SHIPUNOV — Chemical Tuning Strategies for Layered Quantum Materials

Figure 0: Thesis cover

Colofon

Omslag en opmaak: de auteur
Gedrukt door: Printdeal B.V., Deventer

Chemical Tuning Strategies for Layered Quantum Materials

ACADEMISCH PROEFSCHRIFT

ter verkrijging van de graad van doctor
aan de Universiteit van Amsterdam
op gezag van de Rector Magnificus
ten overstaan van een door het College voor Promoties ingestelde commissie,
in het openbaar te verdedigen in de Agnietenkapel
op vrijdag 16 oktober 2026, te 10.00 uur

door Grigory Shipunov

geboren te Ulyanovsk

Promotiecommissie

Promotores:	prof. dr. M.S. Golden	Universiteit van Amsterdam
	prof. dr. B. Büchner	Technische Universität Dresden
Overige leden:	dr. A. Isaeva	Technische Universität Dortmund
	dr. A. de Visser	Universiteit van Amsterdam
	dr. R. Bliem	Universiteit van Amsterdam
	prof. dr. P. Schall	Universiteit van Amsterdam
	dr. G. Perversi	Maastricht University

Faculteit der Natuurwetenschappen, Wiskunde en Informatica

Contents

List of Acronyms

ARPES angle-resolved photoemission spectroscopy
BSE back-scattered electrons
DFT density functional theory
DSM Dirac semimetal
EDX energy-dispersive x-ray spectroscopy
MR magnetoresistance
PXRD powder x-ray diffraction
SAED selected-area electron diffraction
SC-XRD single crystal x-ray diffraction
SE secondary electrons
SEM scanning electron microscopy
SOC spin orbit coupling
SQUID superconducting quantum interference device
STM scanning tunneling microscopy
TEM transmission electron microscopy
TMDC transition metal dichalcogenide
TP triply-degenerate point
TSM topological semimetal
VSM vibrating sample magnetometer
WDX wave-dispersive x-ray spectroscopy
WSM Weyl semimetal

List of Figures

List of Tables

Introduction

Materials discovery is driven by modern technology striving to enhance energy efficiency for sustainability. The accelerating pace of information processing, the recent renaissance of neuromorphic computing, and the proliferation of communication systems demand for high-performance conducting materials with higher processing speeds, greater data transfer capabilities, and minimal losses. Rapid technological progress may even lead to a paradigm shift altogether, from the silicon-dominated semiconducting era that relies on charge conductivity to new material platforms that utilize spin and/or orbital momenta.[1–3]

This vision has encouraged extensive research in the field of quantum materials, which Robert Cava defines as materials *"whose electronic or magnetic properties are best described as having a nontrivial quantum mechanical origin – in other words materials where classical particles or calculations that do not take into account the full character of the system do not adequately describe the electronic or magnetic properties displayed"*.[4] In the modern condensed matter* community, this umbrella term broadly encompasses diverse classes of materials. They are of significant interest both for their fundamental ability to host new types of quasiparticles and exhibit unprecedented quantum phenomena, and for their potential to advance technologies in computation, communication, sensing, and energy.[3]

The experimental research presented here focuses on materials optimization in the quantum materials subclass of bulk topological semimetals (TSMs). Topological materials have entered the spotlight after the experimental realization of first topological insulators in 2007–2009 in 2D CdTe/HgTe quantum wells and 3D systems such as Bi_2Te_3, Bi_2Se_3, Sb_2Te_3, $Bi_{1-x}Sb_x$.[5] Those quantum materials with the chemical potential in a bulk band gap exhibit spin-polarized, conducting surface states. Those states are also resilient to charge carrier backscattering due to *topological protection* via spin-momentum locking. The discovery of 3D TSM in the realization of Cd_3As_2 and Na_3Bi in 2014 has extended this phenomenology to the bulk states.[5] The first 2D material—graphene[6–8]—is also the first example of a 2D Dirac TSM, whose linear energy-momentum relationship near the K points of the Brillouin zone can be described by the Dirac equation.[9,10]

Charge carriers in the linearly-dispersing bands in a TSM can give rise to unique electronic properties. Graphene realizes near-room-temperature quantum Hall effect,[11] twistronics,[12] which includes unconventional superconductivity.[13] TSMs demonstrate record characteristics exceeding the ranges of trivial semiconductors and metals, for instance: extremely high electron mobility (Cd_3As_2 has 10^7 $cm^2/V{\cdot}s$ at low temperatures, which is three orders of magnitude higher than silicon),[14] large non-saturating magnetoresistance (WTe_2 has up to 13×10^6 % under a magnetic field of 60 Tesla at low temperatures,[15] which is a million times higher than copper in similar conditions), high carrier density (up to 10^{22} cm^{-3} in Na_3Bi) combined with low effective mass close to that of free electrons, and ultra-high low-temperature conductivity (a residual resistivity ratio (RRR) exceeding 10^3 in $PtSn_4$[16]). Beyond that, TSM exhibit quantum phenomena enabling interesting and potentially useful conducting behavior. For example: chiral anomaly, i.e. chiral charge is not conserved in the presence of parallel electric and magnetic fields, and negative magnetoresistance, in which the resistance decreases as the magnetic field increases. For example, in TaAs there is an 80 % resistivity decrease in magnetic

*In this thesis, the terms "condensed matter" and "solid state" are used interchangeably. Historically, the former is more common in physics, while the latter is preferred in chemistry. In the context of this thesis, both terms apply to periodic crystalline solids.

field.[17] Finally, Shubnikov-de Haas quantum oscillations at fields as low as 0.5 Tesla with the Berry phase close to π in $ZrTe_5$ deserve a mention.[18]

Despite all these interesting developments, research in topological materials is still in its early stages, focusing on the discovery of new candidates of various types, and understanding how their properties relate to their chemistry and crystal structure. Many research consortia around the world are tackling this challenge in an interdisciplinary manner, with common efforts from physicists, chemists, and theoreticians. First, expanding the pool of available materials is a crucial avenue in the field, as we are still in the acquisition phase of identifying materials with the best-performing properties. A chemist's expertise is very helpful in designing experimental synthetic strategies for predicted materials. This dissertation addresses this task from a chemist's perspective and aims to contribute to the following knowledge gaps.

Outline of the thesis

The scope of this thesis spans the intersection of inorganic chemistry, crystallography, and condensed matter physics.

Chapter 1 introduces TSMs and explains the "composition–structure–property" guiding principle of materials design illustrating how chemical composition and real-space crystal structure influence the electronic properties of selected topological semimetals. Moreover, it highlights how seemingly small misjudgments in structural analysis and chemical composition can result in controversies in the band-structure analysis and, consequently, in the expected topological properties.

Chapter 2 outlines the foundations of the main synthetic techniques employed in the present work. The general principles of phase diagrams are sketched, and various approaches to selecting synthetic conditions based on the thermodynamics and kinetics of solid-state systems are discussed. **Chapter 3** provides general overview of characterization methods employed in this work.

Chapters 4–6 of this thesis thoroughly examine the subtle details of composition and structure, which, in turn, influenced by the choice of synthetic conditions, in three different classes of quantum materials, including topological semimetals and candidates for unconventional superconductivity.

Chapter 4 introduces TSM and superconductor $PtBi_2$, and navigates through its rich polymoprphism. The goal is to optimize the synthesis of the trigonal γ-$PtBi_2$ polymorph that is the outmost interesting topological phase. Following the crystal growth of the target polymorph, its crystal structure is re-investigated, solving the long-standing controversy about its lattice symmetry. Consequently, this result clarifies which band structure model and topological electronic states are inherent to γ-$PtBi_2$. Moreover, several possible substitutional series are investigated and the effects of the substitution on structure and properties are preliminary assessed.

Chapter 5 deals with a family of candidate type-II Weyl semimetals, ternary $TaTMTe_4$ (TM = Ir, Rh, Ru) compounds. Several members were published long ago, but no single crystals were available. While $TaIrTe_4$ has already been studied as a type-II Weyl semimetal (WSM) candidate and crystal growth protocols were available, sizable crystals and reliable composition information for the Rh- and Ru-containing members, and especially for substituted variants, remaining less developed. In this chapter, crystal growth of $TaIrTe_4$, $TaRhTe_4$, and $Ta_{1.25}Ru_{0.75}Te_4$ is explored, together with first attempts at transition-metal substitution. This chapter also revisits crystal structures of the family members, and finds out non-stoichiometry, atomic disorder and lattice changes in the $Ta_{1.25}Ru_{0.75}Te_4$ compound*. These findings suggest that Ru-compound may be structurally and electronically closer to WTe_2 than to the ordered $TaIrTe_4$-type structure, making it attractive for future in-depth studies.

Chapter 6 addresses K_xRhO_2, a compositionally versatile material with a rich phase diagram of physical properties as a function of x. We present a new synthetic approach to this material, which may potentially give access to new compositions and properties. We show the preliminary results of how the synthetic route impacts magnetic properties.

*This was previously reported as the stoichiometric, isostructural $TaRuTe_4$ compound[19]

Chapter 1

Design Tips for Quantum Materials

1.1 Main Mantra of Material Design

This section largely based on West,[20] Hoffmann,[21] Pauling,[22] Atkins et al.,[23] and Singleton.[24]

How can we practically steer the design of quantum materials toward non-dissipative, energy-efficient conductive properties that are in high demand? The cornerstone of creating a new functional material is to identify the key characteristics that are needed to achieve the desired properties. *The relationship between property and structure* is widely recognized as central and crosscutting concept in natural sciences, including all disciplines of chemistry. Linus Pauling in "The Nature of the Chemical Bond" (1939)[22] first introduced this concept into inorganic chemistry on the examples how the structure of molecules and crystals determines their chemical and physical properties.

The term *structure* relates to arrangements of atoms in a chemical compound. For crystalline inorganic solids that are considered here, it boils down to the crystal structure:* a periodically repeated array of atoms (unit cell) in real-space (conventionally, in three dimensions, but can be 2D or 1D as well) that possesses certain symmetries (labelled by a crystal class and a space group).[25] Often, this part of the relationship is expanded to "composition–structure" to emphasize the decisive role of the chemical nature of the involved atoms and their bonding interactions.†

A chemical compound exhibits a given array of descriptive properties. This broad array includes chemical (reactivity, toxicity, flammability, solubility, volatility, etc.), mechanical, thermal, electrical, magnetic and optical properties. In chemistry, property is often understood synonymously to purpose or function. Materials design is aiming to find candidates that are specially fitted for an application.

The *composition–structure–property* concept states that a given property is related to the compound's chemical composition and crystal structure. The question of which particular ingredient is the most influential is the crux of materials chemistry. Once unraveled, this tuning knob is used to guide materials design strategies and optimization of the compound's chemical and physical behaviors. Even minuscule deviations from the idealized composition or high symmetry may entail strong alteration of the related property. Basically, the task of materials design is to figure out these linkages, find out by what they are steered and how strong the impact of various compositional and structural components is on the related property. This algorithm describes in broad brushstrokes the workings of materials chemistry.

In the 1960s, Roald Hoffmann contributed by laying out the theoretical foundations of how the symmetry of molecular orbitals determines the chemical properties of a compound, namely, reaction pathway and stereochemistry (Woodward–Hoffmann rules). Later, he developed the extended Hückel method, a semi-empirical quantum chemistry technique used to approximate molecular orbitals, also in periodic solids.[21] This method helps chemists understand how changes in crystal structure affect the electronic properties, such as energy levels and band dispersions, and how the overlap and interaction of orbitals influence bonding and stability of solids.

*Present work uses the term "structure" in this meaning.

†For sake of conciseness,we don't mention here microstructure effects, defects of various order, etc.

Hoffmann's approach, adopted broadly into inorganic chemistry by von Schnering, Tremel, and Ibers, is based on the visualization how atomic orbitals placed on a certain geometrical arrangement interact with each other, in bonding or antibonding fashion, forming molecular orbitals. This picture is valid for covalent (ionic) interactions of localized electrons when the orbital picture is applicable. It also makes the assignment of oxidation states important in order to understand whether the electric neutrality state (semiconductor or insulator) will be achieved between electron donors and acceptors in a solid or would there be some uncompensated charges (metal).

By simplifying the calculation of molecular orbitals, Hoffmann enabled the exploration of structure–property relationships in complex systems. His approach, albeit simplified as compared to the modern DFT machinery, is still assisting the chemists today to explain why the atoms with certain oxidation states built up frameworks in a certain way. This principle allows for quick crystal structure design and prediction of the impact of doping on structure and properties without need to resort to computationally expensive DFT methods. For instance, it explains the behavior of transition-metal oxides in relation to their electronic conductivity and crystal structure. Undoped $Sr^{2+}Ti^{4+}O_3^{2-}$ is an insulator at room temperature due to the strongly covalent Ti–O bonding and electric neutrality which results in a large band gap. Doped $SrTiO_3$ with e.g. La^{3+} becomes a highly conductive material by extra electrons occupying the conduction band, if the crystal structure of the cubic perovskite type remains unchanged.[20]

This principle holds true even if we narrow down our scope to quantum materials. The "structure–property" concept trains one to search the origins of physical phenomena in atomic structure and interactions. The defining characteristics that influence the macroscopic electrical properties of a periodic crystalline solid are found in their electronic band structures. In turn, the band structure of a periodic crystal is determined by the types of the involved atoms, their geometric arrangement and interatomic bonding.[24] Bloch's theorem links the direct and reciprocal periodic spaces and describes the behavior of electrons in a periodic solid. Complexity arises from quantum-mechanical interactions such as orbital mixing, hybridization, spin-orbit coupling and correlation effects. Moreover, quantum materials harbor exotic quasiparticles, whose energy dispersion give rise to interesting emergent phenomena, such as high electron mobility, giant magnetoresistance, etc. All of this obfuscates the linkage between atomic structure and physical properties.[26]

When it comes to complex electronic systems like topological materials and superconductors, chemical bonding concepts are insufficient. However, the importance of careful consideration of lattice symmetry and chemical composition remains crucial for understanding the quantum material at hand.

Modern theory provides exciting predictions of new quantum materials. Theory often uses entries from crystallographic databases as input to model the band structure and to make advanced predictions of properties. Often these inputs are used for high-throughout screening for potential candidates.[27] However, some of these crystal structure descriptions date back to the early years of the structure analysis and are incomplete or plainly wrong due to the limitations of the experimental methods back then. Without a background in x-ray crystallography it is difficult to assess the quality of available data, and high-throughput screening often does not sufficiently discard poor cases. As exemplified below by my own work and published examples, very often a critical revision of the crystallographic data is paramount the for the correct interpretation of the physical properties. So, for many candidate quantum materials the first crucial step is to carefully examine their crystal structure for possible superstructures or lattice-symmetry reductions, twinning or atomic disorder phenomena in order to ensure accurate input for theoretical modeling.

As will be discussed in more detail in Sec. 1.4, another glaring omission that often occurs in literature is insufficient or inadequate compositional analysis of the material. Even a straightforward method with relatively high systematic errors such as energy-dispersive x-ray spectroscopy (EDX) can give a crucial hint regarding a possible structural mishap, if one keeps in mind that the composition gives rise to crystal structure. Another simple check is the oxidation states of the elements composing the compound: a chemist may check whether the co-existence of assigned valence states is possible within a compound—or would these two elements spontaneously engage in a redox reaction if they had had these molar ratios and oxidation states. Coordination environments and connectivity of the elements are also dependent on the valence state of the central atom, providing yet another way to sanity check the material under consideration.

Ongoing research shows that all the above-mentioned aspects are relevant for the young field of topological semimetals and other quantum materials. Scientific and applied interest in them is fueled mainly by their properties and envisioned functionalization, so the concept is often reversed to *"property – structure"*. Essential information about the structural and compositional part of the relationship is often missing, incomplete, or insufficiently accurate.

The remainder of this chapter will set the stage for the rest of the thesis, giving a brief overview of a TSM band structure, and its arising *properties*, how the band structure is influenced by minute detail in the *structure* and explore the importance of chemical and phase *composition* and its influence on the material's preparation and resulting crystal structure.

1.2 Property: Topological Semimetal Phase

This section largely based on Yan and Felser,[26] and Singleton.[24]

Condensed-matter physics classifies solids into semiconductors (insulators)* and metals based on their electronic band structure. The former have an energy separation—a bulk band gap E_g—between the highest occupied electron state (top of the valence band) and the lowest unoccupied state (bottom of the conduction band) at each momentum k of their three-dimensional Brillouin zone at 0 K (Figure 1.1b). The latter have a continuous energy spectrum of electronic states available for the electrons excited from their ground state at any given temperature if the Fermi level is within the valence or the conduction band. A *semimetal* is a sort of an intermediate state with a small density of states at the Fermi level due to energy overlap (at different k) of conduction and valence bands in the Brioullin zone (Figure 1.1a).

A *topological insulator* has a gapped energy spectrum like a conventional, trivial semiconductor, but with an *inverted band order* at some k values (Figure 1.1d). This band inversion can be promoted by spin orbit coupling (SOC). If a hybridization gap opens between the inverted states, the result is a topological insulator possessing a bulk bank gap. In addition this system has two spin-polarized, linearly dispersing surface states within the bulk gap (Figure 1.1d). If the two inverted bands touch at one particular momentum k, a *Dirac semimetal* results (Figure 1.1c). The touching point of the bands, called the *Dirac point*, is fourfold degenerate (twofold both in k and in spin).

A DSM can be also defined as the phase living at the critical point of a *quantum phase transition* between a trivial semiconductor and a topological insulator. The transition may proceed upon increasing SOC that brings the conduction and valence bands closer in energy, and the Dirac semimetal (DSM) is the point where they touch and close the bulk gap. Upon further increasing SOC, the gap reopens with an inverted energy-state order.

If time-reversal or lattice-inversion symmetry of the periodic crystal is broken, the degeneracy in a DSM can be lifted, and one Dirac point splits into two spin-polarized *Weyl points* separated in momentum space, forming a *Weyl semimetal* (WSM, Figure 1.1e). Each Weyl node is, thus, twofold-degenerate. The Weyl state may arise in a magnetically ordered material or in a lattice with a non-centrosymmetric space group. The latter highlights importance of the correct determination of the lattice symmetry as it has direct consequence for the electronic state.

The peculiar conducting characteristics of TSMs exemplified in the introduction are related to the linear dispersion relation of the topological bulk bands. Charge carriers in a TSM that are close in energy to the Dirac (or Weyl) point cannot be described as nearly-free quasiparticles by the Schrödinger equation. Instead, their energy dispersion relation is analogous to the behavior of relativistic particles described by the Dirac-like Hamiltonian:

$$H(\mathbf{k}) = \pm \hbar v_F \mathbf{k} \cdot \sigma, \tag{1.1}$$

where $\mathbf{k} = (k_x, k_y, k_z)$ is the momentum matrix in 3D space, v_F is the Fermi velocity, and σ is the Pauli spin matrix.

This has the same form as the Dirac hamiltonian in high-energy physics, with the speed of light c replaced by the Fermi velocity v_F and the effective mass equal to zero.[28] Zero effective mass of a Dirac

*The difference between semiconductors and insulators is quantitative, with the boundary typically drawn at 3 eV.

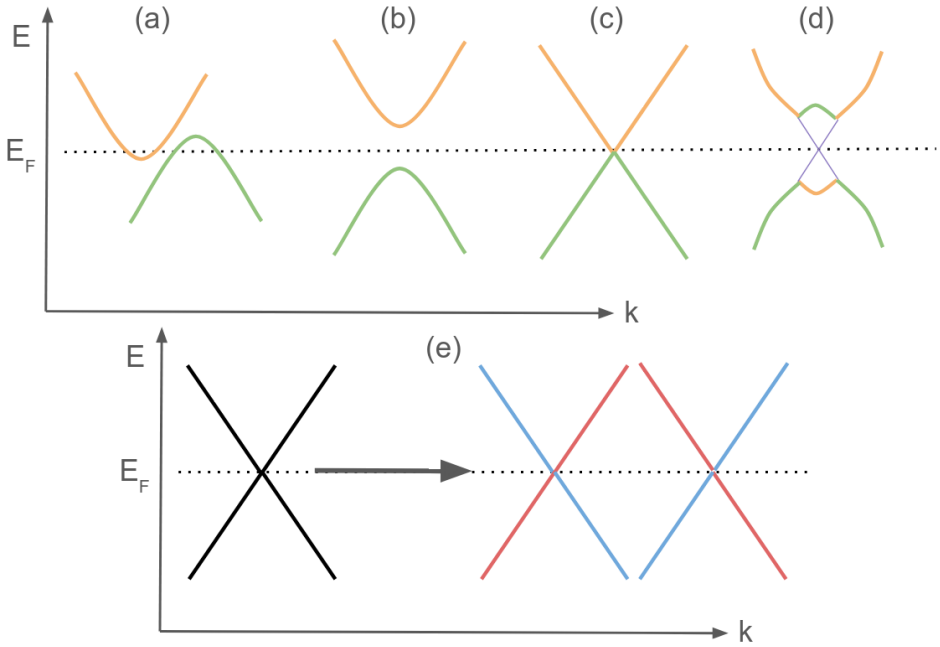

Figure 1.1: Schematics of band structures of (a) trivial semimetal, (b) trivial semiconductor, (c) Dirac topological semimetal, (d) topological insulator, (e) lifting of degeneracy resulting in Dirac point splitting into two Weyl points (red and blue bands indicate two spin-polarized branches). On panels (a)–(d) conduction band is orange, valence band is green, topological surface states are in purple. E_F—Fermi energy (shown with dotted line).

(or Weyl) fermion quasiparticle results in gapless energy spectrum, as shown in Figure 1.1c. This combination makes materials hosting such fermions, such as TSMs, candidates for applications in high-speed and high-efficiency electronic devices, surpassing the performance of conventional (trivial) conductors and many topological insulators.

Weyl fermions are chiral due to the lifting of spin degeneracy, making the WSM attractive candidates for spintronic devices, which rely on the manipulation of electron spin rather than charge. Two Weyl points, the solutions of the Eq. 1.1, have opposite chiralities, and are the source and the sink (monopoles) of non-trivial Berry curvature (see Figure 1.2b). A topological surface state appearing in a WSM is called a *Fermi arc* and it connects the Weyl points with opposite chiralities. Fermi arcs are protected by the bulk Weyl topology as long as the Weyl nodes of opposite chirality remain separated and the relevant symmetries and topological structure are preserved. Therefore, Fermi arcs are robust against perturbations, making the WSMs candidates for the development of stable quantum bits for quantum computing.[3,26] Stronger SOC increases the splitting of Weyl nodes in momentum space (Figure 1.2c,d), making compounds with heavier elements more attractive for spintronics applications.

Moreover, due to the protected locking between the spin and orbital momenta of the topological bands, WSMs exhibit the *chiral anomaly*, a phenomenon where the conservation of chiral charge is violated in the presence of parallel electric and magnetic fields. This can lead to novel transport phenomena such as quadratic negative magnetoresistance, which is unique to TSM in contrast to topological insulators and has strong potential for sensor applications.[26,31]

Nowadays, the classification of known TSMs has expanded dramatically[5] and includes topological features of various dimensionality (crossing points, nodal lines and surfaces), degeneracy (twofold, threefold, fourfold, sixfold, eightfold) and dispersion of the Dirac-like bands (linear, quadratic, cubic). Dirac and Weyl cones can be isotropic (respecting Lorentz invariance and Eq. 1.1) dubbed *type-I*, or

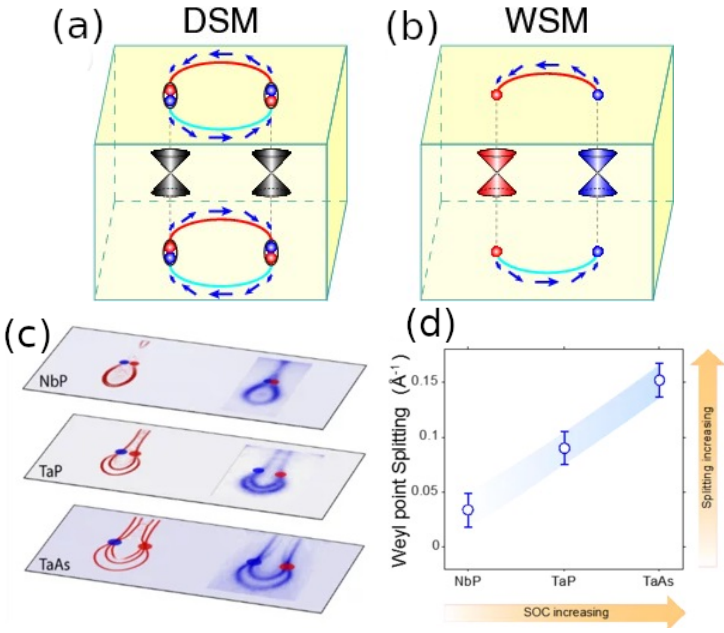

Figure 1.2: Topological Fermi arcs in the TSM. (a) Schematic of a DSM with spin-polarized Fermi arcs on its surface (red and light-blue; blue arrows shows spin texture) connecting projections of two bulk Dirac nodes (blue and red circles). The black color of Dirac cones indicates that one Dirac node is the degeneracy of two Weyl nodes with opposite chirality. (b) Schematic of a WSM with spin-polarized Fermi arcs on its surface connecting projections of two bulk Weyl nodes. The red and light-blue colors represent opposite chirality. For clarity, only surface states on the top and bottom surfaces are indicated. (c) The calculated and measured Weyl points and Fermi arcs in three transition-metal pnictides. (d) Extracted Weyl point splitting plotted against the spin-orbit coupling strength. Figures from Liu et al., Lv et al.[29,30]

tilted along a certain k direction (violating Lorentz invariance) dubbed *type-II* (Figure 1.3). Type-II Weyl states give rise to particular optical and magnetic features thanks to the appearance of hole and electron pockets, which enriches the portfolio of TSM exotic physical properties.[26,32]

In terms of real materials, the TSM class is very diverse. The prime examples of bulk DSM are Na_3Bi, Cd_3As_2 and $PtTe_2$, whereas the most famous WSM are TaAs and its derivatives as well as WTe_2.[26,33–36] Most interest in the condensed-matter community is placed on the property (function), whereas chemical and structural features are usually investigated less thoroughly. Chemically, the known TSM belong to very different classes, and it is challenging to find unifying characteristics. This, in turn, complicates tailored materials design of these materials.

TaAs hosts a large number of Weyl points that are well separated in momentum space (Figure 1.4).[34,37] As a result, it exhibits clear and well-defined surface Fermi arcs which have been extensively studied with angle-resolved photoemission spectroscopy (ARPES) and scanning tunneling microscopy (STM).[33] TaAs also exhibits strong chiral anomaly effects. These clear experimental signatures promoted TaAs and its derivatives, TaP and NbP, to the textbook examples of a WSM.

WTe_2 exhibits Weyl points arising from a linear intersection of the conduction and valence bands. The lack of inversion symmetry in WTe_2 crystal lattice is essential for the occurrence of Weyl fermions and their good separation in momentum space. In case of WTe_2 this signature of the electronic structure translates into the extremely high charge carrier mobility (exceeding 10^4 $cm^2/V{\cdot}s$ at low temperatures) and large, non-saturating magnetoresistance.[15]

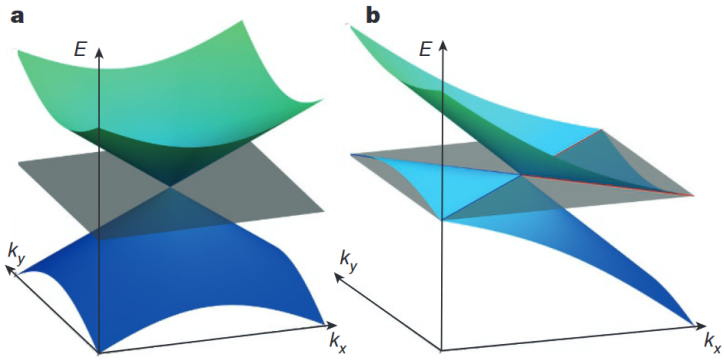

Figure 1.3: Schematic of a type-I (a) and type-II (b) WSM. The type-I features a point-like Fermi surface. In the type-II, the Weyl point is a contact point between the electron and hole pocket. Fermi energy denoted with gray plane. Figure from Soluyanov et al.[32]

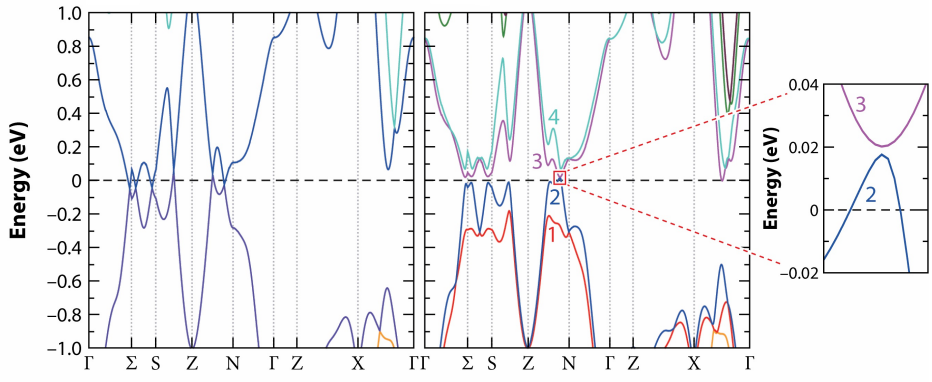

Figure 1.4: The calculated band structures of TaAs (a) without and (b) with spin-orbit coupling. The Weyl points exist off the high-symmetry lines and are not visible from panel b. The numbers 1 to 4 denote the second valence band, the first valence band, the first conduction band, and the second conduction band, respectively. Figure from Weng et al.[34]

The isostructural van der Waals compounds $PtTe_2$ and $PdTe_2$ demonstate that TSM are proximate to another intriguing and less-explored class of quantum materials, topological superconductors (TSC).[38,39] A TSC is a state with a full superconducting gap in the material's bulk and gapless topological states (Andreev bound states) protected by symmetry at the boundary. TSC represents a distinct type of quantum phases and cannot be derived from the conventional superconductors, namely, from the Bose–Einstein condensate of Cooper pairs. TSC are only found in unconventional superconductors, and their excitations are not electrons, but exotic Bogoliubov quasiparticles, which are linear combinations of electron and hole excitations.[38,39] Fermi arcs are less stable in DSM than in WSM. So if a DSM is in a superconducting state, the surface electrons may form Cooper pairs and surface superconductivity may arise. The type-II DSM are believed to be good candidates for the TSC state thanks to their large pockets of electrons and holes near the Dirac points as those contribute to a large DOS which is favorable for SC. In this light, $PdTe_2$ and $PtTe_2$, which are Dirac type-II TSM, are studied as viable TSC candidates.[40]

Fermi arcs and bulk non-trivial states can be observed directly in ARPES and many of the unique

WSM properties manifest themselves in transport experiments and scanning tunneling microscopy (STM) measurements; however, these time- and effort-consuming experimental techniques cannot be used for high-throughput screening of potential new candidates. Moreover, they cannot yield an interpretation of the observed signatures in terms of electron topology. This information can be obtained by theoretical modelling, for instance, density functional theory (DFT) methods. These, in turn, require a reliable structure model for enabling realistic outputs and making predictions. Explorative synthesis of new materials often goes hand in hand with band-structure "screening" by computational methods in order to spot the signatures of possibly topological band crossings. As has been already repeatedly emphasized in the beginning of the Chapter 1, knowing the correct lattice symmetry is crucial for correct band structure calculation.

TaAs has earned the place as a well-studied textbook example of a WSM also thanks to the fact that it does not pose any serious challenges from the standpoint of crystal structure or crystal growth. The scientific community keeps on searching for more optimal TSM. Since the topological band crossing in a TSM is part of the bulk-band continuum, it is very challenging to design a material which can boast the Dirac cones positioned at the Fermi energy, while other, trivial bands do not contribute to the conductivity. New candidates are often being proposed, and some of them present complicated cases of ambiguous structure or composition.

1.3 Structure: the Big Effects from Tiny Shifts

Here, we illustrate several challenges while studying the structure of a topological material using the example of Cd_3As_2. Research on this material dates back to the 1930s, and it has garnered consistent interest due to its extraordinary electron mobility above 10^4 $cm^2/V{\cdot}s$ at room temperature. Even after the discovery of graphene and other 2D materials with very high mobilities, Cd_3As_2 remains competitive as it has the highest reported mobility of 10^7 $cm^2/V{\cdot}s$ at low temperatures.[14] Today, it is widely recognized that this remarkable conducting property is linked to Cd_3As_2 being a TSM.[41] However, there is still ongoing debate regarding its precise classification,[42] and this open question is strongly intertwined with its crystal structure.

Even though at first glance, it is a "simple" inorganic binary compound, Cd_3As_2's crystal structure is actually quite complex. The first thing to do is to decide *which cadmium arsenide structure* to consider. Cd_3As_2 is a typical example of a system with rich *polymorphism**. Typically the different structures, termed *polymorphs*, are thermodynamically stable under different external conditions, with typical variables being temperature and pressure. The crystal structures of the polymorphs are usually related to each other by a sequence of symmetry elements. A lower symmetry is usually found for a polymorph stable at lower temperature.[44] Cadmium arsenide has four polymorphs in total,[45] which all can be derived from the basic antifluorite structure type (*fcc*, CaF_2). The high-temperature (HT) polymorph has the highest lattice symmetry as it crystallizes in a face-centered cubic lattice (space group $Fm\bar{3}m$, lattice parameter $a = 6.24$ Å) with two vacancies† statistically distributed on the cadmium site.[46] The coordination sphere of an As atom is an idealized cube $[As(\frac{3}{4}Cd)_8]$ in the average structure of this cubic polymorph (Figure 1.5 Fm-3m HT). As the temperature decreases, the vacancies begin to arrange into channels, leading to the cadmium positions becoming non-equivalent. The coordination sphere of an As atom changes to $[AsCd_6\square_2]$, which initiates a shift of the cadmium positions towards these channels of vacancies (Figure 1.5 P42/nmc IT). These distortions entail subsequent structure transitions at 600 and 470 °C to the intermediate-temperature (IT) polymorphs with a primitive tetragonal lattice (space group $P4_2/nmc$ and $P4_2/nbc$) and an expanded unit cell ($a = 8.95$ Å, $c = 12.65$ Å).[47] The fourth, low-temperature (LT) modification is stable below 220°C. It exhibits an even more complex vacancy arrangement (Figure 1.5 $I4_1/acd$ LT), resulting in a larger cell: this polymorph crystallizes in a volume-centered tetragonal lattice, with another parameter increase to $a = 12.67$ Å and $c = 25.48$ Å.[48] The exact space group was re-evaluated to be centrosymmetric $I4_1/acd$ instead of non-centrosymmetric $I4_1cd$ only recently.[48]

*The phenomenon in which the same chemical compound exhibits different crystal structures[43]

†The atomic composition of the unit cell can be written as $Cd_6\square_2As_4$ to match up with the A_8X_4 general formula for the antifluorite cell, where □ denotes a vacancy.

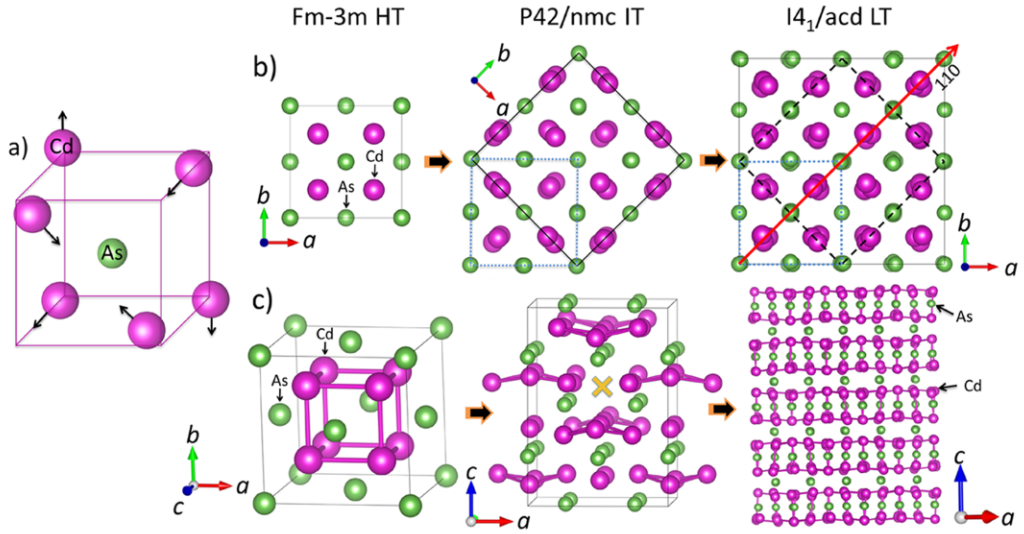

Figure 1.5: Crystal structures of different polymorphs of Cd_3As_2. (a) Coordination sphere of an As atom. Arrows show displacements of the Cd atoms toward the Cd vacancies. (b) Structure relationship of the polymorphs: from the HT to the LT (see text). (c) The Cd cubes and their ordering for each polymorph. In the cubic phase, the Cd atoms are disordered over all of the pseudocube sites, it is antifluorite structure type. In the IT structure, the Cd vacancy channels are shown running along the *b*-axis indicated with the × symbol. In the LT form, the cubes stack in corkscrews along the *c*-axis. Chains of vacancies are no longer present. Figure from Ali et al.[48]

Further alternations in the lattice-symmetry, such as a transition from a primitive to an *I*-centered tetragonal cell, and the possible lack or presence of the inversion symmetry in the LT polymorph, have an immediate impact on the topological band structure of Cd_3As_2 and its carriers' properties. For instance, the lack or presence of the inversion symmetry in the LT polymorph decide whether it is a DSM or a WSM, in which the Weyl states may appear due to the symmetry-related lifting of the spin degeneracy as described in Chapter 1.2. The positions of the Dirac (or Weyl) cones in momentum and energy, their total number and degeneracy, their anisotropy (Fermi velocity, tilting and orientation in momentum space) are all influenced by the crystallographic details.

The room-temperature polymorph of Cd_3As_2 was originally described in a non-centrosymmetric structure model with $I4_1cd$ space group symmetry,[49,50] incompatible with the symmetry requirements for a DSM state. The linear dispersion in ARPES measurements consistent with a Dirac state led to a careful re-investigation of the crystal structure in order to improve the model for theoretical analysis. Indeed, an in-depth single crystal x-ray diffraction (SC-XRD) experiment resulted in a revised structural description: the lattice parameters and the tetragonal crystal class of the previously reported lattice were confirmed, but the space group was updated to the centrosymmetric $I4_1/acd$.[48] This finding led to better reconciliation between the electronic structure simulated by the DFT modelling, and the directly observed one in ARPES. Ambiguity between a centrosymmetric and a non-centrosymmetric case is a frequently occurring, challenging problem in the field of crystallography.[51,52] Resolving it becomes particularly important when distinguishing between various symmetry-dependent topological phases, such as different types of TSMs. This theme will reappear in Chapter 4.

Next, we consider $ZrTe_5$ as another example to illustrating the influence of subtle real-structure effects onto physical properties. The structure of this compound can be described in the centrosymmetric, orthorhombic *Cmcm* space group.[53] Face-sharing [$ZrTe_6$] prisms are linked into columns

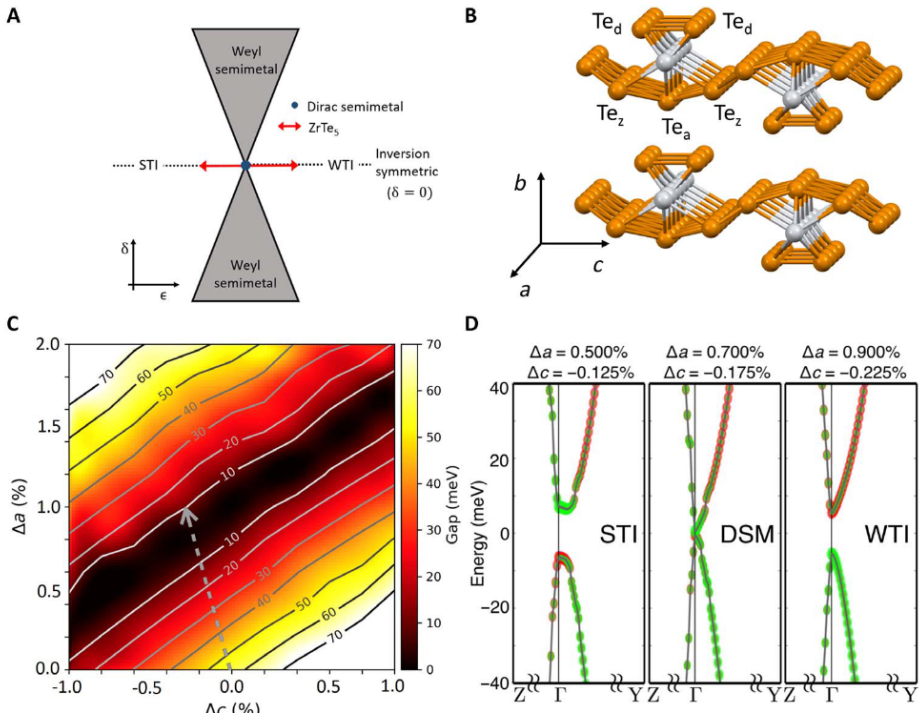

Figure 1.6: Topological phase diagram (a), crystal (b) and electronic (c, d) structures of $ZrTe_5$. (a) Schematic of the phase diagram: δ is the control parameter describing the breaking of inversion symmetry, ϵ is Poisson's ratio. (c) Size of band gap E_G (color scale) at the Γ point as a function of strain in the a and c lattice directions. (d) Calculated band structures for different strain states taken at points along the dashed-line path in (c). STI – strong TI, DSM – Dirac semimetal, WTI – weak TI. The band inversion involves Te p-orbitals from Te_d and Te_z (b) (shown as red and green colors, respectively). Figure from Mutch et al.[54]

extending along the crystallographic a direction. Along the c direction, the columns are connected by tellurium links, Te_z. The resulting [$ZrTe_5$] layers are stacked along the b axis, and held together by van der Waals forces (Figure 1.6b).

The electronic properties of this material are extremely sensitive to the magnitude of the lattice parameters. $ZrTe_5$ has a rich phase diagram as a function of the lattice dimensions (Figure 1.6a). Applied strain, which from the viewpoint of a crystallographer is understood as a change in the lattice parameters and their respective ratios, initiates a *topological phase transition*, i.e. the qualitative change in the electronic structure. As was shown in Chapter 1.2 and Figure 1.1, a transition between phases with different topology – a trivial and a topological insulator – proceeds via a critical point of closing the gap and forming a DSM. In the case of $ZrTe_5$, a transition occurs between two different types of topological-insulator phases, in which each gapped energy spectrum is characterized by a topological invariant Z_2, describing the symmetries of all band inversions and the number and space orientation of topological surface states.[54] Due to topology of the band, the transition between those states is accompanied by closure of the gap and results in a DSM state. The dependence of the band gap size on strain along a and c, together with simulated band structures before, at and after the transition are presented in Figure 1.6c,d.

High sensitivity of the electronic structure to strain originates from the details of the band inversion, which are, in turn, rooted in the peculiarities of the structure. The p-states creating

the band inversion belong to two different Te crystallographic positions, Te_d from the prismatic Zr coordination sphere, and Te_z from the zigzag chains (Figure 1.6b). Since both Te species have similar bonding situations and close oxidation states, the energies and symmetries of their p-states are very similar. As they reside at the Fermi level, they hybridize and realize a topological band inversion, but it takes place in a small range of momenta and energies, and is very susceptible to any minute changes of the Te coordination spheres. Uniaxial strain affects the geometry of the one-dimensional chains by slightly changing the bonding lengths and angles around the Te atoms, and, therefore, is capable of changing the topological character of the material. Mutch et al. expose this effect by showing that less than 1% strain is required to cause a topological transition. Additionally, there is no consensus in the literature whether $ZrTe_5$ hosts the Dirac or Weyl state,[55–58] with an assumption made that the TSM type may change with external temperature.[54,59]

Considering the required symmetry differences between a WSM and a DSM, a plausible hypothesis arises: an external parameter (e.g., temperature or pressure) or a sample-dependent factor (e.g., the synthetic method) could induce a structural transition from a centrosymmetric to a non-centrosymmetric structure. Another possibility is that no such transition occurs, which nonetheless underscores the need for more thorough structural experiments to definitively determine the presence or absence of lattice inversion symmetry in $ZrTe_5$, or to identify any overlooked polymorphic transitions within the material.

The extreme sensitivity to strain further emphasizes the importance of correct structural description, while the ambiguity between Weyl and Dirac physics demonstrates once again how the structure–property relationship is a two-way street. In this context, unexpected behavior in observed properties can prompt new research questions in materials chemistry.

Experimental characterization of topological properties has advanced significantly for layered materials, particularly because they provide well-cleaving specimens ideal for surface-sensitive techniques like ARPES. In these experiments, the maximum signal depth is around 10 nm when using hard X-ray radiation at a synchrotron.[60] "Fresh" surfaces of layered crystals, cleaved *in situ* under ultrahigh vacuum, are free from oxidation, contaminants or adsorbates. Moreover, because the interlayer interactions are relatively weak, there is no significant force imbalance on the atoms at the surface, resulting in minimal *relaxation*[*] or *reconstruction*[†]. This allows to study the material band structure with a sound assumption that signal from this surface layer is representative of the whole material.

On the flipside, layered compounds are often plagued by a particular form of polymorphism known as *polytypism*, where the compound can form several crystal structures that differ based on the stacking sequence of nearly identical layers.[62] These materials also commonly suffer from a high amount of *stacking fault* defects. This issue arises from the same underlying reason: weak interlayer interaction. It fails to hold the layers together firmly, resulting in low energy penalty for the formation of a stacking fault or allows the coexistence of multiple polytypes under the same external conditions. These defects, particularly stacking faults, significantly complicate X-ray diffraction analysis. The defect itself and the surrounding structural relaxation can be thought of as variations in the *d*-spacings within the crystal, causing the diffraction conditions to be satisfied over a wider range of angles, thus, effectively "smearing out" the diffraction reflections. Additionally, these defects contribute to diffuse scattering, which reduces the signal-to-noise ratio in the experiment. While both reflection broadening and diffuse scattering can be informative, for instance, in total scattering methods, they complicate the analytical models and often require advanced laboratory equipment or synchrotron radiation to obtain usable data.[63–66]

Cadmium diiodide, CdI_2, is the textbook example of a polytypic compound. It crystallizes as sheets of $[CdI_6]$ edge-sharing octahedra, which are held together by van der Waals forces. Due to weak interlayer interaction, these layers can easily change their relative positions and, thus, alter the lattice periodicity along the stacking direction. The cadmium iodide structure class is remarkably prolific; for example, a report by Chadha[67] identified three new CdI_2 polytypes at the time, and

[*] "The case when the atomic structure of the topmost layer is the same as in the bulk but the first interlayer spacings are modified",[61] i.e. a situation when the interplanar distances between the first several layers near the surface are different from the bulk, or the layers near the surface are shifted relative to each other.

[†] "The cases when the atomic structure of the top layer is modified. In most instances, the reconstructed surface is characterized by symmetry and periodicity different from those of the bulk"[61]

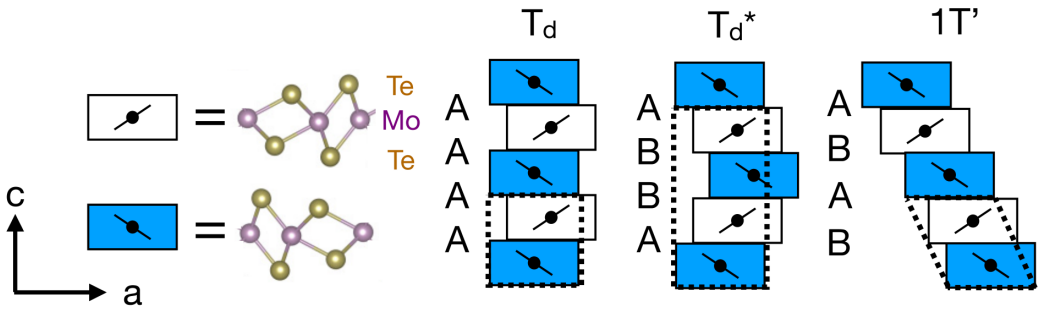

Figure 1.7: Layered motifs and stacking variants of $MoTe_2$ polytypes. Figure from Tao et al.[84]

another report by Pałosz[68] identified 19. Today, the Inorganic Crystal Structure Database contains over 200 entries corresponding to the CdI_2 composition. Although cadmium iodide with an optical band gap of 3.8 eV is not of interest in the field of topological materials, this structure type serves as the progenitor for many structurally related compounds. Notable examples of topological materials within this class include WTe_2 and $MoTe_2$.

Both $MoTe_2$ and WTe_2 exhibit a reversible metal-insulator transition, making them attractive candidates for two-dimensional nanoelectronics.[69,70] WTe_2 hosts a quantum spin Hall state both in the bulk,[71–73] as well as in monolayers,[74] and it exhibits large, non-saturating magnetoresistance.[15,75] Reports indicate that both $MoTe_2$ and WTe_2 exhibit type-II Weyl semimetallic behavior, as demonstrated theoretically and experimentally.[32,76–80] Additionally, $MoTe_2$ has been found to host an edge supercurrent.[81] Another notable feature of these materials is the potential for the formation of polar domains. As reported by Sharma et al.[82] and Huang et al.,[83] both WTe_2 and $MoTe_2$ exhibit switchable spontaneous polarization and natural ferroelectric domain structures in seemingly non-magnetic materials, with WTe_2 showing this effect even at room temperature. Combined with their metallic conductivity, these properties make WTe_2 and $MoTe_2$ the first reported real-world examples of ferroelectric metals.

WTe_2 and $MoTe_2$ possess a van der Waals layered structure, which can be described as a distorted CdI_2 structure type. The metal atom is coordinated by 6 Te atoms, forming a distorted octahedron. The metal atoms move towards each other to form zigzag chains along the a crystallographic axis, with the W–W distance of 2.85 Å (isostructural motif for molybdenum). The resulting layers are held together by van der Waals forces, and stacked on top of each other along the c axis with a translational shift along the b direction.[19]

There are several ways in which the layers can stack on top of each other, leading to multiple polytypes for these compounds: T_d and $1T'$ for WTe_2 and $MoTe_2$, with the addition of $1T_d^*$ for $MoTe_2$. The only structural difference between these polytypes lies in the stacking order of the covalently bonded layers. A schematic of these different stackings is presented in Figure 1.7.

In the T_d polytype, the shift between the layers alternates along the stacking direction, with every third layer positioned directly above the first. This arrangement results in a lattice described by the orthorhombic crystal class in the non-centrosymmetric space group $Pnm2_1$. As the temperature increases, the $1T'$ stacking becomes favored, where each successive layer is shifted in the same direction, reducing the lattice symmetry to the monoclinic system, with the centrosymmetric space group $P2_1/m$.[84,85]

While the geometric difference in these stacking sequences may seem minor, it yields a significant change in the material's overall symmetry. This is highlighted by the substantial differences in physical properties: Weyl physics and various unconventional electronic properties are only present in the orthorhombic, non-centrosymmetric T_d polytypes of WTe_2 and $MoTe_2$ (Figure 1.8), while the monoclinic, centrosymmetric polytypes are "boring" trivial semiconductors. Given that such polytypic transitions may occur relatively easily, especially in layered materials, it is crucial to synthesize the

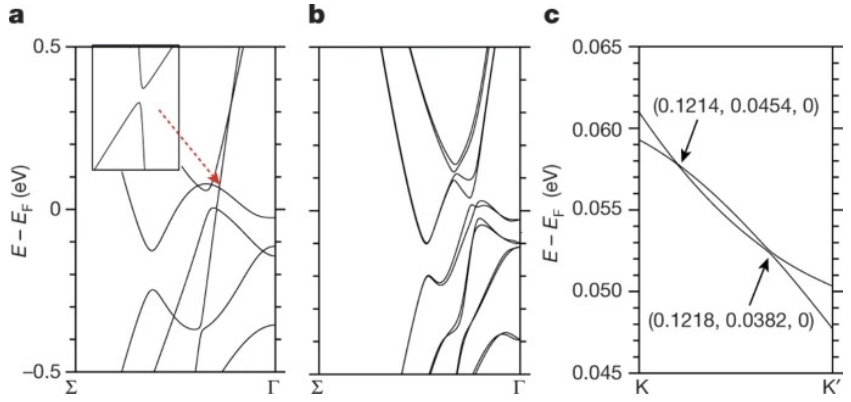

Figure 1.8: Type-II WSM in the T_d polytype of WTe_2. Calculated band structure along the $\Gamma - X$ line ($\Sigma = (0.375, 0, 0)$) without (a) and with (b) SOC. (c) One of the four pairs of Weyl points (fractional coordinates in the reciprocal space are given in units of reciprocal lattice constants). Figure from Soluyanov et al.[32]

correct polytype and understand how factors like composition tuning can affect the transition and, consequently, the material's physical properties.

1.4 Composition: Chemical and Physical Tuning Knob

The composition of a material deserves to be at the first place of the *composition–structure–property* mantra for a good reason. Its decisive influence on the geometric arrangement of atoms is the fundamental topic in inorganic chemistry. It also impacts the electronic structure, both via changes in the electron count and carrier concentrations, and due to more complex phenomena, such as variations in the strength of SOC.

The remainder of this chapter examines two key aspects of how composition influences material properties. First, we will consider the case where changes in composition primarily alter physical properties, allowing for the design of materials with tailored characteristics. Second, we will examine a situation where changes in composition also modify the underlying structural motifs of the atomic arrangement.

The first category, in which compositional changes do not affect the crystal structure, comprises doped materials that are termed *solid solutions*. These crystalline phases exhibit compositional variability that influences their physical properties while keeping the lattice symmetry intact.[20]

Consequently, solid solutions are a go-to playground for *bandstructure engineering* and have been central to semiconductor physics since its inception. For example, $Ga_{1-x}In_xAs$ is a semiconductor solid solution that allows for precise tuning of the material's composition with little structural change across any value of x. This allows to acquire a range of materials with variable direct ($x \leq 0.35$) or indirect bandgap.[24] GaAs and InAs exemplify a special class of isostructural compounds known as *isomorphic* compounds. These compounds not only crystallize in the same unit cell with identical symmetry and geometric atomic arrangement but also share common constituent elements. Such systems are particularly conductive to solid solution formation, enabling gradual tuning of their physical properties. Numerous topological materials exhibit this behavior. Examples include $Bi_{2-x}Sb_xTe_{3-y}Se_y$,[86,87] $Pb_{1-x}Sn_xTe$[88] , and the previously mentioned $Mo_{1-x}W_xTe_2$ system.

The topologically non-trivial phases of $MoTe_2$ and WTe_2 are isomorphic. Moreover, they demonstrate mutual solubility with a wide range of compositions that have been grown. In addition to a number of topology-driven properties described above, $MoTe_2$ transitions to a bulk superconducting state at $T_c = 0.1\,K$.[90] Materials combining Weyl physiscs and superconductivity are a frontier research topic nowadays, since they may host a novel quasiparticle—the Majorana zero-mode—which of great

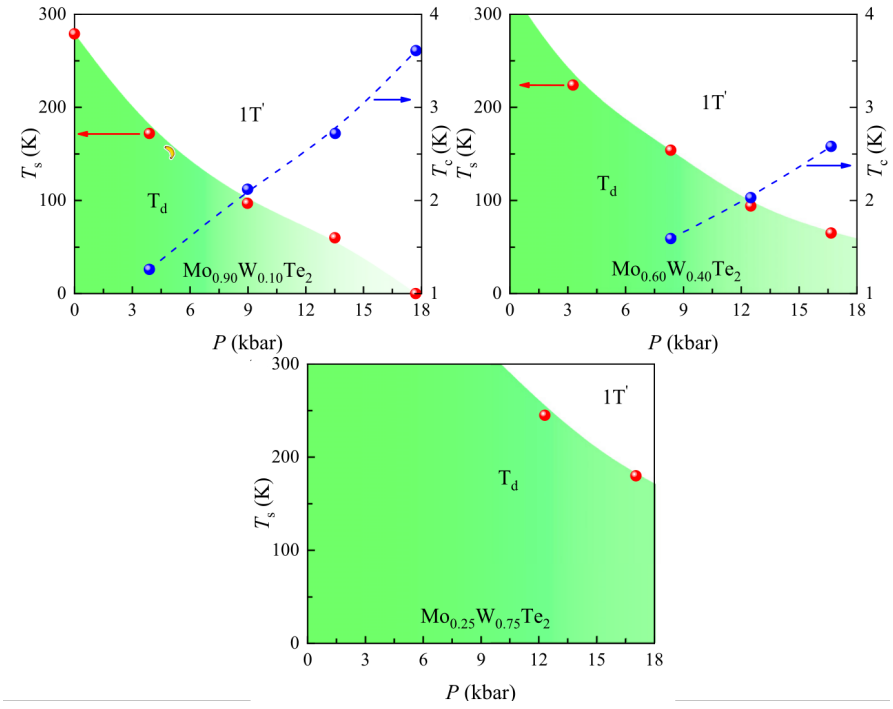

Figure 1.9: Phase diagrams illustrating temperature- and pressure-dependent superconductivity in the $Mo_{1-x}W_xTe_2$ series with various x. T_S is the structural transition temperature, T_C is the superconducting transition temperature. Figure from Dahal et al.[89]

interest both for the fundamental physics and for the development of a next generation of quantum bits.[91] While theoretical modelling of new topological materials and states suffers, as pointed out by Zunger,[92] from "overprediction", progress in superconductivity still mostly relies on experimental outcomes, which includes material design by chemical principles.

In this context, the $Mo_{1-x}W_xTe_2$ series serves as a good model system where both compositional and structural tuning knobs play crucial roles, as outlined in the report by Dahal et al..[89] This study explored several compositions corresponding to $x = 0.1$, 0.4, and 0.75, examining the dependence of the polytype transition (discussed in the previous section) and the superconducting critical temperature on applied pressure. These dependencies are presented in Figure 1.9.

For the molybdenum-rich compound, an enhancement of the critical temperature (T_c) was observed with increasing pressure, while the temperature range of the low-temperature polytype was suppressed. In contrast, adding tungsten to the system stabilized the T_d polytype over a broader temperature range, but suppressed the superconducting state. The tungsten-rich compound exhibited no superconductivity up to 18 kbar. This simple isoelectronic substitution alters the preferred stacking order of the weakly bound layers, demonstrating how minute changes can significantly impact interlayer interactions and strongly suppress the superconducting transition. The composition of this series of isostructural and isoelectronic compounds acts as a well-defined "tuning knob". By varying the composition, we alter only a limited set of parameters, allowing for deeper insights into the material's properties from both theoretical and experimental perspectives.

The second category involves systems where compositional changes are accompanied by structural and physical alterations. Instead of focusing on substitutional doping like in the first category, we now examine cases where additional atoms are introduced into the compound, occupying new crystallographic sites within the structure. For the sake of conciseness, we exclude in this discussion materials where substitutional doping, often heterovalent, induces structural changes, such as alterations in

lattice symmetry. A prime example of such compositional modification is intercalation, a process particularly common in layered compounds that provide ample, structured space between the layers for intercalants. It is important to note that this process is not merely a simple geometric insertion of new atoms into vacant sites: the addition of new elements alters the electron count and chemical bonding within the material. These charge modifications can also lead to significant changes in both the electronic and crystal structures due to interatomic interactions. However, the latter cases are not the focus here.

The world of intercalated compounds is vast, and intercalation serves as a crucial tuning mechanism for quantum materials.[93] In the following, the focus is on a specific group closely related to the materials discussed in Chapter 6. Intercalated layered transition-metal oxides A_xMO_y (A—intercalating species, M—transition metal, O—oxygen) represent a broad group of functional materials which are particularly interesting for battery applications due to their high capacity and high energy density.[94] These oxides efficiently store charge by intercalating ions into the interlayer vacant sites of the bulk material. This structural flexibility is facilitated by reversible change of the transition metal's oxidation state, thereby accommodating the charged species. The most common intercalants, A, include alkali metals (Li, Na, K), alkaline-earth metals (Ca, Ba), structural water, or organic molecules.

Alkali-metal intercalated cobalt oxides often referred to as cobaltites, and in particular Na_xCoO_2, have attracted significant attention in condensed matter physics due to its remarkable transport properties. The electronic configuration of Na_xCoO_2 is highly tunable by the amount of intercalated Na (x), resulting in different degrees of electronic band filling. Experimentally x can be varied in a wide range by varying synthesis parameters (Figure 1.10).

Na_xCoO_2 ($0.65 \leq x \leq 0.75$) has a high thermopower and a high thermoelectric figure of merit (ZT) exceeding 1,[97] despite having a metallic carrier density two orders of magnitude higher than traditional thermoelectrics. The high thermoelectric performance of Na_xCoO_2 arises from the combination of narrow bands, metallic conductivity when doped, and moderate thermal conductivity.[98]

$Na_{0.5}CoO_2$ exhibits a metal-insulator transition at $T = 53\,\mathrm{K}$ due to charge-ordering behavior.[95] At lower Na content ($x < 0.5$) metallic Na_xCoO_2 demonstrates correlated electron properties: the hydrated monolayer $Na_{0.35}CoO_2 \cdot 1.3H_2O$ and bilayer-hydrated $Na_{0.42}CoO_2 \cdot 1.3H_2O$ are both superconducting with critical temperatures of $5\,\mathrm{K}$[96,99] and $4.25\,\mathrm{K}$,[100] respectively (Figure 1.10). Interestingly, the triangular cobalt-oxygen lattice is chemically and structurally analogous to the well-known copper oxide high-T_c superconductors. Applying the same model used for cuprates to the cobalt oxides under consideration, the picture of electron correlations may look as follows: the parent CoO_2 hosts the Co^{4+} ($[\mathrm{Ar}]3d^5$) state, with one unpaired electron ($s = 1/2$). Upon Na intercalation, electrons are doped into this orbital, reducing the x portion of cobalt atoms to the Co^{3+} ($[\mathrm{Ar}]3d^6$, $s = 0$) state. This scenario describes Na_xCoO_2 as a doped spin-1/2 Mott insulator, similar to the cuprate case. However, experiments show that electron correlations disappear in pristine CoO_2, which behaves as a conventional metal due to its three-dimensional crystal lattice.[101] The highly two-dimensional structure of intercalated Na_xCoO_2 is therefore an important prerequisite for the appearance of electronic correlations. Another example that highlights the importance of enhanced two-dimensionality for electron correlations in intercalated transition-metal oxides is that water intercalation into non-correlated Na_xCoO_2 induces spin fluctuations and leads to the superconducting state.[96,100]

While physics-focused research often treats all Na_xCoO_2 and their derivatives as hexagonal structures within the $P6_3/mmc$ space group, the reality is more complex. Several polytypic modifications are stable, depending on temperature and intercalant content. These hexagonal, trigonal, and monoclinic polytypes differ in their stacking sequences of identical layers, offering various coordination environments for the intercalated Na ions.[102] Experimentally, a surprisingly intricate variation in Na ordering patterns across the range of x has been observed. However, the potential influence of these stacking orders on the material's electronic properties remains largely unexplored. Such a study would be highly challenging due to the difficulty of accurately determining lattice symmetries and dealing with phase separation among the different polymorphs.

To conclude, the *composition, structure, property relationship* remains an important guiding principle for materials design, which should not be overlooked. Especially, in the cases when a

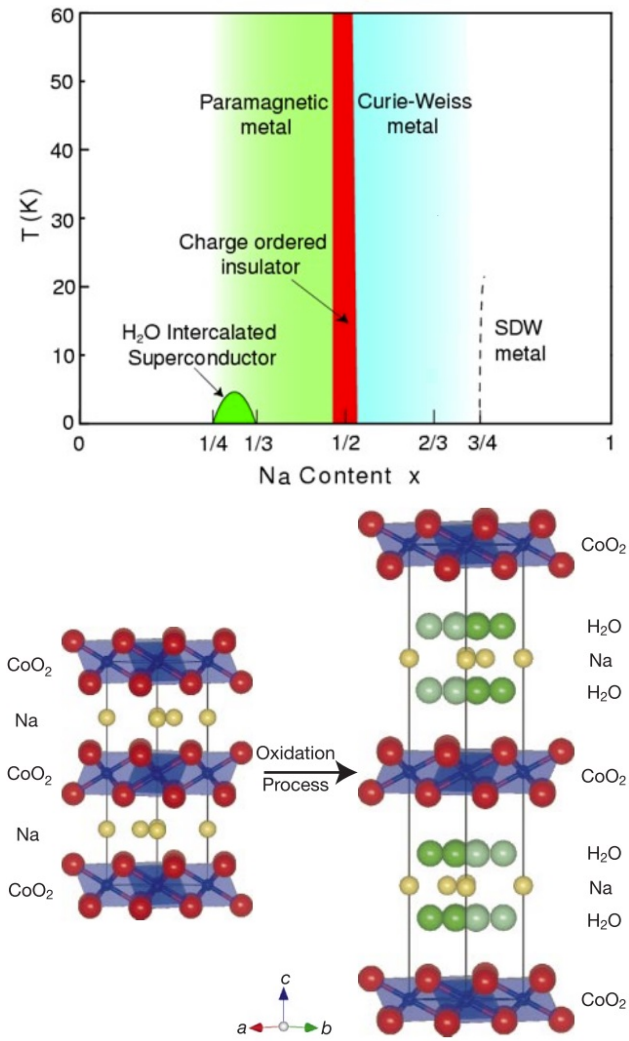

Figure 1.10: Phase diagram of nonhydrated Na_xCoO_2. Structures of intercalated Na_xCoO_2. Figures from Foo et al., Takada et al.[95,96]

material in question is mostly interesting due to its unconventional electronic properties. A change in composition may influence the electronic structure in a straightforward way by adjusting the carrier concentration, e.g. by means of doping or changing the SOC strength. Alternatively, it may induce minute changes in the crystal structure of the solid in question and, therefore, lead to an altered electronic band spectrum.

The structure should be carefully assessed, especially, in the case of topological semimetals, as failure to detect an inversion center could result in an incorrect type of TSM in the theoretical band structure. Those electronic structures, in turn, are widely used to interpret experimental findings and may bias interpretation of experimental spectroscopic data such as ARPES. Thus, expertise in crystal chemistry and crystallography is vital for conducting an adequate theoretical assessment of the material, and, in turn, for an interpretation of experimental studies of emergent physical phenomena.

Next, we move on to the question that was carefully avoided in the present chapter: how to synthesise a compound with the desired composition and structure, preferably, in the form of a single crystal, so its potential fascinating electronic properties can be further studied.

Chapter 2

Synthetic Approaches

This chapter largely based on West[20] and Atkins et al..[23]

The previous chapter presented at length how the minute changes to composition and structure of the material may make or break the topological properties. Experimental studies of the electronic properties of a given material are impossible without the real material in hand.

These two facts present a challenge for material synthesis: a targeted single crystal growth or powder synthesis experiment has to be employed, with its outcome aimed at one specific structure and a tightly controlled chemical composition. This endeavor is additionally complicated by the fact that strong SOC is a prerequisite for topological materials and TSMs, in particular. This, translated to the domain of chemistry, means that material candidates should contain heavy elements with a high atomic number Z. These elements may adopt many oxidation states and have a rich chemistry, which often translates to an abundance of polymorphs, solid solutions, off-stoichiometry and other phenomena, strongly complicating targeted synthesis. The latter needs, therefore, tight control of the varied experimental parameters. Simultaneously, the phase space of these synthetic parameters can be very rich.

Luckily, inorganic chemistry has developed a vast palette of synthetic approaches for compounds with heavy elements. Suitable parameters for these techniques can be either chosen by navigating a "map" through this chemical landscape *(phase diagrams)*, or, if one finds themselves in a new blank spot on that map, by using rules that constrain your choices from the experimental data *(phase rule)*. The rest of the chapter introduces these concepts and illustrates how they guide experimental design, crystal-growth and powder synthesis of high-quality quantum materials.

2.1 Phase Equilibria and Phase Diagrams

Phase diagrams represent thermodynamically stable phases (or mixtures of phases) and their relations, i.e. reactions between phases, as a function of temperature, composition etc. Even though phase diagrams give no information on the kinetics, they are still a vital tool to gain understanding of the synthesis process. If the phase diagram is available for the system under question, it helps to predict the effect of temperature or charge composition on the reaction's course. In case where there's no phase diagram published, the thermodynamic constraints can be used to simplify the search for the right synthesis conditions during "lather-rinse-repeat"-style optimization.[20]

To formalize the description of phase equilibria in a *system*, i.e. a range of compositions in question, we need to define a *phase*, a *component* and *variance* of the system. One defines a *phase* of a substance as a form of matter uniform throughout in chemical composition and physical state. The "physical state" also includes the crystal structure of the phase, e.g. carbon and diamond while being two solids with identical chemical composition will still be two different phases. A *component* is a chemically independent constituent of the system. *Variance* of the system is the number of intensive* variables (e.g. temperature, pressure) that can be changed independently without affecting number of phases at equilibrium. Variance is also often referred to as amount of the *degrees of freedom*.[104]

*Physical quantity whose magnitude is independent of the extent of the system.[103]

The *phase rule* relates the number of phases at equilibrium P to the number of components C and the variance of the system F by equation:[20,104]

$$P = C - F + 2 \tag{2.1}$$

In many situations in solid state synthesis conditions are close to isobaric at ambient pressure, and influence of the difference in pressure between different setups (i.e. labs at different elevation) on the solid state synthesis is negligible. In this conditions pressure is not a variable, so one can reformulate Eq. 2.1 as the *condensed phase rule*:[20]

$$P = C - F + 1 \tag{2.2}$$

Since in this model we consider pressure a constant, we loose one intensive variable, and hence we loose one degree of freedom.

The condensed phase rule alone already puts a simple set of useful constraints to help with determination of synthetic strategy and interpretation of experimental results. If, for example, we take a two component system, Eq. 2.2 could be rewritten as $P + F = 3$, which already gives us general rule regarding system reaction to different perturbations. If we have a single phase at equilibrium, the system is *bivariant*, i.e. both composition and temperature could be changed independently. This will correspond to a 2D field on a diagram. In a contrived example in Figure 2.1 the example of such field is "Liquid": both composition and the temperature of this liquid can be changed independently, while the sample stays a single phase of melt of A and B mixture. More hands-on example would be if we have two phases, e.g. crystals in equilibrium with the solution: In this case we are in *univariant* regimen, since a change in temperature will result in a change of the composition of solution due to crystals either dissolving or precipitating, represented by a line on a diagram. Consider the equilibrium of A_2B with the liquid phase along the liquidus (purple line in the phase diagram): a change of temperature will result in a shift of the solid:liquid phase ratio along the liquidus line, and vice versa: shift of the composition of the solution will change the equilibrium temperature. This naturally leads to a limit of phases that can be in equilibrium in 2-component system: namely three. At this point we've lost all degrees of freedom, change of any variable would change amount of phases in equilibrium, which is naturally represented in the diagram by a single point. In our contrived example one of such a points will be the *eutectic point* for A + A_2B mixture, represented by a point where liquidus touches the horizontal *solidus* line above A + A_2B two-phase field. If we starting at this point, change in temperature will result in either condensation of the liquid phase, or dissolution of the solid phases' mixture, hence, in this configuration we have no intensive variables that we can change without affecting phase composition of the sample. Knowing the number of components in the system, and measuring the number of resulting phases one can draw conclusions if system has reached equilibrium or not, or how the variables could be changed to affect the result. In our example if we somehow end up with the sample that contains four phases, we know that we didn't reach thermodynamic equilibrium. Or, if aiming at crystallization of pure AB_2 from solution we end up with mixture of AB_2 and B, we can conclude that our starting composition was too B-rich, and the system crossed the liquidus line too far right on the phase diagram.[20,104]

Phase Diagrams as a Tool for Synthesis Strategy Determination

Phase diagrams practically map out all phase equilibria in the corresponding system. Even though phase diagrams are constructed using only thermodynamic information, and do not provide information about the kinetics, they still can be used to predict evolution of the system as e.g. function of temperature, assuming a quasi-static process.[20,104]

Since a full explanation of the theory behind the mapping and reading of a phase diagram would require quite lengthy elaboration of physical and solid sate chemistry background, this section will focus on phase diagrams as a tool in the process of determination of synthesis strategy based on a typical example. We consider the phase diagram presented in Figure 2.1. This binary phase diagram, shows two compounds between A and B: A_2B and AB_2. A_2B melts congruently, while AB_2 decomposes peritectically. A and A_2B, as well as A_2B and AB_2 form an eutectic. Since typical

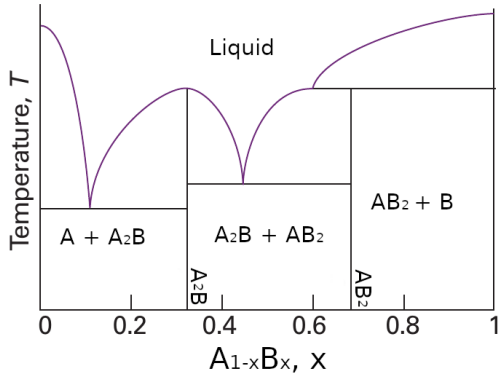

Figure 2.1: A sample binary phase diagram with a congruently melting compound A_2B, an incongruently melting compound AB_2 that decomposes peritectically, as well as two eutectic points. Adopted from West.[20]

synthesis takes plase in a closed system, the elemental ratios stay constant, usually the problem of accessing the right phase is about finding a cooling curve, i.e. a vertical line on the diagram, from which one can extract a phase-pure sample of the desired compound. For example, to obtain a pure sample of A_2B from the melt it is enough to start with stoichiometric composition above the melting point, to alleviate the solid-state diffusion constraints (which will be further discussed in Sect. 2.2), after which this mixture could be cooled directly. In this case, as soon as we cool down to the melting point, we come to an equilibrium point in the phase diagram, and the desired compound will start to precipitate from the melt.

In case of AB_2, cooling of the stoichiometric composition would result in reaching the univariant liquidus line above the compound's temperature of decomposition. As soon as we reach the liquidus line variance of our system is decreased to 2, and we "lock in" on the line during the cooling. This results in shift of the liquid phase composition towards A-rich side, with precipitation of pure B as a solid phase. The precipitation of AB_2 wouldn't start until we reach the decomposition temperature, so in case of stoichiometric mixture one will contaminate the desired AB_2 phase with B. In this case as starting composition for synthesis of pure AB_2 one should choose something in the range of liquidus line that corresponds to equilibrium between the AB_2 solid phase and the melt, i.e. a shift in the composition towards the A-rich side.

2.2 Solid State Powder Synthesis

Thermodynamically, as discussed in Sect. 2.1, to form a compound we just need to expose stoichiometric mixture of the elements to conditions at which the phase is thermodynamically stable. However, thermodynamics doesn't deal with kinetic aspects of the process, so even though the desired phase has the lowest energy in a given set of conditions, the process can be slowed down beyond any practicality by either the activation energy (e.g. H_2–O_2 mixture at standard conditions) of the process, or the diffusion (e.g. FeS would ignite spontaneously in the air, but only in the form of fine powder).[20,23,104]

Diffusion between two solid phases is usually the slowest out of any other combination of state of matter, so during solid state synthesis most of the effort is going towards alleviating effects of it. The overall course of the reaction could be accelerated via increasing the volume to interface ratio, and increasing the temperature. The former can be achieved by grinding down the starting components, or using commercially available fine mesh powders which increases the surface to volume ratio and, in some cases, provides mechanical activation energy to ease the tip over the activation energy. These fine powders could then be thoroughly mixed, or grinding can be preformed *in situ*, to achieve the maximum surface of the interface between phases. The diffusion coefficient is quite often obeys the

Arrhenius formula:

$$D = D_0 \exp\left(-\frac{\Delta H}{RT}\right), \tag{2.3}$$

and depends on the temperature exponentially. So, increasing the temperature to increase the solid state diffusion speed is very effective. In experimental reality this means that to achieve maximum reaction speed, the best temperature to carry out the synthesis is one close to upper limit of desired phase stability. That way we insure the formation of desired phase (due to it being most favorable under the conditions selected), as well as completion of the reaction in a reasonable time, with phase-pure equilibrium sample as the result of the synthesis.[20,23,104]

It is also worthwhile to mention that in limited cases even single crystal growth is possible by this method via subsolidus abnormal grain growth.[105–109] But in general this only viable in a limited list of systems under specific conditions.

In this work, solid state synthesis was carried out in Nabertherm box furnaces or Gero tube furnaces. As a container, evacuated quartz silica tubes were employed. All the quartzware was cleaned with commercially available detergent (Fit), rinsed with deionized water and baked out at 800°C overnight, to avoid any contamination. Reagents employed in the synthesis were in a form of a fine-mesh powder, and were mixed thoroughly by grinding in a agate mortar. Atmosphere sensitive reagents were handled, and silica tubes were filled in a dry argon glovebox. After filling, the ampules were evacuated to $\approx 10^{-4}$ mbar and sealed to prevent oxidation during synthesis.

2.3 Solvent Single Crystal Growth

Kinetic Considerations

For detailed studies of structure or physical properties the samples in the form of single crystals are preferable. To perform growth of a single crystal material in addition to the constraints outlined in Sect. 2.1 and 2.2, we need to lay out additional kinetic constraints. When the solid phase precipitates from a solution, there's an energy barrier associated with free energy of the created phase boundary. This leads to overcooling of the solution below the single liquid phase stability boundary, after which spontaneous nucleation occurs. Nucleation can occur by itself, but quite often happens on "catalytic amounts of dirt", i.e. on some impurities or container surface imperfections that lower the free energy of formation of initial nuclei. After the nucleation has happened, together with formation of the phase interface, the nuclei start to grow, since with addition of stable phase volume free energy decreases faster than energy gain of the formation new surface. Decrease in Gibbs free energy associated with the volume and increase of free energy associated with the surface evolve as $E_{volume}(x^3)$ and $E_{surface}(x^2)$ correspondingly.[20,23,104]

Another consideration is the speed of the cooling after precipitation has started. During the growth of the single crystal the material needs to diffuse from the volume of the liquid phase to the interface, adsorb on the surface, and incorporate itself into the crystal structure. With a fast rate of cooling, this process can become diffusion-limited or adsorption-limited, resulting in a gradient of concentration, which could lead to more spontaneous nucleation in the volume of the liquid phase. Since, assuming we started with fully melted material, the total amount of the precipitate is only dependent on the temperature at which cooling ends one of the priorities of single crystal growth process is to limit nucleation. By lowering the number of individual nuclei, we end up with fewer, but bigger and less defect-ridden crystals. Another consideration is crystal quality: lower speed results in enough time for diffusion at the interface to take place. This lowers the defect concentration of resulting crystal.[20,23,104] In case of a laboratory synthesis, this is, of course, a balancing act, because while often bigger and less defect-ridden crystals are favorable, the crystals need to be obtained in reasonable time.

Solvent Selection

Selection of solvent (or *flux*) is an important step during synthesis planning. As we have seen in Sect. 2.1, sometimes congruent crystallization of the compound is possible, where solvent is not needed

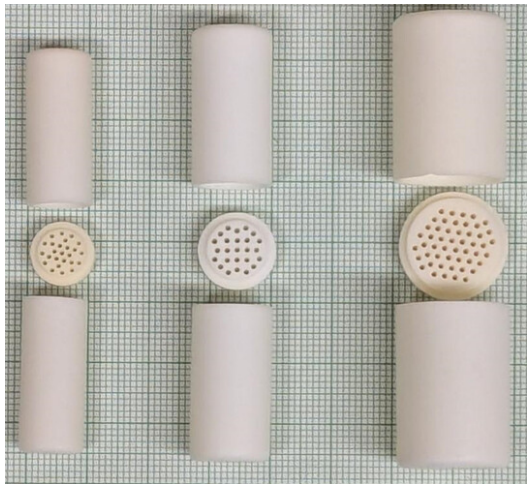

Figure 2.2: Three Canfield crucible sets of different sizes. Figure from Canfield et al.[110]

per se, but then crystallization has to happen at a nonvariant point in the phase diagram, and we don't have control of precipitation speed with temperature. Adding flux can lower the crystallization temperature, avoiding possible "container problem", i.e. absence of suitable container material for required conditions, as well giving us control over the crystallization kinetics. Quite often a *self-flux*, i.e. a component of the system, is a favorable solvent, since it helps to avoid contamination of the desired phase with third-party elements.[20,23,104]

In this work, as a general consideration for single crystal growth all the containers in contact with reaction mixture were cleaned thoroughly both chemically and mechanically. After, all the quartzware was baked out at 800°C overnight, and all ceramics at 1000°C overnight, to ensure absence of adsorbed impurities or residuals of cleaning agents, to avoid contamination or unwanted nucleation centers. The reaction mixtures were thoroughly homogenized to avoid any concentration gradients on heating. To ease the flux separation from the crystals, some growth runs were carried out inside of the frit-disk crucibles, shown in Figure 2.2, commonly referred to as Canfield crucible set. This facilitated flux separation by high-temperature centrifugation.[110]

Chapter 3

Methods

Introduction chapter highlights importance of the *composition, structure, properties* chain in materials chemistry, and previous chapter deals mostly with acquisition of the sample with desired composition and structure. In experimental reality we don't control many factors of the experiment, e.g. 100% pure reagents and furnaces with infinitely precise temperature control are subject of science fiction. Kinetic considerations add another layer of complexity, and differ strongly per experiment. So even when working with well-studied systems which have a trustworthy phase diagram published, control of composition and structure is essential. This chapter gives a whirlwind tour of main methods used in present work to study the composition and structure of the materials synthesised, with main focus on scanning electron microscopy and X-ray diffraction, with a short mention of other experimental analysis methods employed in this work.

3.1 Scanning Electron Microscopy

Scanning electron microscopy (SEM) is a vital tool in material synthesis, which allows for simultaneous characterization of both relatively local and general composition and topography of single crystal samples. In a SEM setup, the sample is scanned by the primary electron beam generated inside of the machine, and scattered electrons and/or radiation produced in this interaction is detected as a function of beam position on the sample in the form of rasterized image. The beam-sample interactions are presented schematically in Figure 3.1. When the primary beam hits the sample, the electrons from primary beam interact with pear-shaped volume of the sample with the size of the order of $1\,\mu\mathrm{m}^3$. Primary electrons can either scatter elastically, or interact with the sample while losing energy, producing electromagnetic radiation or secondary particles. Of particular interest among them are back-scattered electrons (BSE) providing chemical contrast, secondary electrons (SE) giving topographic information, and X-Ray radiation, containing spectral information which helps to spatially map the elemental composition of the sample.[111]

In this subsection we discuss the experimental applications and data that can be extracted from BSE, SE and X-Ray radiation, while assuming "perfect" experimental conditions, e.g. flat and well-conducting sample with primary beam impinging perpendicular to the surface of a sample.

Back-Scattered Electrons

BSE are electrons that undergo enough scattering events to reverse their trajectory by an angle close to 180°, and exit the sample in the general direction of the primary beam source. The BSE can carry information on composition, topography, mass thickness, and crystallography. We focus here on aspects regarding the elemental composition. Intensity of the BSE can be characterized by backscatter the coefficient

$$\eta = \frac{N_{\mathrm{BSE}}}{N_{\mathrm{P}}}, \tag{3.1}$$

where N_{BSE} is the number of BSE, and N_{P} is number of electrons that enter the specimen from the primary beam. The backscatter coefficient η is proportional to atomic number as third-degree

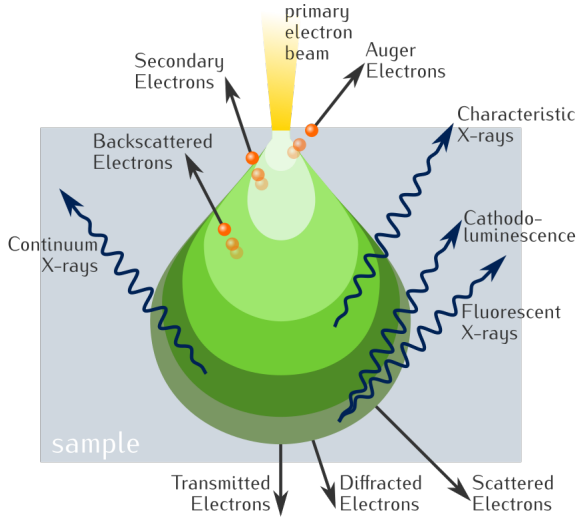

Figure 3.1: Schematic of interactions of electron beam with a sample inside of a SEM. Figure courtesy of Ref. [112]

polynomial, so intensity of BSE rises with atomic number. And, the backscatter coefficient of the mixture of different atoms can be expressed as[111]

$$\eta_{\text{mixture}} = \sum_Z \eta_Z C_Z, \tag{3.2}$$

where η_Z is backscatter coefficient of the element with atomic number Z, and C_Z — element's mass fraction in the sample. This dependence of the fraction of backscattered electrons gives rise to *Z-contrast*, which is sensitive to the average atomic number in the specimen being analyzed. When we scan along the surface of the specimen with a constant flux of electrons in primary beam, locations with different concentration of heavy elements, i.e. with different average Z, would result in different BSE intensity. The contrast between two points with η_1 and η_2 backscatter coefficients (which are related to the amount of BSE by Eq. 3.1 and 3.2), can be expressed as:[111]

$$C_Z = \frac{|S_1 - S_2|}{S_1} = \frac{|\eta_1 - \eta_2|}{\eta_1}, \tag{3.3}$$

where S_1 and S_2 is intensity of the signal from different points.[111]

Experimentally, the dependence shows up as difference in brightness in the resulting BSE image — the higher average atomic number Z of the point, the higher the brightness of the resulting pixel of the image. This is an important tool that can directly reveal phase separation or concentration gradients along the surface of the sample or absence of thereof, limited by microscope resolution.[111]

Secondary Electrons

SE are created when primary beam electrons scatter inelastically and eject conduction band (for metals) or valence electrons (for ionic or covalent compounds) which are weakly bound in the samples, with binding energies of $E \approx$1–15 eV. Some of these electrons are emitted from the sample, which can be detected in the sample chamber of a SEM. Due to large mismatch in relative velocities of incident primary beam and weakly bound sample electrons, energy transfer to SE is rather small, so electrons of this type exit the sample at energy of several electronvolts. Due to this low energy, the SE can be efficiently collected by the detector by applying electrostatic field inside of SEM setup.[111]

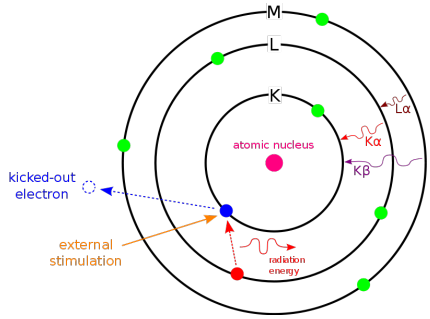

Figure 3.2: Schematics of characteristic X-ray generation process in SEM. Figure courtesy of Ref. [114]

The measured rate of emitted SE is strongly dependent on surface tilt, i.e. on angle between primary beam and the surface of the sample, as was shown by Koshikawa and Shimizu.[111,113] This results in strong dependence of measured intensity on sample surface topography. This helps to visualize the sample at higher spatial resolution than optical microscopy can enable. Coupled with Z-contrast, SE images help to attribute possible artifacts in BSE images to topography of the sample.[111]

Energy-Dispersive X-Ray Spectroscopy

When the primary electron beam hits the specimen, a variety of X-ray signals is generated. Among them are Bremsstrahlung (Continuum X-rays), fluorescent X-rays, and characteristic X-rays. Of particular interest are characteristic X-rays which is the signal analyzed during EDX. As the name hints, characteristic X-rays are generated at specific energies for each distinct element of the sample. During interaction with the primary beam an atom in the sample might lose one of its strongly bound electrons from an inner shell. If, for example, the electron from the K-shell gets kicked out, the atom is now in an excited state, and one of the ways to lower its energy would be for an electron from the L-shell to drop down to K-shell, while emitting an X-ray photon carrying away the energy difference $E_\gamma = E_\mathrm{K} - E_\mathrm{L}$. These X-rays can be detected using semiconductor X-ray detector, where both the count rate and the energy of the X-ray photons are registered.[111]

The transition giving rise to the X-rays is unique for the relevant core levels of each element, thus the atomic identity behind the X-ray energies are simply tabulated. Consequently, after the measurement, the spectral line positions and intensities can be fitted and compared with known standard intensities, after which the elemental composition of the measured area can be determined. This provides an opportunity to measure the sample composition both locally, with lower limit being the excitation volume in the sample, as well as over a large area.[111]

The big advantages of SEM is that spatially resolved EDX data is being collected *in situ* with imaging, which provides both Z and topographic contrast, with low time and effort cost of sample preparation and fast turnover. This simplifies attribution to features in the image to composition, and allows to to study composition of any peculiarities discovered in imaging, enabling e.g. study of phase separation or concentration gradients in relation to the sample topography. This is an invaluable tool to gain insight not only into the specimen composition, but also into the process of the growth itself.

In this work, SEM imaging both in BSE and SE modes as well as EDX was performed on Zeiss EVO MA 10 microscope with incident beam energy of 20–30 keV. For single crystal measurements, the crystal was mounted on the sample holder with conducting carbon-based adhesive tape, after which some crystals were cleaved with commercially available Scotch tape to obtain a fresh surface. The imaging was then performed both in SE and BSE mode at the same magnification, which allowed both to record any composition gradients and investigate sample topology, as well as to compare features in both types of contrast to assess any topography artifacts in Z-contrast images. The

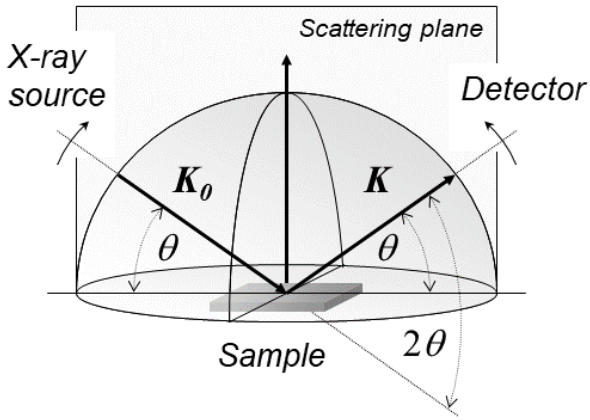

Figure 3.3: General scheme of the diffraction experiment. Figure courtesy of Ref. [115]

investigation was done over the whole sample at first, after which identified regions of interest were studied at higher magnification. The EDX measurements were preformed at around 10 points, each point uniformly spaced over measurement area. In addition to point analyses also spectra were taken from wide areas of the crystal. Final compositions were calculated assuming Gaussian statistical error in each individual measurement. In this work the standard deviation in the least significant digit is presented in brackets, where applicable.

3.2 X-Ray Diffraction

After the composition of our specimen is obtained from SEM data with added bonus of imaging in Z and topographical contrast, structure of the sample needs to be studied. Solid state materials feature high periodicity, which allows for a wave with a wavelength similar to the interatomic distance to diffract on the atomic lattice, which acts as a diffraction grating. These scattered waves carry a lot of information about the arrangement of the atoms in the material, as well as types of atoms therein. X-ray diffraction is a widely employed method for structure determination and refinement. It uses monochromatic electromagnetic radiation with wavelength on the order of $\lambda \approx 1$Å as the light source, widely available in the laboratory setting, and allows for in-depth study of not only study of the structure of the specimen, but in case of powder diffraction, also phase composition. The following section lays out the basics of the powder x-ray diffraction (PXRD).

General Principle

Since crystalline material is highly periodic, it can be studied by diffraction of electromagnetic waves. We can consider scattering of X-Ray radiation on every atom of the specimen as isotropic and elastic. Given that our crystal lattice has primitive translation vectors $\mathbf{a}$, $\mathbf{b}$, and $\mathbf{c}$, wavevector of a primary X-ray beam $\mathbf{k_0}$, and wavevector of the diffracted beam $\mathbf{k_d}$, we can write down the constructive interference condition in the form of the *Laue equations*:

$$\mathbf{k} \cdot \mathbf{a} = 2\pi h, \tag{3.4}$$

$$\mathbf{k} \cdot \mathbf{b} = 2\pi k, \tag{3.5}$$

$$\mathbf{k} \cdot \mathbf{c} = 2\pi l, \tag{3.6}$$

where $\mathbf{k} = \mathbf{k_d} - \mathbf{k_0}$ is a *scattering vector*, and h, k, and l are integers, called *Miller indices*. This directly ties the spatial positions of the diffracted peaks on a detector in the far field relative to

the sample and the primitive lattice parameters of the structure. In case of a powder measurement we lose some spatial resolution, due to rotational averaging caused by random orientation of every crystallite inside of a specimen. Due to this we lose some point group symmetry information, but can still extract the crystal system and lattice parameters from diffraction peak positions and some information about open symmetry elements from peaks absent due to reflection selection rules.[20,25,63]

In a laboratory diffraction experiment, this translates to X-Ray generation in a diffractometer by an electron beam hitting a target material. Copper, cobalt, molybdenum or silver being the most common. During that process one of the characteristic X-Ray radiation lines of the target material is selected using a monochromator. The resulting X-Ray radiation used for diffraction has a wavelength on the order of $\approx 1\,\text{Å}$. Next, the monochromated X-Ray beam is collimated, and brought to the specimen. The diffracted beams, that are either reflected from or transmitted through the sample depending on the device geometry, are recorded at the detector.[20,25,63]

In this work powder X-ray diffraction measurements were performed on STOE STADI diffractometer. The material was ground by hand in agate mortar, after which it was mixed with glue and transferred to the sample holder. The samples were measured in Bragg-Brentano transmission geometry, $2\theta : \omega$ scan, Co $K_{\alpha 1}$, Mo $K_{\alpha 1}$, or Cu $K_{\alpha 1}$ radiation, using a curved Ge monochromator. With Co and Cu radiation typical 2θ scan range was 10–110°; for Mo radiation — 5–55°. Samples were scanned 2–3 times over the desired 2θ range, after which the scan ranges were added together in the WinXpow software package.

Phase Analysis and Indexing

Miller indices of the reflections can be selected by brute force, i.e. by guessing the indices until all peaks are indexed. The primary beam wavevector is a known value from the experimental setup, and the diffracted wavevector can be inferred from the angle at which reflection was measured. From this, one of the diffraction peaks can be assigned the Miller indices by educated guess, e.g. in general the most intense peaks are usually have low indices. After that, the lattice parameters can be inferred from the position of this peak and the expected position of other peaks in the diffraction pattern can be calculated via the Laue reflection conditions. Further, the calculated diffraction peaks can be compared to experiment, and conclusion can be drawn if the indices are assigned correctly. This process is repeated until a matching set of indices is found for every peak.[25,63]

Additionally, the positions and intensities of the diffraction peaks of most known crystalline phases are deposited in the crystallographic databases, or can be calculated easily from a crystal structure model. This allows to identify the known phases quickly in the diffraction experiment, making it a vital tool for the quick analysis of phase composition of solid state crystalline samples.[25,63]

Indexing step allows to identify known phases in the sample, as well as allows to extract the lattice translation vectors. This gives information on the crystal system in which the phase has crystallized, as well as lattice parameters of the phase in question. Additionally, the presence of open symmetry elements or centering vectors in can be identified by absence of diffraction peaks due to associated reflection selection rules. While at this step we now nothing about the unit cell contents, i.e. atomic positions inside of the material, this can be dealt with employing a full-profile analysis of the diffraction patterns.

Full Profile Analysis

Further information can be extracted by analysis not only of the peak positions, but considering the experimentally acquired intensity vs angle dependence as a whole. In the diffraction experiment, in addition to the basic information carried by Laue conditions, a lot more information is imprinted in the X-rays scattered by the sample. Peak positions and intensity, in addition to lattice parameters, carry information about absorption and porosity of the sample, as well as wavelength, alignment and beam divergence of the instrument. Peak intensity can be used to extract information about atomic parameters, preferred orientation, microstructure parameters such as strain, and absorption of the sample together with configuration and radiation of the machine. Peak shape is affected by crystallinity, disorder and defects in the structure, grain size and strain on the sample as well as beam

conditioning of a machine. Background can give information about the presence and relative amount of amorphous, non-diffracting phases. The instrument effects can be characterized by measuring a standard sample with sample-dependent parameters tabulated by the standardization body that produced the sample, and after that the instrument effects can be separated from effects of a specimen under question.[25,63]

One of most popular methods of full-profile analysis was proposed by Rietveld.[116] In this method, observed diffraction peaks are fitted with so-called peak shape function (PSF), which is a convolution of functions describing the instrumental broadening, wavelength dispersion, and specimen function, which are added to a polynomial describing background. Exact inner workings of the methods are beyond the scope of this introduction, but the method allows to deconvolute many contributions, some of which are presented above, to the diffraction pattern. This allows for calculation of both phase fractions in the sample, as well as enables refinement of the structural model of the material at hand. The result of such refinement is a full structural model, with both unit cell parameters, as well as atomic positions and displacements inside the unit cell. This allows not only to precisely identify the structure of the material, but also study effects of composition on the structure, e.g. continuous structural changes on substitution. On top of that Rietveld refinement enables study of the sample microstructure by estimating strain, particulate size, etc.[25,63]

One of the experimental limitations of X-Ray diffraction in general is inability to focus the X-ray beam. So information carried from the sample to the detector is averaged out over illuminated area. This limits our ability to study materials with e.g. high defect concentration, which causes serious peak broadening. Also, in highly ductile materials standard sample preparation methods introduce a lot of new defects into the crystal structure, sometimes rendering the X-Ray diffraction data unusable for further analysis. One way to deal with this problem is to use a local diffraction method, so the analyzed volume is shrunk to the point where defects stop playing such a prominent role. One of such methods is selected-area electron diffraction (SAED), which is discussed in the following section.

3.3 Selected Area Electron Diffraction

A unique strength of the electron diffraction in a transmission electron microscopy (TEM) setup is ability to focus the monochromatic beam in the single spot. This allows to study the structure of the compound locally, considering only the small volume in the sample, which allows to collect diffraction data from the samples with e.g. high amount of stacking faults, which is common situation in van der Waals materials.[117]

While the guiding principles of the diffraction stay the same as laid out above in Sect. 3.2, there's a set of important differences. Electrons' interaction with matter is stronger than that of X-rays, and, as obvious from the name, in a TEM the only available geometry is transmission through the sample, so sample has to be thin enough. In case of van der Waals materials this is easy to mitigate by repeated cleaving, until sample is thin enough to extract useful signal. At a typical accelerating voltage in a TEM of 100-200 kV de Broglie wavelength of an incident electron is is on order of magnitude of 10^{-3} Å, which is 3 orders of magnitude shorter of a typical lab X-ray with wavelength of ≈ 1 Å. This results in way larger magnitudes of the incident and diffracted wavevectors, and in practical terms allows to project an almost flat cut through the 3D diffraction pattern on a detector, i.e. one doesn't need to rotate the single crystal, or average all the rotations by performing the diffraction on many particulates of a powder. Locality of the measurement, enabled by our ability to focus the beam, on one hand prohibits us from looking at the sample as a whole, allows us to avoid defects such as stacking faults. This not only enables to get structural data in cases where either defects in as-grown sample or defects introduced e.g. during grinding in preparation for PXRD measurement significantly lower the quality of conventional PXRD data, but also allow more close study of the local symmetry. This information is first to be lost in conventional PXRD, so combination of both PXRD and SAED is a powerful tool for structure analysis.[117]

At this point, we laid out state of the art in Chapter 1, know how to get to desired material from Chapter 2, and from present chapter we have a robust way to identify both composition and

structure of our materials. For the remainder of the thesis we'll be dealing with original research in three different material systems.

Chapter 4

$PtBi_2$: Centrosymmetric or not?

This chapter is based upon the publication: Shipunov, G. et al. Polymorphic $PtBi_2$ Growth, Structure, and Superconducting Properties. *Physical Review Materials* **2020**, *4*, 124202[118]

4.1 Introduction

$PtBi_2$ belongs to the materials class of TSM and exhibits an array of fascinating electronic properties. In particular, trigonal γ-$PtBi_2$* is in the spotlight as a promising quantum material due to its giant linear magnetoresistance (MR) of up to 684% at 2 K in a field of 15 T, and 61% at room temperature.[119] The MR in $PtBi_2$ is strongly anisotropic, with a transition between saturating and non-saturating behavior depending on the angle between the external field and the crystallographic [001] direction. Notably, the MR becomes linear at the specific angle of 8.3° with respect to the trigonal axis.[120]

Furthermore, γ-$PtBi_2$ is an attractive candidate for potential spintronics applications thanks to a giant, 3D spin splitting (so-called Rashba splitting) of the bulk bands with Rashba coefficient of $\alpha_R = 4.36\,\text{eV Å}$.[121] Spin-resolved ARPES experiments by Feng et al.[121] observed helical spin textures at the M points in the Brillouin zone of $PtBi_2$ that are enabled by both the strong spin-orbit coupling of high-Z platinum and bismuth and bulk inversion-symmetry breaking. The size of the SOC-induced bulk-band splitting in $PtBi_2$ is one of the largest observed so far, surpassing even 3.8 eV Å for BiTeI,[122] which for a long time was the champion in giant Rashba-type bulk splitting.

The van der Waals nature of the material facilitates the studies of thickness-dependent properties. Monolayer-thick $PtBi_2$ possesses several consecutive hybridized band gaps with topologically non-trivial character in the vicinity of its Fermi energy. Nie et al.[123] coined "multiple topological insulator" for this scenario, in which every such gap is shown to host a robust edge state, by means of STM measurements.

The palette of exotic conducting properties of $PtBi_2$ is enriched by the possibility that it is a topological superconductor.[124] Bulk crystals show superconducting transition at around 600 mK[118,125] with T_c enhancement of up to ≈2 K under hydrostatic pressure higher than 6–7 GPa.[126] Furthermore, in the studies enabled by the research presented in this thesis, a 60 nm γ-$PtBi_2$ flake demonstrated two-dimensional superconductivity ($T_c \approx 370\,\text{mK}$), with signs of a Berezinskii-Kosterlitz-Thouless transition at $T_{\text{BKT}} \approx 310\,\text{mK}$.[125] Investigation of those crystals by STM and ARPES has brought further confirmation of topological superconductivity such as gapping out of the surface Fermi arcs.[127–130] Despite this growing wave of interest in $PtBi_2$ as a quantum material, its chemistry and, especially, crystallography still present open questions due to the rich polymorphism within the system.

A compound with the composition $PtBi_2$ was first reported in 1895,[131] and it caught the attention of physicists as early as the 1950s with the first report of superconductivity in a $PtBi_2$ alloy.[132] Unfortunately, this report does not mention any details of sample preparation or chemical characterization, making it impossible to infer the structure of the compound. Further studies of compounds with this

*If not mentioned otherwise, for remainder of this chapter $PtBi_2$ refers specifically to the trigonal modification γ-$PtBi_2$

composition revealed that $PtBi_2$ has at least four polymorphic modifications, each stable in different temperature ranges.[133] Up to 270°C, the α-modification (space group $Pbca$ №61, orthorhombic system, $AuSn_2$ structure type) is stable. In the 270–420°C temperature range, the β-modification ($Pa\bar{3}$ №205, cubic system, pyrite structure type) is thermodynamically favorable.[133,134] Above 420°C, a polymorphic transition to γ-modification (trigonal crystal family, controversy about the space group, see below) takes place, and this phase remains stable up to 640°C, where the signature of another transformation to the δ-modification is observed. This δ-modification is stable only within a very narrow temperature window, and decomposes peritectically at 660°C, only approximately 20°C above the polymorphic transition.[133,134] This rich polymorphism complicates the synthesis of the desired material. Extra attention must be paid to match the synthesis conditions to the window of thermodynamic stability of the targeted polymorph.

Among this array of polymorphic modifications, two have captured the scientific community's attention due to their emerging topological properties and strong potential for application-relevant transport behavior: cubic β-$PtBi_2$ and trigonal γ-$PtBi_2$.

The former, pyrite-type form has been proposed to be a 3D Dirac TSM[135] with one of the largest observed MR among the known nonmagnetic metals so far, and a unique electronic structure with relativistic fermions identified via Shubnikov–de Haas (SdH) quantum oscillations and the de Haas–van Alphen (dHvA) effect.[136,137] While β-$PtBi_2$ has a crystallographically straightforward pyrite-type fcc lattice, the structure of γ-$PtBi_2$ is itself of significant scientific interest.

γ-$PtBi_2$ is a layered material, where layers of covalently bonded Pt and Bi are held together by weak van der Waals forces. The literature contains two different models to describe the γ-$PtBi_2$ structure: some researchers assume that this compound crystallizes in centrosymmetric $P\bar{3}$ space group,[119,138–140] while others employ the non-centrosymmetric $P31m$ structural model.[121,123,141] The lack of an inversion center in the latter leads to significant alterations in electronic properties compared to the $P\bar{3}$ model, as shown by the results of theoretical band structure calculations. Modelling of the $P\bar{3}$ centrosymmetric lattice finds a trivial metal with a topologically inverted band gap deep in the valence band (-2 eV) that hosts surface Dirac fermions[139] projecting onto the $\bar{\Gamma}$-point of the surface Brillouin zone. However, experimental studies based on this model find Dirac-like states not only at $\bar{\Gamma}$ at $E - E_F \approx -1$ eV, but also at the $\bar{M}$ point at ca. -0.1 eV.[138,140] Calculations assuming the $P31m$ model predict a metallic electronic spectrum with the signatures of Weyl TSM (allowed by inversion-symmetry breaking) with multiple, nearly linear bulk-band crossings in a ± 0.3 eV energy range near the Fermi level.[141] This unique combination of two types of TSM signatures yields triply-degenerate points (TPs) in the band structure. TPs can be viewed as an intermediate state between fourfold degenerate Dirac points and twofold degenerate Weyl points and are highly sought-after as a source of exotic transport phenomena. Particularly attractive is the close proximity of the TPs in the electronic spectrum of γ-$PtBi_2$ to the Fermi energy. A set of type-I Weyl nodes is positioned just 48 meV above the Fermi energy[125] and, thanks to a large separation within k-space, can be the source of large, robust Fermi arcs observed in ARPES.[127] Indeed, this material exhibits pronounced Shubnikov–de Haas (SdH) quantum oscillations with a gigantic MR greater than 1.3×10^5 % without any sign of saturation at 32 T and 1.8 K, and similar oscillations in magnetization due to the de Haas–van Alphen (dHvA) effect.[141] Its rich topological phase diagram and the experimentally observed properties render determination of the correct space group for γ-$PtBi_2$ paramount for further studies of the material.

Detailed studies of the crystal structure of $PtBi_2$ are presented in two reports. The first published structure assumed $P\bar{3}$ space group. Lattice parameters $a = 6.57$ Å, $c = 6.16$ Å were determined from PXRD data indexing.[134] Later, $PtBi_2$ was synthesized by Kaiser et al., where a single crystal sample was made by low-temperature reduction of $Bi_{13}Pt_3I_7$.[142] In this report, the authors solve the structure from SC-XRD data in the space group $P31m$ with lattice parameters of $a = 6.573$ Å, $c = 6.167$ Å, which are practically the same as in the $P\bar{3}$ model. This two models are presented in Figure 4.1. Crystallographically, these two models are very similar, in both cases [$PtBi_6$] edge-sharing octahedra form [$PtBi_2$] layers, and the layers stack on top of each other along [001]. However, in the $P31m$ case the Pt atoms move closer to the 3-fold rotation axis forming equilateral triangles in the structure (compare Figure 4.1 a and c). Bi atom in the middle of the triangle thereby moves into the van der Waals gap, giving a Bi–Bi interlayer distance lower than that of elemental Bi, hinting at stronger interlayer interactions in $PtBi_2$. All of this results further distortion of the [$PtBi_6$] octahedra.

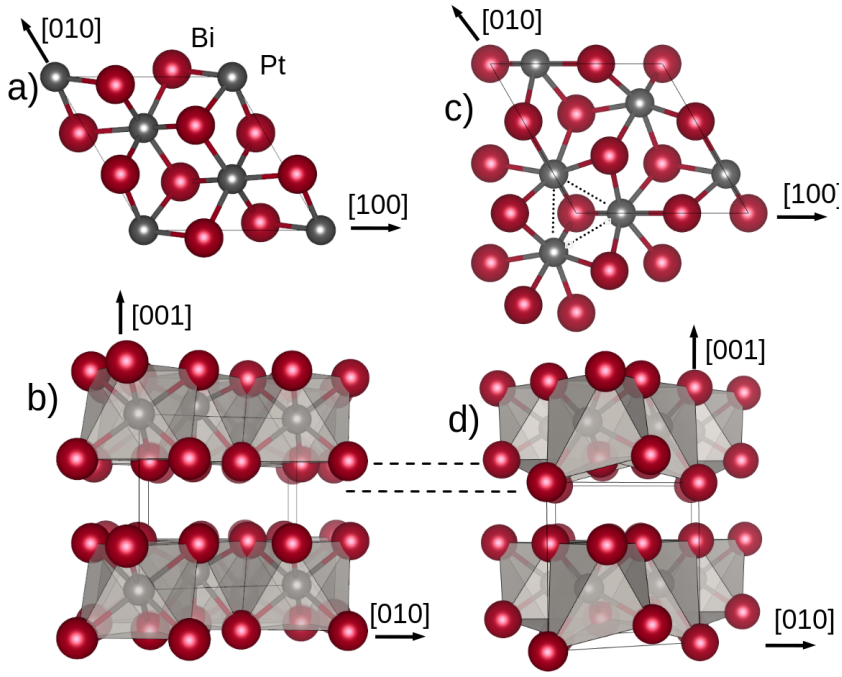

Figure 4.1: Reported crystal structures for trigonal $PtBi_2$: in space group $P\bar{3}$ (a,b),[134] and in $P31m$ (c,d).[142] Dotted lines are highlighting Pt triangles forming in $P31m$ model. Dashed lines are guide for eyes to highlight the corrugation of one of the Bi planes in $P31m$ model.

While this structural motif is unusual, this can be explained by counting electrons: assuming that every atom of the less electronegative bismuth is a $3e^-$ donor, platinum (neutral atom electron configuration $[Xe]6s^14f^{14}5d^9$) has only $16e^-$ in its valent shell. With the addition of two Pt–Pt covalent bonds (resulting in the triangles), the platinum atoms can be considered to each have two more valence electrons, bringing the outer shell electron count to a magic number of 18, i.e. the outer shell of the atom is filled with configuration $[Xe]6s^24f^{14}5d^{10}6p^6$ (isoelectronic to radon).[142]

Most crystals on which physical properties were studied were synthesized via self-flux growth, with crystallization happening in high temperature range, in which γ-$PtBi_2$ is thermodynamically stable.[139] On the other hand, the report by Kaiser et al.[142] employs a "soft chemistry" synthetic approach known to provide access to metastable phases.[143,144] In this light, the discrepancy in the determined space groups for γ-$PtBi_2$ may originate from the more precise structure characterization method (SC-XRD) used by Kaiser et al. or from the low-temperature reduction method, resulting in a new metastable phase of $PtBi_2$. Indeed, the reduction of $Bi_{13}Pt_3I_7$ takes place at $T = 70$°C over two days, 350°C below the lower bound of the polymorph's thermodynamic stability region of 420–640°C. Kaiser et al.[142] leave the mechanism of the reduction as an open question. Therefore the characterization and comparison of "high temperature"-grown crystals, i.e. crystals that are formed at thermodynamic equilibrium, is provided here. These results is of significant interest as it will provide better input for theory models.

The reported targeted synthesis of single crystal γ-$PtBi_2$ employs direct crystallization from a stoichiometric melt. The mixture of Pt:Bi with molar ratio of 1:2 is heated up to 700°C, after which crystallization takes place during cooling to 450°C at a rate of 3°C/h.[139] Although Xu et al.[139] managed to extract $PtBi_2$ single crystals of desired phase in this manner, careful examination of the phase diagram reveals several pitfalls in this growth protocol. First, if employing this method, the rich polymorphism in the system guarantees at least one polymorphic transition of already crystallized

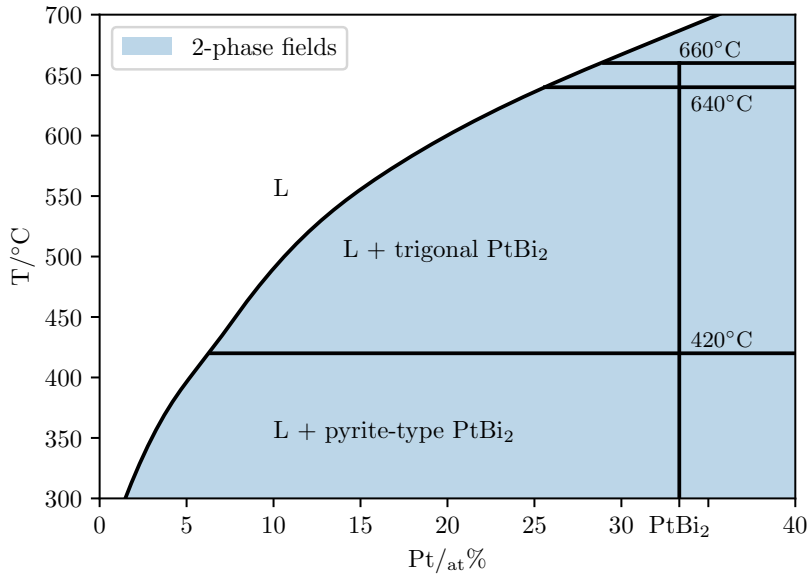

Figure 4.2: Region of Pt–Bi phase diagram adopted from Okamoto.[133] Precipitation zones, where a $PtBi_2$ polymorph can be selectively crystallized from the melt (L) are labeled.

material at 640°C, due to existence of the δ polymorph with a higher temperature of thermodynamic stability. Second, according to the literature, δ-$PtBi_2$ does not melt congruently, but decomposes peritectically to $Pt_{0.67}Bi$ on heating,[133] which should result in contamination of the precipitate with $Pt_{0.67}Bi$ during the start of the crystallization. To solve the problems outlined above, the research presented here was aimed to provide a protocol for the targeted growth of γ-$PtBi_2$.

The phase diagram of Pt–Bi system published by Okamoto[133] shows a precipitation zone for γ-$PtBi_2$, allowing for selective crystallization of the compound via the self-flux technique. For clarity, the relevant region of phase diagram is shown in Figure 4.2. This method allows direct crystallization of γ-$PtBi_2$, avoiding polymorphic transitions and contamination by the phases of different compositions. Since the flux does not introduce new elements to the mixture, we also avoid undesired doping of the crystals.

To recap: γ-$PtBi_2$ has a wide array of interesting physical properties. This diversity of different effects makes the $PtBi_2$ system extremely attractive both for fundamental research and as possible candidate for applications. Meanwhile, the reported synthesis is suboptimal and structural data seems incomplete, posing interesting question about chemistry and crystallography of the material. Understanding the structure is essential for further research into the electronic properties. To remedy this, the present works deals with optimization of the synthesis of trigonal $PtBi_2$, followed up by careful structural reassessment of the material. In parallel, element substitution is also attempted, in search for "tuning knobs" for studying the evolution of the crystal chemistry, and as a consequence, the properties of the material.

4.2 Synthesis

For the crystal growth temperature profile and Pt:Bi ratio were selected in such a way that only trigonal polymorph crystallizes from the solution. Synthesis was stopped before possibility of pyrite-type polymorph formation. To try to alter or tune the properties of the materials substitution at the Pt site was attempted, yielding $Pt_{1-x}TM_xBi_2$. To select the elements, we considered the coordination geometry of Pt position, the electron count on the outer shell and the ability of the substituent to

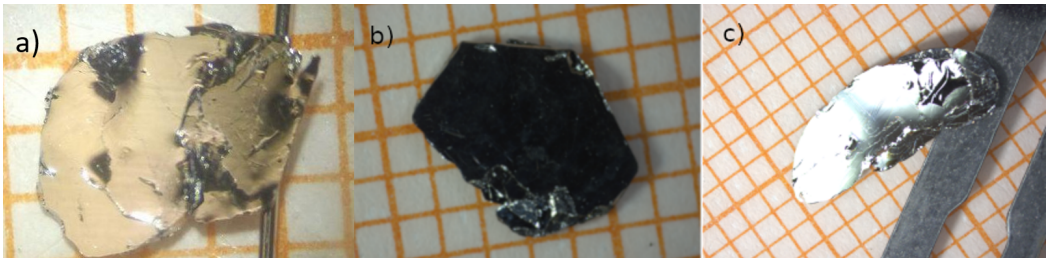

Figure 4.3: As-grown single crystals on millimeter scale background: (a,b) $PtBi_2$, notice the regular 60° edges on the top of (b); (c) crystal of $Pt_{0.65}Rh_{0.35}Bi_2$.

dissolve in the Bi flux. Naturally, the radii of the elements also play a role and due to intermetallic nature of original compound, the metallic radii were the ones considered. For isoelectronic substitution we chose Ni (electron configuraion $[Ar]4s^23d^8$, metallic radius 1.24 Å vs. platinum's $[Xe]6s^14f^{14}5d^9$; 1.385 Å). For non-isoelectronic substitution we settled on Ir ($[Xe]6s^24f^{14}5d^7$, hole doping; 1.355 Å), Rh ($[Kr]5s^14d^8$, hole doping; 1.34 Å), and lastly Au ($[Xe]6s^14f^{14}5d^{10}$, electron doping; 1.44 Å).

Self-flux Single Crystal Growth

Pristine γ-$PtBi_2$ Single crystals were synthesized by first mixing powders of elemental Pt (powder, 99.99%, Saxonia Edelmetalle GmbH) and Bi (325-mesh powder, 99.5%, Alfa Aesar) in a molar ratio of Pt:Bi=1:4. The mixture was then homogenized thoroughly via manual grinding in an agate mortar and then placed into a Canfield crucible set,[110] for easier flux removal after synthesis. The crucible was then placed in evacuated fused silica ampoule to prevent oxidation. This setup was then placed in a box furnace and heated to 850°C at a rate of 100°C/h, and held at this temperature for 10 h to ensure homogeneous melt. After that, the furnace was slowly cooled to 420°C at a rate of 2°C/h, to allow the solid phase to precipitate. Finally, the ampoule was taken out of the furnace at 420°C and quickly placed in the centrifuge to separate the flux from precipitated crystals.

$Pt_{1-x}TM_xBi_2$ The method for single crystal growth of the substituted compounds was mostly the same as for the pristine material described above. Due to absence of data of the phase relations in such ternary systems, the mixture was cooled only to 500°C during growth to avoid precipitation of hypothetical secondary phases. Elements were mixed in the molar ratios presented in Tab. 4.1*, with total charge mass of ≈0.3 g. The mixtures were ground until homogenous in an agate mortar, after which the mixture was put into a Canfield crucible set and sealed inside an evacutated fused silica tube. The growth was carried out in a box furnace, with a hot centrifugation at 500°C immediately after.

4.3 Morphology and Composition

Crystals of $PtBi_2$ were obtained as gray platelets with metallic luster. For clarity, typical as-grown crystals are shown in Figure 4.3. Crystals were obtained in hexagonal tabular habit, the shape of the crystals corresponds nicely to the structure of the desired trigonal polymorphic modification. Edges of the platelets that were not in contact with the crucible walls or did not formed aggregates are demonstrating regular 60° edges. The acquired crystals are extremely ductile. Thin platelets are foil-like under handling. The compound cleaves extremely easily along the shear planes parallel to the face of the platelet, which is in line with van der Waals nature of the crystal structure of γ-$PtBi_2$.

*$Pt_{1-x}Rh_xBi_2$ single crystal compounds where synthesized by Irina Kovalchuk in the course of her Master's project that I supervised.

Table 4.1: Nominal compositions of reaction mixtures and compositions according to SEM-EDX analysis for the obtained $Pt_{1-x}TM_xBi_2$ compounds.

Reaction mixture	SEM-EDX
$PtBi_4$	$PtBi_{2.03(4)}$
Rh substitution:	
$(Pt_{0.9}Rh_{0.1})Bi_4$	$Pt_{0.97(1)}Rh_{0.02(1)}Bi_{1.89(2)}$
$(Pt_{0.7}Rh_{0.3})Bi_4$	$Pt_{0.64(2)}Rh_{0.35(1)}Bi_{1.9(3)}$
$(Pt_{0.5}Rh_{0.5})Bi_4$	$Pt_{0.42(6)}Rh_{0.58(6)}Bi_{1.94(3)}$
$(Pt_{0.25}Rh_{0.75})Bi_4$	$Pt_{0.17(2)}Rh_{0.82(2)}Bi_{1.94(2)}$
$(Pt_{0.1}Rh_{0.9})Bi_4$	$Pt_{0.10(2)}Rh_{0.89(2)}Bi_{1.7(4)}$
Ir substitution:	
$(Pt_{0.9}Ir_{0.1})Bi_4$	$PtBi_2$
Ni substitution:	
$(Pt_{0.9}Ni_{0.1})Bi_4$	See Sect. 4.3 and Tab. A.1
$(Pt_{0.8}Ni_{0.2})Bi_4$	”
$(Pt_{0.7}Ni_{0.3})Bi_4$	”
Au substitution:	
$(Pt_{0.9}Au_{0.1})Bi_4$	$PtBi_2$
$(Pt_{0.8}Au_{0.2})Bi_4$	$PtBi_2$
$(Pt_{0.7}Au_{0.3})Bi_4$	$PtBi_2$

The chemical composition of the crystals was studied via SEM with EDX. For $PtBi_2$, a stoichiometric composition was confirmed. BSE contrast images show uniform surfaces, indicating absence of macroscopic element concentration gradients. In the case of the $Pt_{1-x}Au_xBi_2$ and $Pt_{1-x}Ir_xBi_2$ compounds, substitution didn't result in Au or Ir incorporation. From the published Au-Bi phase diagram,[145,146] one can expect that gold fully dissolved in the flux during the synthesis. Absence of incorporation most probably can be explained by the lower chemical potential for dissolved gold (or iridium) at those temperatures and concentrations.

$Pt_{1-x}Ni_xBi_2$ shows rather peculiar behavior. At low nominal content ($x = 0.1$), Ni incorporates into the crystals, but does so extremely unevenly. One can see nickel content varies anywhere between $\approx 1.5_{\text{mol}}\%$ and $\approx 22_{\text{mol}}\%$ at different places in the same crystal at the scale of a millimeter (See the appendix, Tab. A.1). For nominal $x = 0.3$, the Ni content seems to stabilize, now being uniform inside the crystal, but we observe two kinds of composition, corresponding to approximately 6 and 10 mole percent. For $x = 0.5$, the nickel content is at the lower boundary of detection limit for the device. The uneven distribution at low nominal concentration might be explained by formation of some intergrowth phase. Decrease in the incorporated nickel content with increasing nominal concentration is more peculiar, with one possibility being that increasing the Ni concentration drives the system further to the middle of Pt–Ni–Bi phase diagram, where nickel either stays dissolved in the flux, or precipitates as some other phase that is getting discarded during handling. In any case, from composition studies alone we can conclude that Ni doesn't show conventional solid solution formation with $PtBi_2$. In view of the above, equilibria in the Pt–Ni–Bi system do pose interesting scientific questions, but they are beyond the scope of this work.

In contrast to the Ni case, $Pt_{1-x}Rh_xBi_2$ shows more stable behavior. Crystals in this series resemble those of $PtBi_2$ in color and luster. The habit remains tabular throughout the substitution series, but the shape of the platelets changes. For $Pt_{0.97}Rh_{0.03}Bi_2$ (nominal Rh substitution $x = 0.1$), the platelets still show 60° edge angles. With higher Rh substitution levels, the platelet shape becomes irregular, and by $Pt_{0.1}Rh_{0.9}Bi_2$ becomes elongated rectangular, and flattened, needle like. Examples of whole-crystal SEM pictures can be found in the Appendix, in Figure A.1. Compositions with higher levels of nominal substitution change non-linearly (Tab. 4.1). For example, nominal $x = 0.1$ result in a composition shifted to Pt-rich side of the phase diagram, with only 3% Rh substitution in

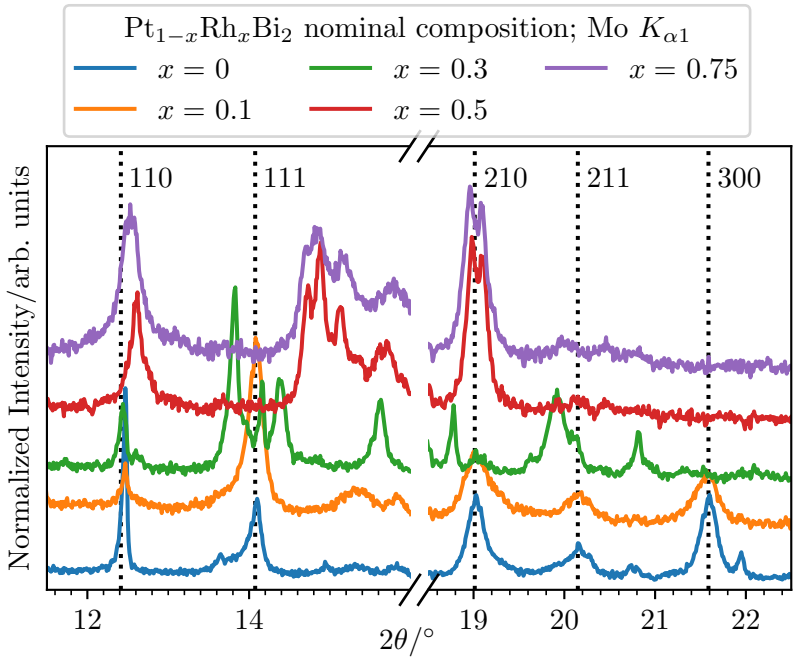

Figure 4.4: Normalized intensity PXRD patterns for $Pt_{1-x}Rh_xBi_2$ series of compounds. Dotted black lines are positions of the well-resolved, high-intensity peaks for $PtBi_2$, with Miller indices labeled ($P31m$ structure model). For clarity curves are offset along ordinate. Unprocessed data is presented in the Appendix in Figure B.1.

the crystals. For nominal $x = 0.3$, we already see a shift in opposite direction, crystals being more Rh-rich than the reaction mixture, corresponding to $Pt_{0.65}Rh_{0.35}Bi_2$ composition. This change in Rh distribution might indicate that system is entering a different crystallization field in the ternary phase diagram, and extra attention should then be paid for qualitative changes during e.g. PXRD analysis. This trend continues up to nominal $x = 0.9$, at which point relative Rh content of the crystal is approximately the same as in the melt.

4.4 Crystal Structure

To get the first glimpse at the crystal structure, PXRD from crushed crystals single was employed. The as-grown aggregates of crystals of $PtBi_2$ and $Pt_{1-x}Rh_xBi_2$ were ground by hand in agate mortar, after which the powder was transferred to the sample holder, wetted with x-ray glue. The reflections in the diffraction pattern from crushed aggregates are abnormally broadened, signal-to-background ratio is rather poor, and the resulting PXRD pattern shows quite strong texture. Also, since as-grown crystal aggregates were used, peaks of minority phases are present, most likely attributable to the flux. A combination of these effects forbids Rietveld analysis of the data. The poor quality of the data could be attributed to high ductility and ease of cleavage of the material.

Nonetheless, we can draw some conclusions from these measurements. PXRD patterns in Figure 4.4 show peaks in agreement with the literature for the $PtBi_2$ compound. As x in $Pt_{1-x}Rh_xBi_2$ increases, we don't see much qualitative change for nominal $x = 0.1$. For nominal $x = 0.5$ and $x = 0.75$, one can see prominent clusters of unresolved peaks at around $2\theta \approx 14.3^\circ$ and $2\theta \approx 19^\circ$, which correspond to the $RhBi_2$ structure. Since $RhBi_2$ is the main phase formed those experiments, we exclude them from

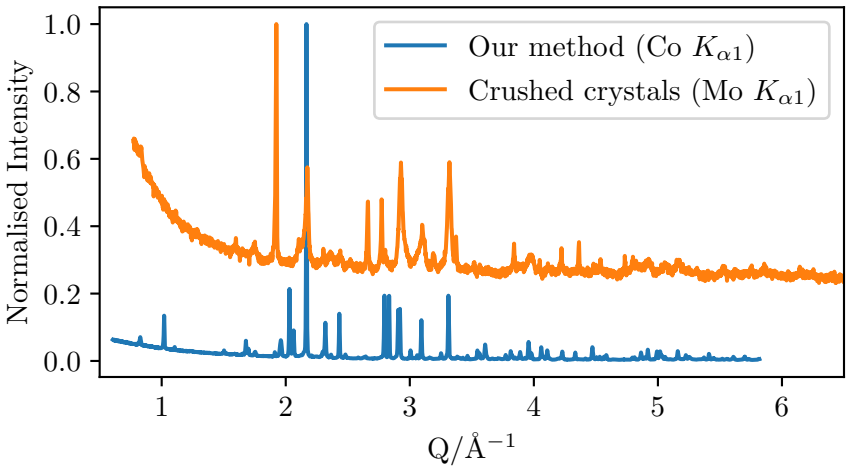

Figure 4.5: Comparison of PXRD patterns of $PtBi_2$, prepared using the conventional and with our newly-developed method for sample preparation. Notice lower FWHM, better peak resolution, lower texture, and better signal to background ratio for the preparation method presented in this thesis.

further consideration. In the case of $x = 0.3$, one can see weak features corresponding to the $PtBi_2$ phase, but the main phase formed in this compound doesn't seem to correspond to either $RhBi_2$ or to $PtBi_2$. This hints at some interesting chemistry in the $PtBi_2$–$RhBi_2$ system, which requires further studies of the phase relations between the end members. For more in-depth structural investigation, we focus on pure γ-$PtBi_2$ and nominal $x = 0.1$ sample due to hints of it being isostructural to $PtBi_2$.

To obtain PXRD patterns suitable for in-depth structural investigation via Rietveld refinement, the sample preparation was modified. Crystals were ground in a ball mill for 30 min, after which the powder was sealed in evacuated fused silica tube, and annealed in a box furnace for 72 h. The temperature was set as the "end" temperature of the corresponding single crystal growth, to guarantee recrystallization in the same polymorphic modification as the grown single crystals. To prevent polymorphic transitions taking place on cooling, at the end of the annealing period ampules with samples were quenched to ambient temperature water. To alleviate texture effects, the powder was first suspended in x-ray glue, after which a drop of the suspension was transferred to the holder with the help of a Pasteur pipette. This modification of the preparation method led to higher crystallinity of the PXRD sample and as a result, enhanced peak resolution and signal-to-background ratio. Such a method also significantly reduces the strong preferred orientation seen with the conventional PXRD sample preparation method. For clarity, comparison of PXRD patterns from conventional and our new method is presented in Figure 4.4.

The improved sample preparation method developed here allows for Rietveld refinement of the PXRD data. The results for the $PtBi_2$ re-annealed powder are presented in Figure 4.6. Diffraction data were analyzed in the framework of both structural models reported earlier: $P\bar{3}$ and $P31m$.[134,142] While in both cases refinement results in lattice parameters that agree well with the literature, refinement in the $P\bar{3}$ space group results in negative isotropic displacement parameters for the "Pt" and "Bi1" positions. Tables with structure factors, residual parameters and refined atomic coordinates are presented in the appendix B (Tab. B.1 and Tab. B.2). Residual parameters of the refinement corroborate the story: in case of the refinement in the $P31m$ model, the profile residual is $R_p = 5\%$, and weighted profile residual $R_{wp} = 7\%$. These residuals are significantly better than in case of the $P\bar{3}$ model fit: $R_p = 12\%$, $R_{wp} = 19\%$. Visual inspection, an essential method for assessing Rietveld refinement quality, reinforces the fact that $P31m$ model describes the data significantly better. For clarity, a zoom-in of the pattern is presented in the Appendix in Figure B.3. In case of the

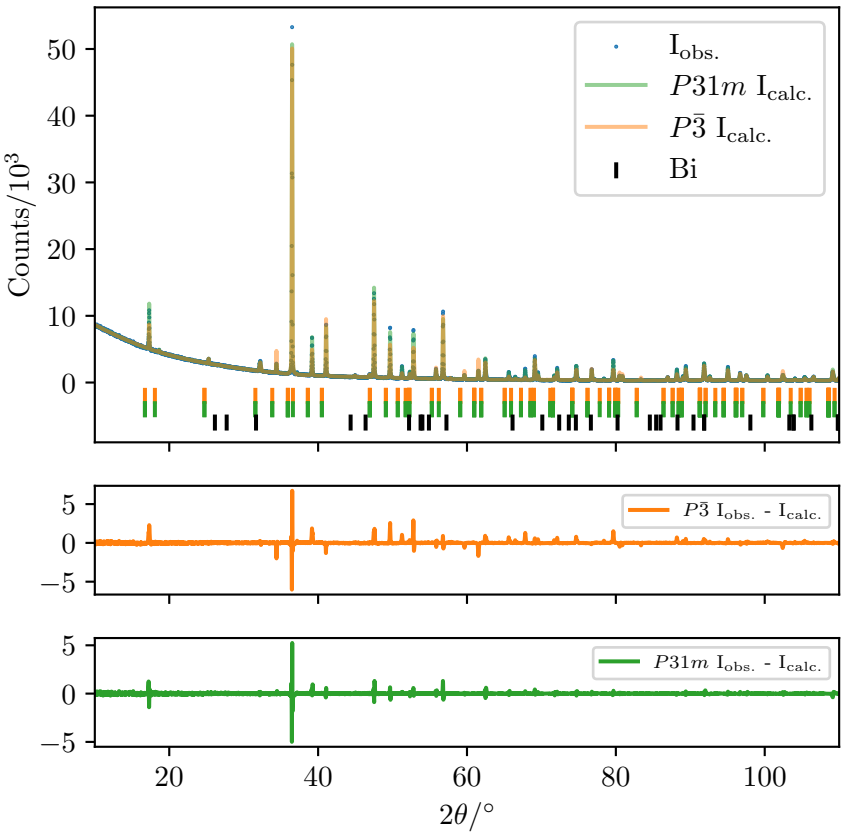

Figure 4.6: Rietveld refinement of $PtBi_2$ structure from PXRD: In the top panel the experimental data (markers) are superimposed with the Rietveld fit in the $P\bar{3}$ (orange) and $P31m$ (green) space groups. Peak positions (colorful ticks) and difference curves (two bottom panels) are plotted in corresponding colors. The theoretical peak positions expected for the Bi flux are marked as black ticks. Notice the intensity mismatch on difference curve for $P\bar{3}$ model, especially between 40–60° 2θ. For clarity, a zoom-in into high resolution part of the pattern is presented in the Appendix in Figure B.3

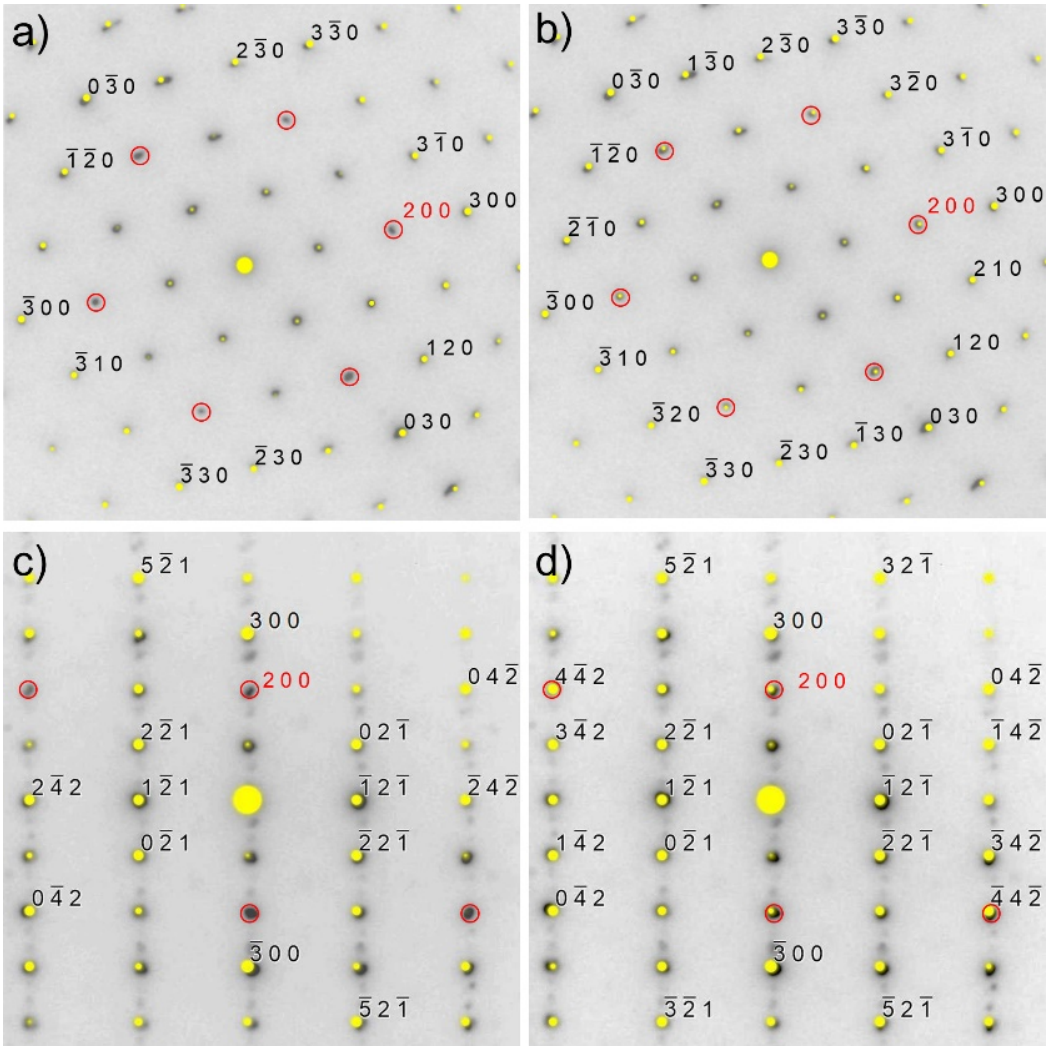

Figure 4.7: SAED data from $PtBi_2$ and $Pt_{1-x}Rh_xBi_2$. (a,b) SAED pattern of a representative $PtBi_2$ nanoflake oriented in the [001] zone axis overlaid with theoretical SAED patterns (yellow dots) using $P\bar{3}$ (a) and $P31m$ (b) space group models. (c,d) SAED pattern of a $Pt_{0.65}Rh_{0.35}Bi_2$ representative nanoflake oriented in the [012] zone axis, with the theoretical pattern overlay, in $P\bar{3}$ (c) and $P31m$ (d) space group models. The red circles in (a–d) indicate the 200 and symmetry-equivalent reflections which are virtually forbidden for $P\bar{3}$ symmetry (a,c), but clearly show up for $P31m$ (b,d)[118]

$P31m$ model, the difference curve is "cardiogram"-like. This is typical when imperfect peak profile description is present, together with noise, both of which are inherent to a diffraction experiment. On the contrary, the difference curve with respect to the $P\bar{3}$ model shows serious intensity mismatch for pretty much every diffraction peak. This tells that $P31m$ model provides better description of the atom positions in the unit cell than the $P\bar{3}$ case.

Due to the fact that the lattice in case of both models is the same, and symmetry of two structural descriptions is quite similar, one would ideally want to complement the findings above with single crystal diffraction. Unfortunately selecting a crystal for SC-XRD is rather difficult in this system.

The material's high ductility in combination with weak interlayer bonding eases the formation of stacking faults in the crystal, which smear out some of the reflections or leads to an intergrown-like diffraction picture (i.e. diffraction from several misoriented crystals). However, this complication can be circumvented by shrinking the analyzed volume to the point where macroscopic defects stop playing a serious role. One such "local" diffraction method is SAED, which we applied to $PtBi_2$ and $Pt_{0.65}Rh_{0.35}Bi_2$ crystals to seek further confirmation of the PXRD findings*. SAED was measured using FEI Tecnai G2 transmission electron microscope with a LaB_6 emmiter operated at 200 kV acceleration voltage. The nanoflakes were exfoliated from the bulk crystals using commercially available adhesive tape (Vivess). The flakes were separated from the tape in an ultrasonic bath while immersed in a 1:1 acetone-isopropanol mixture. Subsequently, the exfoliated flakes were transferred onto Cu-grids. To ensure the purity of the sample, elemental composition was checked using in-situ EDX. Theoretical kinematic electron diffraction patterns were simulated in the "SingleCrystal" software package, version 3.1.5 (CrystalMaker Software Ltd., UK).

The results of SAED are presented in Figure 4.7. SAED patterns were recorded in the [001] zone axis for $PtBi_2$ Figure 4.7 a, b and in the [012] zone axis for $Pt_{0.65}Rh_{0.35}Bi_2$ Figure 4.7 c, d. These SAED patterns are compared to the ones simulated with $Pt_{1-x}Rh_xBi_2$ models in space groups $P\bar{3}$ and $P31m$. As can be seen, the 200 and symmetrical equivalent reflections are present in both recorded patterns. Since these reflections are forbidden in the $P\bar{3}$ space group, i.e. their scattering factor is three orders of magnitude lower compared to computed diffraction from the $P31m$ structure model, SAED data strongly support the $P31m$ symmetry assignment for $PtBi_2$. For $Pt_{0.65}Rh_{0.35}Bi_2$ the local SAED result shows that at least some crystallites retain a $P31m$-related structure. However, because $Pt_{1-x}Rh_xBi_2$ samples are multiphase in PXRD, this observation on local scale cannot be interpreted as a proof of a homogeneous $Pt_{1-x}Rh_xBi_2$ solid solution.

To conclude, data from PXRD with Rietveld refinement together with TEM SAED data corroborate the $P31m$ structural model for the description of the γ-$PtBi_2$ structure, as suggested by Kaiser et al.[142] Additionally, this confirms that crystals obtained by Kaiser et al. via their low temperature route are of the γ-$PtBi_2$ phase. This bears significant consequences for further studies of physical properties, as it speaks for the predictions of Weyl semimetal states (lack of inversion center), instead of Dirac ones (centrosymmetric structure). While studies of physical properties of the materials are outside the scope of the present work, the bulk magnetic properties are screened in the following section.

4.5 Magnetization and Superconductivity

Since pure γ-$PtBi_2$ hosts superconductivity (as measured on crystals obtained in this work[118,125,127]), magnetization was measured for $PtBi_2$ and $Pt_{1-x}Rh_xBi_2$ crystals. $PtBi_2$, $Pt_{0.97}Rh_{0.03}Bi_2$ and $Pt_{0.65}Rh_{0.35}Bi_2$ exhibit regular diamagnetic behaviour, both in zero field and field-cooled measurements, the results of which are presented in the left panel of Figure 4.8. In a magnetic field of 0.5 T, all samples show no magnetic order down to 1.8 K, and a Curie-Weiss tail at low temperatures, probably due to paramagnetic impurities. To check for a possible superconducting response above the reported T_c of $PtBi_2$, the magnetization was also measured in low external field (2 mT), with results presented in the right panel of Figure 4.8. In the case of $Pt_{0.97}Rh_{0.03}Bi_2$, we do not see any signal down to 1.8 K, but in the case of $Pt_{0.65}Rh_{0.35}Bi_2$ we see well-pronounced superconducting-like downturn in the magnetization at ≈3 K. The zero-field cooled susceptibility monotonically decreases with temperature down to 1.8 K, and shows no signs of saturation. The volume shielding fraction at 1.8 K is rather low at ≈2%, which may reflect a broad transition, incomplete superconducting volume, or that superconducting phase is a minor phase of the sample. Therefore, this results demonstrates that the Pt-Rh-Bi system can host a superconducting-like response near 3 K. This is not, however, a definitive proof of a homogeneous T_c enhancement of $PtBi_2$ by Rh substitution.

*Selected-area electron diffraction data and analysis courtesy of Subakti Subakti, Dr. Daniel Wolf, and Dr. Axel Lubk.

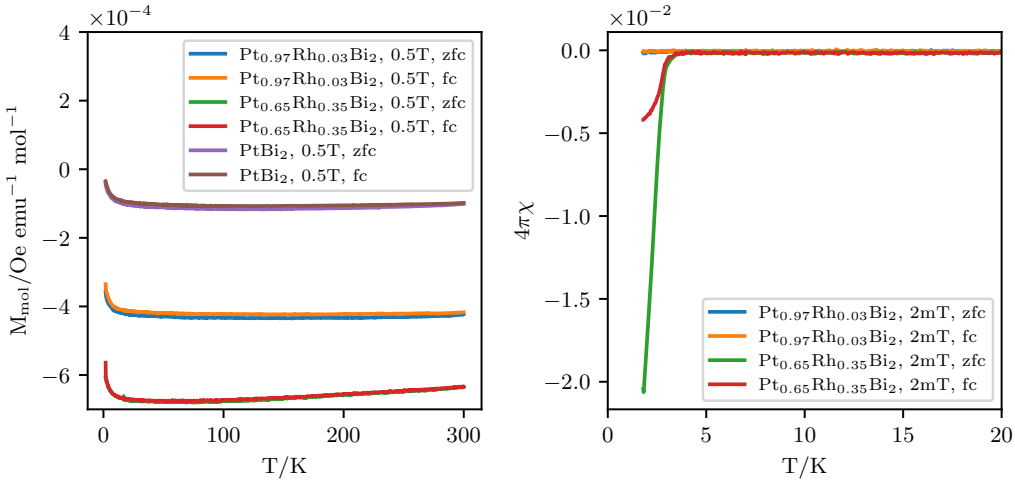

Figure 4.8: Temperature dependence of magnetization for $Pt_{1-x}Rh_xBi_2$ compounds. Left panel: molar magnetization in 0.5 T field in 1.8–300 K temperature range. Right panel: magnetic susceptibility in 1.8–20 K temperature range.

4.6 Summary and Outlook

In conclusion, large γ-$PtBi_2$ single crystals were grown successfully via the self-flux method. The present work optimized the growth protocol with a special attention to the rich polymorphism and temperature-induced structural phase transitions in the Pt–Bi system.

Chemical composition of the pristine $PtBi_2$ was found to be stoichiometric using EDX. A thorough reinvestigation of the γ-$PtBi_2$ crystal structure was performed by means of PXRD and SAED. A novel sample preparation method was developed for PXRD experiments to overcome the complications caused by the material's mechanical properties. This helped to alleviate strong preferred orientation and avoid broadening of the reflections. Rietveld refinement was carried out on the powder diffraction data. A combination of nonsensical displacement parameters, worse residuals and poor model fit overall was found in the case the of centrosymmetric $P\bar{3}$ model, and a reasonable fit resulted in the noncentrosymmetric $P31m$ model. These data resolve the existing confusion between the models. This conclusion is corroborated by local diffraction data from SAED.

The clarification of the lattice symmetry has far-reaching implications for further studies of this material's electronic properties. The confirmed model corresponds to a band structure with type-I Weyl states in the vicinity of the Fermi energy, which determine the exotic conducting properties of this material. The refuted structure model also happens to be that accorded with a less attractive electronic structure, with trivial metallic states at the Fermi level and surface Dirac fermions stemming from a topological band inversion at -2 eV. Before this work, the latter structural model was, however, the prevalent description in the published literature. Furthermore, the non-centrosymmetric crystals obtained in the course of this work show signs of topological superconductivity, making γ-$PtBi_2$ a strong candidate for breakthrough quantum behavior.[127–130]

We also conducted partially successful attempts of elemental substitution at the Pt site in order to study the structural evolution. Nickel incorporates into the crystals, but quite unevenly as confirmed by EDX spectroscopy, and likely does not form a typical solid solution with $PtBi_2$. Rhodium does incorporate into the crystals according to EDX, but the structural interpretation is more complex. The nominal $x = 0.1$ product is closest to $PtBi_2$ in PXRD, and therefore was used in for Rietveld analysis. At higher nominal Rh contents the products become multiphase. In particular, the nominal $x = 0.3$ product contains weak $PtBi_2$-like features, but its main diffraction features do not correspond

cleanly to either $PtBi_2$ or $RhBi_2$. SAED on a selected $Pt_{0.65}Rh_{0.35}Bi_2$ flake nevertheless suggests that $P31m$-related crystallites can be present in this composition range. Preliminary magnetization screening further shows a superconducting-like diamagnetic downturn near 3 K in the nominal $x = 0.3$ sample, although the low shielding fraction and imcomplete bulk phase assignment prevent this feature from being assigned unambiguously to a homogeneous $Pt_{1-x}Rh_xBi_2$ phase. This findings indicate that the Pt-Rh-Bi system is a promising target for further work on superconducting properties, but they do not confirm an extended $Pt_{1-x}Rh_xBi_2$ solid solution at this stage. Since $PtBi_2$ and $RhBi_2$ represent different topological material classes, better-controlled samples in this compositional region could also be interesting for future studies of topological transitions and superconducting behaviour.

Chapter 5

$TaTMTe_4$: Ordered and Disordered Structures

This chapter is based upon the publication: Shipunov, G. et al. Layered van Der Waals Topological Metals of $TaTMTe_4$ (TM = Ir, Rh, Ru) Family. *The Journal of Physical Chemistry Letters* **2021**, *12*, 6730–6735[147]

5.1 Introduction

We now turn from $PtBi_2$ to a materials system closely related to the transition metal dichalcogenide (TMDC) WTe_2. Ternary transition-metal tellurides MM^*Te_4 (M=Nb, Ta; M* = Rh, Ir, Ru, Os) were discovered by Mar et al.[19,148] in the early 1990s. The crystal structures of $TaIrTe_4$ and $NbIrTe_4$ are closely related to orthorhombic WTe_2, which is nowadays among the most studied TMDC quantum materials.[149] In contrast to WTe_2 and other binary TMDC materials, interest in the ternary derivatives was rekindled only in recent years and currently is on a steep rise. Published research has so far focused on the most well-characterized member $TaIrTe_4$: it has the band structure of a type-II Weyl semimetal[150–152] and demonstrates a nonlinear Hall effect with temperature-induced sign change.[153] Thanks to its layered nature, the compound is easy to cleave, facilitating studies of thickness dependent properties: booth mono- and bilayer $TaIrTe_4$ demonstrates the quantum Hall effect,[154,155] as well as signatures of surface superconductivity at critical temperatures up to 1.54 K.[156] Another member of this ternary telluride family, $NbIrTe_4$, has been proposed to host type-II Weyl fermions, effects of which have likely already been observed experimentally in charge transport measurements,[157] and this system also exhibits non-saturating magnetoresistance.[158] The exotic electronic properties of these ternary tellurides make them of interest for technological applications. This potential has been illustrated recently by the observation of bi-stable, resistive metal-insulator switching in point contact measurements at room temperature.[70]

The crystal structures of $TaIrTe_4$ and $NbIrTe_4$[19,148] have been solved in the orthorhombic space group $Pmn2_1$ on the basis of data from single-crystal X-ray diffraction experiments. These structures can be described as stacks of van der Waals layers along the c direction, as shown in Figure 5.1. Each layer consists of edge-sharing, distorted octahedra centered around a transition-metal cation, M or M*. The distortion in the transition-metal coordination environment arises from the underlying chemical bonding, making it dependent on the chemical composition. The ideal octahedral coordination becomes distorted because the transition elements shift towards each other to engage in metal-metal bonding, forming zigzag chains along the a direction. Due to its more covalent nature compared to sulfur or selenium and its low electronegativity, tellurium does not form purely ionic M–Te bonds. This often results in tellurides having distinct structures compared to sulfides and selenides.

In a hypothetical ionic picture, formal charges would be assigned as $Ta^{5+}Ir^{3+}(Te^{2-})_4$. However, charge transfer from Te to Ta and Ir reduces formal charge of the Te atoms and induces attractive Te−Te bonding interactions, and observed as shortening of the Te−Te distances well below the sum of the respective van der Waals radii. Simultaneously, the transition-metal cations M and M* acquire extra electrons (more metallic character) and cluster into zig-zag chains. This electronic situation is reflected in the oxidation state formula $Ta^{4+}Ir^{3+}(Te^{-1.75})_4$. The presence of such an electronic reservoir of metal-metal bonding suggests that this structure type has a broad variability: it can

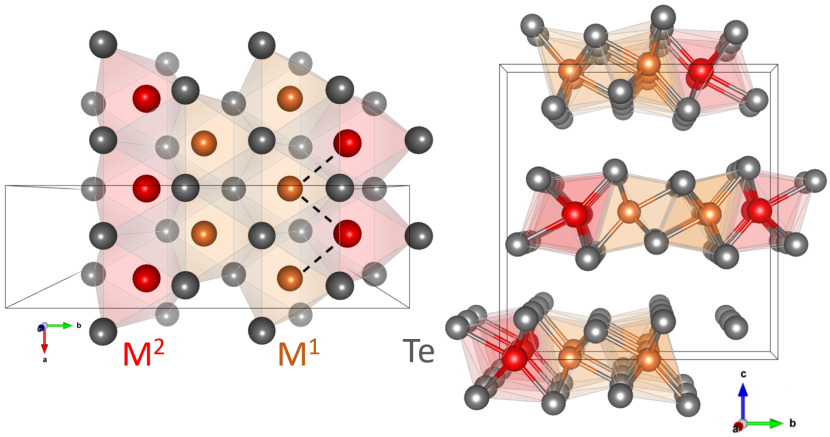

Figure 5.1: Schematics of the WTe_2-like orthorhombic structures. For WTe_2, M^1=M^2=W; for $TaTMTe_4$, M^1=TM, M^2=Ta. Dashed lines are guide for eyes outlining the zigzag chains running along a. The unit cell is outlined for $TaTMTe_4$.

accommodate various combinations of transition metals and resolve electronic imbalances through structural distortions, either in the Te sublattice by forming Te−Te bonds or in the metal sublattice by forming chains.

The WTe_2 crystal structure is another example of this flexibility: the transition metal sites are equivalent, M = M* = W, and they form zigzag chains along the a axis, with W−W distance of approximately 2.85 Å. The lattice is derived from that of $TaIrTe_4$ by halving the b direction due to the equivalency of the transition metals. This results in van der Waals lattices with similar atomic connectivity and crystal symmetry, underlying certain similarities in their electronic structures and unconventional electronic properties.

This structural flexibility together with unconventional physical properties fuel stronger interest in the less-studied MM^*Te_4 representatives. Whereas reliable growth protocols are available for $TaIrTe_4$ and $NbIrTe_4$,[19,148] the other members that have been identified such as $TaRuTe_4$, $NbOsTe_4$, $TaOsTe_4$, and $TaRhTe_4$ were obtained only as minor fractions in the mixtures of binary tellurides. In this light, the structural description of these new representatives in the MM^*Te family is inconclusive and requires an in-depth reinvestigation. In their original structure report, Mar et al.[19] assumed that all these members are isostructural to $TaIrTe_4$. On a special note they mention that $TaRuTe_4$ diffraction data has systematic absences of diffraction peaks, which might be indicative of metal site disorder, but nonetheless Mar et al. report it as isostructural to $TaIrTe_4$. The structural data deposited in major crystallographic databases (e.g. ICSD entry No. 656452) also describe the $TaRuTe_4$ structure as an isostructural analog of $TaIrTe_4$, without any disorder. Since Ru and Os have one d-electron more than Rh and Ir, their electronic situation is more suitably described by the formulation $Ta^{5+}Ru^{3+}(Te^{-2})_4$ with decreased charge transfer from Te to the transition metals. In turn, this may impact the crystal structure significantly.

Emerging interest in the ternary tellurides as quantum materials warrants expansion of the availability of those compounds, in the first order, by developing crystal-growth protocols for $TaRhTe_4$ and the Ta−Ru−Te phase, originally reported as $TaRuTe_4$. Given the importance of accurate structural models for investigating material properties, it is crucial to examine any potential disorder in these crystals. Another point of interest is the pursuit of solid solutions among the large number of compounds with identical or related crystal structures. The similarity in the crystal structure and elemental chemistry suggests the feasibility of such solutions. These solid solutions may exhibit a smooth variation in material composition and structural parameters, and consequently, in physical properties. Identifying miscibility gaps or abrupt changes in lattice symmetry, which may indicate either tuning or abrupt changes in electronic properties, is also worth exploring.

5.2 Synthesis

The first reported synthetic technique for $TaIrTe_4$[19,148] employed a high-temperature reaction with a double excess of tellurium. Later, an optimized route to $TaIrTe_4$ single crystals was developed by Khim et al.,[151] using the self-flux method with molten tellurium which can be centrifuged away. In this work, this self-flux method was adopted to several other $TaTMTe_4$ compounds as well as to the substitution series. The cooling rate was reduced to minimize oversaturation, and in case of quaternary compounds, the centrifuging temperature was increased in an attempt to reduce the amount of secondary phases. Note, phase diagrams of the respective ternary and quaternary systems are not known, so the synthetic parameters had to be selected through a trial-and-error process. Following this route large single crystals of $Ta_{1.25}Ru_{0.75}Te_4$, $TaRhTe_4$ and $TaIr_{1-x}Rh_xTe_4$ were obtained for the first time. Their characterization established that the ruthenium analog in fact has the off-stoichiometric $Ta_{1.25}Ru_{0.75}Te_4$ composition.

Single crystals of $TaIrTe_4$, $TaRhTe_4$, and $Ta_{1.25}Ru_{0.75}Te_4$ were grown via the self-flux method. Powders of Ta (Alfa Aesar, powder 325 mesh, 99.97%), transition metal, TM=Ir (Alfa Aesar, powder 325 mesh, 99.9%), Rh (Evochem, powder, 99.95%), Ru (MaTecK, powder, $< 60\mu$m, 99.9%) correspondingly, and Te (Alfa Aesar, powder 18 mesh, 99.999%) were mixed in the Ta:TM:Te=1:1:20 molar ratio and thoroughly ground by hand in an agate mortar. Afterwards the reaction mixture was loaded into a Canfield crucible set,[110] which in turn was placed in an evacuated fused quartz ampule. The mixture was heated up to 970°C at 100°C/h, kept at this temperature for 24 h, and subsequently slowly cooled at the rate of 1.5°C/h to the final temperature of 600°C. Further, the crucible was taken out of the hot furnace, turned over and instantly put into a centrifuge which facilitated the flux removal. The resulting crystals were mechanically separated from each other, and from the crystals of minority binary phases, mostly cubic, binary transition-metal tellurides. The latter formed as more isometric, prismatic-like crystals and thus could be easily identified and removed. After this, the small amounts of the remaining flux were mechanically cleaved off from the crystal surfaces.

The $TaIr_{1-x}Rh_xTe_4$ substitution series was synthesized by mixing the elemental powders in the molar ratios Ta:$Ir_{1-x}Rh_x$:Te=1:1:20 for $x = 0.1$, 0.3, 0.7 and 0.9, similar to the preparation procedure for the ternary compounds described above. The mixtures were heated up to 1000°C, held at this temperature for 24 h, and then cooled over the course of 133 h to 700°C, after which the reaction mixture was centrifuged in the aforementioned manner. Needle-like crystals for further studies were manually separated from the ingots, secondary phases and remaining flux could easily be easily cleaved off.

Polycrystalline samples of $TaRhTe_4$, $TaRuTe_4$, and $Ta_{1.25}Ru_{0.75}Te_4$ were synthesized by a direct solid-state reaction. Powders of Ta, Te, and the corresponding transition metal were taken in the stoichiometric amounts for a total charge of ca. 300 mg per experiment. Powders were thoroughly homogenized in an agate mortar and sealed in an evacuated quartz ampule. The mixture was heated up to 700°C at 100°C/h, held at the temperature for 48 h, and then quenched in air.

5.3 Composition and Morphology

As-grown crystals of $TaIrTe_4$, $TaRhTe_4$, $TaIr_{1-x}Rh_xTe_4$, and $Ta_{1.25}Ru_{0.75}Te_4$ compounds were acquired as flat, silvery needles. Optical as well as SEM images of typical crystals are presented in Figure 5.2. The cross-section of $TaIrTe_4$ and $Ta_{1.25}Ru_{0.75}Te_4$ needles is almost squared. $TaRhTe_4$ needles grown in the shape of flattened thin stripes. Some $TaRhTe_4$ crystals have almost platelet-like appearance, shaped like a very wide rectangle.

As-grown crystals of all $TaTMTe_4$ compounds are extremely ductile and easily cleavable in two perpendicular directions along the long axis of the crystal. Upon any handling the crystals bend and twist effortlessly, and also split into hair-like soft needles (e.g. see Figure 5.2c). This mechanical behavior arises because of the quasi one dimensional crystal structure with strongly bound metal-metal zigzag chains. Mechanically the crystals resemble fine aluminum foil. This behavior also leads to destruction of long-range order actively prohibiting SC-XRD studies.

SEM images of the ternary compounds (Figure 5.2 (b)) show even, homogeneous surfaces both in Z and topography contrast, demonstrating absence of macroscopic element concentration gradients.

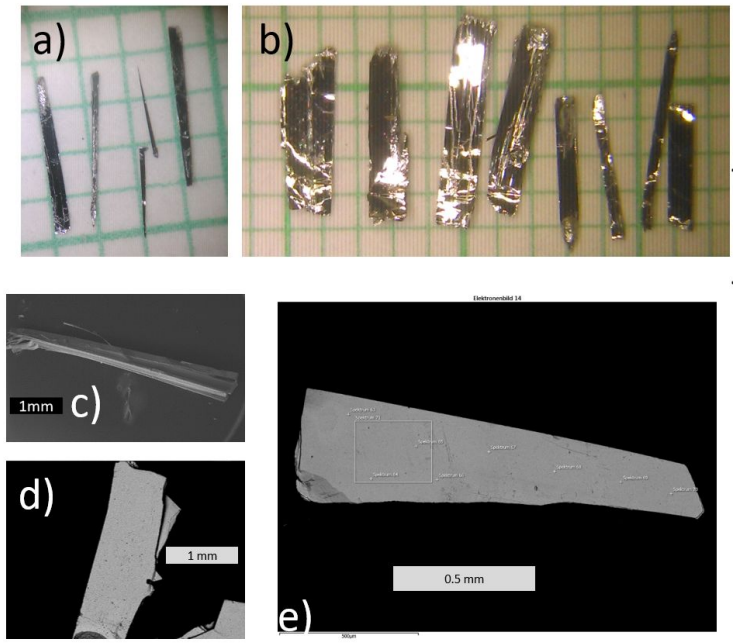

Figure 5.2: (a,b): images of as-grown $Ta_{1.26(2)}Ru_{0.75(2)}Te_{4.000(8)}$ (a) and $TaRhTe_4$ (b) on a millimeter scale. Notice the difference in habit. (c–e): SEM images of $TaRhTe_4$ (c) and $Ta_{1.26(2)}Ru_{0.75(2)}Te_{4.000(8)}$ (d,e). In (c), the layered morphology of the crystals is clearly visible.[147]

Table 5.1: comparison of nominal and measured composition determined using EDX for $TaIr_{1-x}Rh_xTe_4$ crystals

Ir:Rh, nominal	EDX composition
$Ir_{0.9}Rh_{0.1}$	$TaIr_{0.96}Rh_{0.04}Te_4$
$Ir_{0.7}Rh_{0.3}$	$TaIr_{0.82}Rh_{0.14}Te_4$
$Ir_{0.3}Rh_{0.7}$	$TaIr_{0.22}Rh_{0.78}Te_4$
$Ir_{0.2}Rh_{0.8}$	$TaIr_{0.08}Rh_{0.92}Te_4$

The surface of the crystals appears smooth with some steps, which is in line with the layered crystal structure.

Composition of the crystals was studied by means of EDX. For $TaIrTe_4$ and $TaRhTe_4$ spectroscopy shows stoichiometric composition. Surprisingly, in case of the ruthenium compound, EDX composition is $Ta_{1.26(2)}Ru_{0.75(2)}Te_{4.000(8)}$, i.e. the Ta to Ru ratio is drastically different from nominal, and from the corresponding $TaIrTe_4$ and $TaRhTe_4$ crystals. Assuming that connectivity of the crystal structure is the same as in phase prototype $TaIrTe_4$, i.e. the structural motifs are the same, this off-stoichiometry must result either in disorder, or in alteration of the structure. This is in line with a related discrepancy reported by Mar et al.,[19] and requires revisiting of the $Ta_{1.25}Ru_{0.75}Te_4$ crystal structure.

SEM and EDX analysis was also performed for the $TaIr_{1-x}Rh_xTe_4$ series of compounds. As in case of the ternary compounds, visual inspection of the BSE and SE images show flat uniform surfaces, indicating absence of the macroscopic concentration gradients. The crystal habit is similar to the "parent" compound. Composition for $TaIr_{1-x}Rh_xTe_4$ series was studied via EDX spectroscopy, the

results of which, together with corresponding ratios of transition metals in reaction mixture are presented in Tab. 5.1. The data clearly show incorporation of both transition metals into the crystal. These factors provide a strong indication of solid solution formation between Ir and Rh compounds, but further structural and phase-relation studies are needed. Interestingly, the composition is shifted in each case towards the element with higher concentration. Further analysis of this concentration behavior should include EDX spectroscopy from flat polished samples, employing standards so as to improve the quantitative analysis, and an in-depth investigation of the phase relations in the quaternary system. However, the phase diagrams have not yet been reported, even for the ternary end members.

5.4 Structure

Product purity and preliminary assessment of the structure for $TaTMTe_4$ was done via PXRD experiments. However, this process was seriously hindered by the high ductility and spontaneous cleaving of the crystals. This is a typical picture in case of such layered compounds, and this experience is similar to the one described in the Section 4.4. For the $TaTMTe_4$ compound family, SC-XRD studies proved to be equally challenging, since picking a crystal for the experiment often introduces mechanical damage. This damage disrupts the long-range order required in a single crystal diffraction experiment.

In case of the $TaTMTe_4$, in addition to weak van der Waals bonding between the layers there is also a "weak" cleavage plane perpendicular to the van der Waals gap, between the zigzag chains. Macroscopically this results in crystals cleaving along two perpendicular planes, therefore breaking into thin wires. These wires are extremely easily bent, due to the high ductility of the material. Thus, the conventional sample preparation approach for PXRD — manual grinding of the crystals — introduces huge amount of defects, which then results in very broad, low-intensity reflections. The example of peak profiles obtained in this way is presented in the Appendix, in Figure B.2. While one can recognize the fingerprint of the ternary phase, reliable extraction of the lattice or atomic positions via full profile analysis is deemed unfeasible. Furthermore, the peak intensity is also rather low due to the high absorbance of the materials. This effect is especially noticeable in the transmission geometry of the PXRD experiment, a geometry that helps to alleviate the deleterious effects of a strong preferred orientation (inherent in layered materials), and allows for collection of accurate intensities in the whole 2θ angle range.

For obtaining powder diffraction data usable for full-profile refinement, sample preparation procedure was modified to minimize grinding of single crystals. While this modification resulted in suboptimal, non-uniform particle size distribution, known as "stones in the sand", it nonetheless allowed for acquisition of usable diffraction patterns for $TaIrTe_4$ and $TaRhTe_4$, as presented in Figure 5.3. In both cases, model diffraction profiles are able to fit the data well, with reasonable residual parameters for this data quality. Refinement tables and refined atomic positions are presented in Appendix B. Atomic displacement parameters could not be refined due to low intensity of the signal and the peak broadening, with grinding-induced disorder being the most probable reason.

The lattice parameters are in agreement with those reported previously. When moving from $TaIrTe_4$ to $TaRhTe_4$, the a and c lattice parameters shrink somewhat, and b significantly increases ($\Delta a \approx -0.03$ Å; $\Delta b \approx +0.12$ Å; $\Delta c \approx -0.03$ Å). This effect might be the result of changing Ir^{3+} (0.68 Å) to the smaller Rh^{3+} (0.66 Å), and, as a consequence, the tighter, more extended zigzag chains in the structure. Indeed, in case of $TaRhTe_4$ one of the alternating angles in the chain is bigger ($\phi \approx 71°$ vs 76°) with comparable bond lengths, which leads to an elongation of the chain. Furthermore, contraction in c might suggest stronger electron density transfer from Te towards the transition metal, thereby strengthening the direct Te–Te interactions. Indeed, the shortest Te–Te interlayer distance shrinks from ≈ 3.7 Å in case of $TaIrTe_4$ to 3.3 Å in case of $TaRhTe_4$. Potentially, this change could result in more three-dimensional character, and could alter its electronic properties compared to $TaIrTe_4$.

The powder sample from solid state reaction with the starting $TaRuTe_4$ composition was clearly multi-phase. Together with the fact that EDX data, extracted from single crystals obtained in

this work, cleary shows $Ta_{1.25}Ru_{0.75}Te_4$ composition, this calls into question the existence of a pure, stoichiometric $TaRuTe_4$ phase. Due to the discussed complications of PXRD phase analysis in these ternary systems, final conclusions about the possible homogeneity range of this ternary phase and its structural and compositional variability are considered out of the scope of this thesis. Future studies should begin with the optimization of the sample preparation and ideally also include clarification of the phase relations in this system.

The issues with poor diffraction data quality are even more severe for the $TaIr_{1-x}Rh_xTe_4$ series of compounds. Any—even slight—grinding of the obtained single crystals results in extremely broad diffraction peaks, while their intensity is rather low due to high absorbance of the material. Powdered samples also require grinding because as-grown grains are too large for optimal powder-data collection, especially when measurements on these highly absorbing samples are performed in the transmission geometry. Additional complications arise from the admixtures of well-crystallized binary phases (e.g. $IrTe_2$, see Appendix B.2). The majority of these secondary phases crystallize in high-symmetry crystal systems (e.g. cubic for $IrTe_2$) and are, therefore, mechanically quite hard and brittle. As a result, they pulverise very well upon grinding, and contribute very sharp, high-intensity peaks in the diffraction patterns, on top of the broadened, low-intensity reflections of the target phase. This poses yet another challenge for the phase analysis of the obtained phase mixtures.

Based on the lessons learned in Section 4.4, structural analysis of $TaIrTe_4$, $TaRhTe_4$, and $Ta_{1.25}Ru_{0.75}Te_4$ was carried out using the SAED method. Optimizing the PXRD sample preparation would be considerably time-consuming and was therefore deemed impractical. At this point, we refrained from SAED studies of the $TaIr_{1-x}Rh_xTe_4$ series because the crystal growth protocols for this series need to be optimized first, so as to achieve reproducible and accurate elemental compositions.

Samples for SAED were prepared by mechanically exfoliating single crystals using commercially available adhesive tape (eco, tesa).* The conventional approach was adapted in the following way to deal with high ductility of the crystals and their strong propensity to bending, cleaving, and forming defects. The exfoliated $TaTMTe_4$ crystals were separated from the tape by immersion in 10 mL of acetone and isopropanol (1:1) solution in a 12 mL glass sample vial. Sonication (frequency ≈ 35 kHz) was employed to assist the separation of flakes from the tape surface for 2 h (8×15 minutes sonication, with 5 minute breaks between the 15 minute sessions). The resulting micrometer-sized $TaTMTe_4$ flakes were then transferred to lacey-carbon copper TEM grids using a standard pipette. To ensure the cleanliness of the flakes, the elemental composition of every flake was controlled using in-situ TEM-EDX, before collection of the SAED pattern.

The SAED patterns were collected using FEI Tecnai F20 transmission electron microscope (TEM), equipped with a LaB_6 emitter operated at 200 kV acceleration voltage. The images of the reciprocal $(010)^*$ zone (along the [101] zone axis) allow visualization of the lattice differences in various $TaTMTe_4$ structures along the b^*-direction. The experimental data and simulated patterns for the $Pmn2_1$ space group agree nicely in the case of $TaIrTe_4$ (Figure 5.4a) and $TaRhTe_4$ (Figure 5.4b). This result is in line with our aforementioned Rietveld refinements of the PXRD data, as well as the results of structural investigations reported previously by Mar et al.[19] Remarkably, the observed $Ta_{1.25}Ru_{0.75}Te_4$ diffraction pattern does not match up with the theoretical structural model based on the earlier published data. Namely, every second reflection along the b^* ($k = 2n + 1$, $n-$ integer) is systematically absent, hinting at the halving of the b lattice parameter in comparison with the regular $TaIrTe_4$-type structure (Figure 5.4c). In other words, the SAED $(010)^*$ pattern of $Ta_{1.25}Ru_{0.75}Te_4$ accords more with the WTe_2-type structure (Figure 5.4d). The observed reduction of the b unit cell parameter may be related to symmetry enhansment caused by randomized antisite disorder between Ta and Ru. In this scenario, the two transition metal crystallographic positions become partly of fully averaged, making the local diffraction pattern of $Ta_{1.25}Ru_{0.75}Te_4$ closer to that expected for a WTe_2-type structure. Based on SAED results, the phase with composition $Ta_{1.25}Ru_{0.75}Te_4$ appears to adopt this WTe_2-like average lattice. This interpretation may have important implications for the electronic band structure and transport properties, but it requires confirmation by full structural refinement. Our observation nevertheless provides a plausible explanation for the systematic absences

*Selected-area electron diffraction experiment courtesy of Subakti Subakti, Dr. Daniel Wolf, and Prof. Axel Lubk.

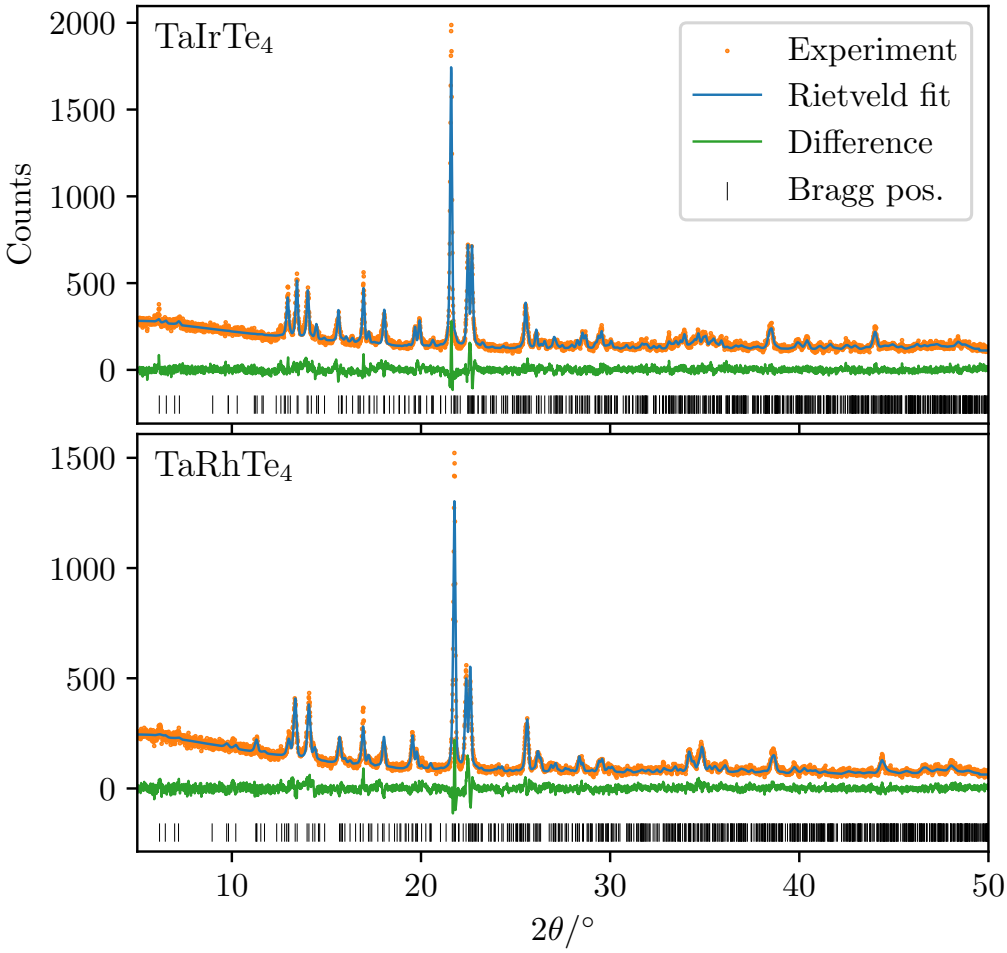

Figure 5.3: Rietveld refinement of $TaIrTe_4$ (top panel) and $TaRhTe_4$ (bottom panel).[147]

of diffraction peaks previously observed by Mar et al..[19]

It remains unclear whether the $Ta_{1.25}Ru_{0.75}Te_4$ compound exists solely with 1.25:0.75 Ta:Ru stoichiometry, or if different compositions for material exist. The composition may arise from the electronic configuration. Mar et al.[19] provide an argument by considering WTe_2, $TaIrTe_4$ and $NbIrTe_4$ compounds. In this series Mar et al. experimentally demonstrates that metal-metal bond distance increase, and Te−Te bond distance decrease, resulting in more tightly bound layers. In their work they go on to explain that going from W to Ir extra electron has to occupy an antibonding M−M level, resulting in weakening M−M bond, elucidating bond lengthening. In case of Nb *d* levels are close in energy to *p* orbitals of Te, resulting in further redistribution of charge, which results in strengthening of Te−Te interactions and formation of weak Te−Te bonds. We apply the same argument to the Rh and Ru compound. As number of *d* electrons decreases when moving from Rh to Ru, fewer electrons are on the antibonding orbitals, enhancing metal-metal bonding in the zigzag chains. Consequently, the extent of electron transfer from the Te to the transition metal decreases, and Te−Te bonding ceases. Thus, interlayer Te–Te distances widen, favoring a truly two-dimensional structure like WTe_2. Furthermore, as mentioned in the introduction to this chapter, Mar et al. stipulated that the formal charge on the Ta atom increases from +4 to +5 as we move from $Ta^{4+}Rh^{3+}(Te^{-1.75})_4$ with

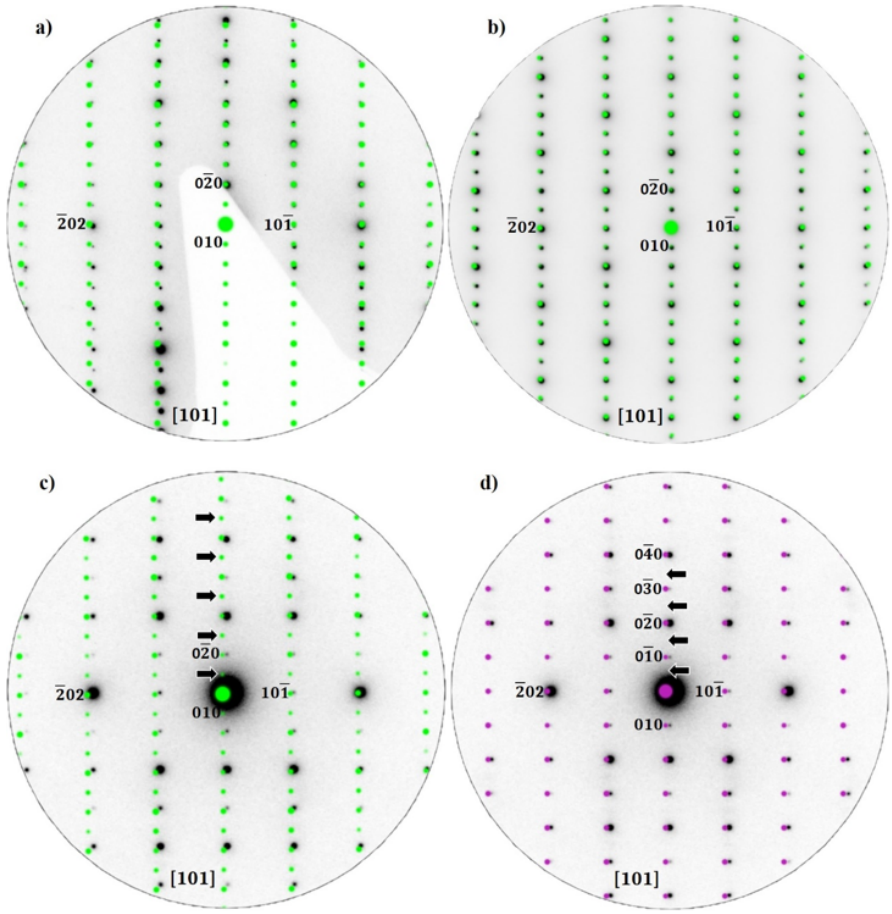

Figure 5.4: SAED on $TaIrTe_4$, $TaRhTe_4$, and $Ta_{1.25}Ru_{0.75}Te_4$. (a, b): SAED patterns of representative $TaIrTe_4$ and $TaRhTe_4$ nanoflakes oriented along [101] zone axis, overlaid with theoretical SAED patterns (green dots) using a $Pmn2_1$ space group model based on data refinement of PXRD obtained in this work. (c, d): SAED pattern of a representative $Ta_{1.25}Ru_{0.75}Te_4$ nanoflake oriented along [101] zone axis overlaid with theoretical SAED patterns using $Pmn2_1$ structure derived from $TaIrTe_4$ (c), and a $Pmn2_1$ structure derived from WTe_2 (unit cell is halved along b compared to $TaIrTe_4$, d). Note that model overlay is intentionally slightly shifted horizontally for easier comparison with the SAED data. The black arrows in (c) and (d) mark the (in) ability of the two models to fit the absence of $k = 2n + 1$ peaks in the pattern for $Ta_{1.25}Ru_{0.75}Te_4$.[147]

Te–Te bonding to $Ta^{5+}Ru^{3+}(Te^{-2})_4$ without Te–Te bonding. The higher charge of Ta^{5+} contracts its atomic radius to 0.64 Å, in contrast to 0.68 Å in Ta^{4+}.[159] Thus, the uneven Ta:Ru ratio in the stable $Ta_{1.25}Ru_{0.75}Te_4$ lattice could result from geometrical balancing the smaller, higher-charged Ta^{5+} cations with the larger, lower-charged Ru^{3+} cations. Intriguingly, an electron-neutral formulation without Te–Te bonding can be also achieved with the experimentally found non-integer stoichiometric coefficients if one assumes Ta^{4+} and Ru^{4+} oxidation states, i.e. $(Ta^{4+})_{1.25}(Ru^{4+})_{0.75}(Te^{-2})_4$. If the latter explanation is correct, $Ta_{1.25}Ru_{0.75}Te_4$ would be isoelectronic and isostructural to $W^{4+}Te_2$. The proposed relation between $Ta_{1.25}Ru_{0.75}Te_4$ and WTe_2 is an attractive hypothesis for further studies, which first requires full structural and spectroscopic confirmation.

5.5 Summary and Outlook

In this chapter, single crystals of the family of ternary transition-metal tellurides $TaTMTe_4$ were obtained. These are emerging as promising quantum materials with attractive (magneto)transport properties. Crystal-growth protocols were optimized and, for the first time, sizeable crystals of $TaRhTe_4$, $Ta_{1.25}Ru_{0.75}Te_4$, and $TaIr_{1-x}Rh_xTe_4$ with $x = 0.04, 0.18, 0.78$ and 0.92 were obtained, with compositon confirmed via EDX spectroscopy.

Current protocols already yield large crystals of $TaIrTe_4$, $Ta_{1.25}Ru_{0.75}Te_4$, and $TaRhTe_4$, which can be mechanically extracted from as grown ingots. We observed more admixtures in experiments targeting $TaIr_{1-x}Rh_xTe_4$, indicating that further optimization of the growth conditions is necessary to eliminate these unwanted phases. Nevertheless, available $TaIr_{1-x}Rh_xTe_4$ crystals are sufficiently large for first characterization of their physical properties. In order to improve the crystal yield and our understanding of the phase formation and variability, an in-depth study of the yet unknown phase relations in these ternary and quaternary systems is required.

In terms of chemical composition and crystal structure, we confirmed that $TaIrTe_4$ and $TaRhTe_4$ crystallize in the previously reported orthorhombic lattice (sp. gr. $Pmn2_1$). Overcoming severe experimental challenges, structure of those two phases was confirmed via the Rietveld method. Previously published determinations were based on rotation and Weissenberg photographic data,[19,148] which are less sensitive to superstructures and lattice distortions than contemporary x-ray equipment. Analysis of the lattice parameters in the present work suggests that the $TaRhTe_4$ lattice may have a less pronounced two-dimensional character than $TaIrTe_4$. An impact of this on the electronic band structure needs to be evaluated in future studies.

Furthermore, the first indications were presented that show existence of a continuous $TaIr_{1-x}Rh_xTe_4$ solid solution, with members both on the Ir- and Rh-rich sides as verified by EDX spectroscopy. Future studies should investigate the crystal and electronic structure evolution upon Rh doping into $TaIrTe_4$, as the protocol for crystal growth is now available. This substitution series will help the field explore how the two-dimensional character of this lattice develops, given that Ir orbitals lie higher in energy and do not contribute to the Fermi level, whereas Rh orbitals lie lower in energy and potentially contribute more to the three-dimensional Weyl-semimetal states at the Fermi level.

In this chapter, the first reliable compositional and structural assessment of tantalum-ruthenium telluride is also provided. Unlike what has been previously suggested, this compound has a non-stoichiometric, Ta-rich $Ta_{1.25}Ru_{0.75}Te_4$ composition and crystallizes in a different lattice than the other family members. SAED data presented in this work shows systematic absences consistent with a halved b lattice parameter compared to the ordered $TaIrTe_4$-type structure. This observation suggests that $Ta_{1.25}Ru_{0.75}Te_4$ may adopt a WTe_2-like average structure. A plausible explanation is partial or uniform Ta/Ru disorder over the two transition metal positions, which would reduce the distinction between them and make the diffraction pattern closer to that of WTe_2-type structure. This preliminary assesment makes further structural studies of the compound attractive for further research, since a complete structural model would require full structure refinement. Two possible electronic configurations for Ta and Ru are briefly discussed — heterovalent and isovalent. Future spectroscopic and full-structure diffraction studies should help determine which configuration is more accurate. The isovalent configuration, $(Ta^{4+})_{1.25}(Ru^{4+})_{0.75}(Te^{-2})_4$, is particularly promising for

technological advances, as it renders $Ta_{1.25}Ru_{0.75}Te_4$ not only isostructural but also isoelectronic to the renowned $W^{4+}Te_2$ quantum material.

In these investigations of the $TaTMTe_4$ family of compounds, extensive efforts to map out phase relations and optimize synthetic protocols, as well as crystal-structure evaluation of powder samples by PXRD, were significantly hindered by the high ductility, spontaneous cleaving and bending of the crystals. This resulted in the formation of numerous defects upon grinding, and other disorder-related phenomena, in a system already hampered by high X-ray absorbance. Nonetheless, a sample preparation protocol for SAED experiments is reported here, and shown to be as a fruitful alternative to the otherwise routine PXRD technique. Since TEM-based techniques are typically less accessible in regular research and probe only a very small sample volume, developing more reliable and less time-consuming PXRD investigations is a challenging but logical next step in studying these kinds of materials.

Chapter 6

K_xRhO_2: Self-Sealing Crucibles

6.1 Introduction

Given the versatility of the ground states that can be achieved by various cation levels x in Na_xCoO_2 that were discussed at length in Section 1.4 (page 14), it is very interesting to explore the phase diagrams of other, related materials by chemical means. Coupled charge and spin dynamics in the cobalt oxides appears as a very attractive target for a chemical tuning knob. The heavier analogs of cobaltates—rhodates—offer stronger spin-orbit coupling effects that impact the energy diagram of the transition-metal d-orbitals. For example, elemental Co and Rh are in the same column in the Periodic Table, but due to a larger spin-orbit coupling ($\approx 0.1\,\mathrm{eV}$), the electron configuration of Rh is $[\mathrm{Kr}]5s^1 4d^8$ in contrast to $[\mathrm{Ar}]4s^2 3d^7$ of Co. These effects may also significantly alter the correlated behavior of the system. The research presented in this chapter is centered on K_xRhO_2, which can be expected to show different physical properties in comparison to the alkali metal cobaltates.

Investigation of the A_xRhO_2 (A = Na; K) rhodates is still at an early stage. The first studies showed that K also serves as an electron-donor unit for the conducting $[RhO_2]$ triangular layer.[160,161] The Rh analogs may exhibit weaker electron correlations than the respective cobaltates (the former show increased bandwidths in the electronic band diagrams), but possess an advantage of strongly enhanced transport. Due to those features, K_xRhO_2 and Na_xRhO_2 are predicted to host an array of interesting electronic properties. For example, $K_{0.875}RhO_2$ is expected to host giant thermoelectric effect, with the power factor exceeding that of $Na_{0.88}CoO_2$ by more than 50%.[160] Also, these predictions are already proved to be fruitful in experiment: the report by Shibasaki et al.[162] shows that in transport $K_{0.49}RhO_2$ demonstrates metallic behavior with a moderate Seebeck coefficient ($40\,\mu\mathrm{V\,K^{-1}}$), and according to the following reports this behavior enhances with increasing of potassium content—with the Seebeck coefficient increasing to $46\,\mu\mathrm{V\,K^{-1}}$ for $K_{0.63}RhO_2$, while retaining clearly metallic conductivity.[161]

Nonetheless, the experimental data on the synthesis and characterization of A_xRhO_2, especially the potassium variant, K_xRhO_2, are rather scarce. The first account on the synthesis of polycrystalline $ARhO_2$ (A = Li, Na, K) via solid-state reaction between stoichiometric amounts of A_2CO_3 and Rh_2O_3 at 900 °C in dry oxygen atmosphere dates back to 1987.[163] Atomic absorption spectroscopy and combustion microanalysis established (nearly) perfect stoichiometry of the as-grown phases. Unlike $LiRhO_2$ and $NaRhO_2$, $KRhO_2$ was found to react spontaneously with water on exposure to air, indicated by observed increased interlayer spacing. It was concluded that x is close to 0.6 in the hydrated compound. The given indicative unit cell parameters are: 15.7 Å with 5.23 Å interlayer distance in the non-hydrated $KRhO_2$ and for hydrated $K_{0.6}RhO_2$ these values increase to 20.2 Å and 6.74 Å respectively.

The first synthetic report of single crystal K_xRhO_2 is presented by Yubuta et al.:[164] the authors report self-flux growth by cooling of K_2CO_3:Rh_2O_3 (25:1 molar ratio, 13.5:1 mass ratio) reaction mixture at a rate $2\,^\circ\mathrm{C\,h^{-1}}$ from starting temperature of 1100 °C. After the synthesis the crystals were washed in water to remove the flux. Unfortunately, the authors do not discuss the synthesis in any great detail. The composition is established to be $K_{0.49}RhO_2$ via wave-dispersive x-ray spectroscopy (WDX) and the lattice parameters to be $a = 3.065$ Å and $c = 13.60$ Å. Interestingly, even though the

crystals were washed with water, the lattice parameters seem to correspond to non-hydrated variant, possibly hinting at kinetic limitations of the hydration process. Yao et al.[161] report the growth of the $K_{0.63}RhO_2$ compound by "spontaneous nucleation from solution". A mixture of Rh_2O_3 with excess of K_2CO_3 (1:11 mass ratio) was loaded in an alumina crucible, and the setup underwent heat treatment with the profile similar to the previous work.[164] Yao et al.[161] report "many hexagonal platelets" that were retrieved after washing the mixture with distilled water, without specifying the part of the crucible where the crystals grew. Another interesting difference between the potassium and sodium variants is the composition that forms initially. For sodium compound, the stoichiometric composition forms, while for potassium, the reported composition is $K_{0.63}RhO_2$, which is rather suprising given lower alkaline metal to rhodium ratio then in the previous work.

Zhang et al.[99] in their report of $NaRhO_2$ single crystal growth provide a bit more detail about the synthesis and paint a different picture. The growth was carried out in an alumina crucible from a Rh_2O_3 and Na_2CO_3 mixture. The crucible was covered with a perforated lid to control the speed of sodium carbonate evaporation. The setup was heated to 1100°C and held at this temperature for 3 days, after which the setup was slowly cooled to 850°C. After growth the crystals were also washed with the deionised water to remove the flux. The authors specifically highlight that the growth happened by *vapor transport*, due to the observation that crystals form on the walls of the crucible above the melt.

The chemistry of alkaline metals is rather similar, and the equlibrium atmosphere above both K_2CO_3 and Na_2CO_3 shows significant CO_2 partial pressure at 1100 °C. This hints at thermal decomposition of the flux in all cases mentioned above, since the synthesis was carried out in open systems. Due to this transformation, kinetic considerations might become important, i.e. the amount of time spent at maximum temperature, as well as restrictions in gas mass flow from the reaction volume. This complexity with many equilibria makes these rhodate compounds interesting systems for further crystal growth optimization.

To summarize, the layered alkaline metal rhodates, and especially K_xRhO_2, are interesting materials with several "knobs" to adjust their chemical, crystallographic and physical properties. The ability to change the alkaline metal element, together with the off-stoichiometry in case of the potassium compound show a strong case for attempting to alter formal oxidation state of rhodium, and thus electronic properties of the material. To enable such manipulation, the parameters involved in the synthesis of the material need to be well understood. In this chapter, the synthesis of K_xRhO_2 is described, attempts at substitution at both the potassium and rhodium sites are presented, as is a previously unreported synthetic approach involving *in situ* sealing of the reaction vessel by potassium containing oxide or carbonate derived melt.

6.2 Synthesis

The synthesis method was adopted from Yao et al..[161] First, right before the reaction mixture preparation, potassium carbonate (EMSURE, 99 %) was ground and heat-treated for a day at 250 °C in an alumina crucible to decompose any crystal hydrates that might have formed during storage and remove moisture. Rhodium oxide (III) (Alfa Aesar, 99.9 %) and the potassium carbonate were mixed together in an agate mortar. For the attempts at substitution in the parent compound, the reaction mixture then also contained Barium Chloride (Alfa Aesar, 99.998 %) or Ruthenium Oxide (IV) (ChemPur, 90.9 %). The mass ratios in the reaction mixtures is presented in Tab. 6.1. The reaction mixture was put in an alumina crucible with the lid which in turn was placed into a box furnace. The furnace was heated up to 800 °C at 100 °C h^{-1}, and heated further to 1200 °C at 12 °C h^{-1}. This slowdown at last leg of the heating was implemented to decrease the decomposition rate of K_2CO_3. Afterwards, the reaction mixture was held at the maximum temperature of 1200 °C for 2 h to ensure full solution of Rh_2O_3. Afterwards, the furnace was cooled to 950 °C over 72 h, after which synthesis proceeded by slow cooling to 700 °C over 125 h. Finally, the furnace was switched off and cooled to ambient temperature naturally. During earlier attempts at the synthesis, in some experiments the lid of the crucible was displaced, most probably by escaping CO_2 during potassium carbonate decomposition, resulting in unwanted flux evaporation. To alleviate this effect piece of firebrick was

Table 6.1: Nominal compositions of reaction mixtures and approximate compositions estimated by SEM-EDX. EDX composition is normalized to 1 mol of rhodium. Oxygen content is not measured directly assumed to be stoichiometric

Batch #	Reaction mixture/g				SEM-EDX
	Rh_2O_3	K_2CO_3	$BaCl_2$	RuO_2	
1	0.300	4.084	—	—	$K_{0.65(2)}Rh_{1.00(2)}O_2$
2	0.3005	4.0817	—	—	$K_{0.68(6)}Rh_{1.0(1)}O_2$
3	0.303	3.0613	—	—	$K_{0.57(5)}Rh_{1.0(1)}O_2$
4	0.380	2.994	0.5054	—	*see text*
5	0.2713	3.064	—	0.0329	”

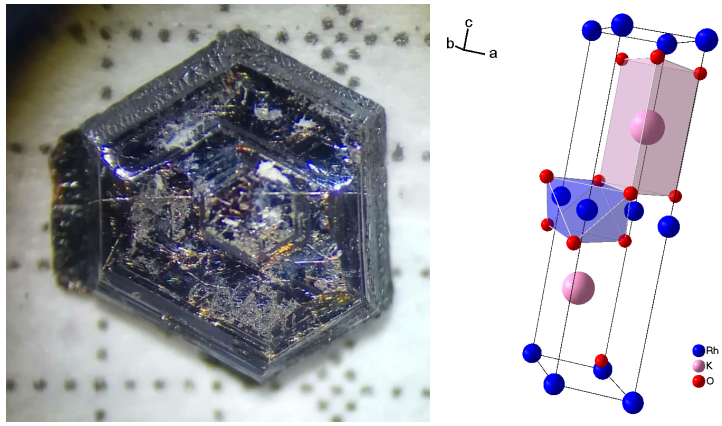

Figure 6.1: Image of K_xRhO_2 crystal on millimeter scale (left panel),[165] and K_xRhO_2 structure (right panel)[161]

put on top of the lid to hold the lid in place. Otherwise the synthesis proceeded with the same procedure as described above. Interestingly, in the case of the weighted lid, the cap of the crucible was soldered to the crucible itself. This sealing is most plausibly caused by a potassium-containing oxide or carbonate, derived from partial decomposition of K_2CO_3, which can be represented in simplified form as:

$$K_2CO_3 \overset{\Delta}{\rightleftharpoons} K_2O + CO_2\uparrow \tag{6.1}$$

The sealing substance wan not analyzed, but it is plausible that it may be K_2O. This self-sealing effect is an interesting feature of the synthesis, as it prevents the flux from escaping the crucible, while saves effort of working in sealed containers, which itself also brings the risks associated with pressure buildup. The resulting solidified flux with embedded crystals was dissolved by repeated washing with cold water. After transferring the crystals to a separate dish, the flux residue was washed off with room-temperature $50\%_{vol}$ ethanol solution in deionized water. Afterwards the crystals were dried on paper towels, and transferred to an argon glovebox to prevent crystal deterioration.

6.3 Composition and Morphology

Crystals of the unsubstituted composition in batches 1 and 2 (refer to Table 6.1 for batch number) showed a hexagonal tabular habit with dimensions of up to several millimeters. Crystals are black with metallic luster. An image of typical crystal from these batches is presented in Figure 6.1. Crystals cleave easily along the platelet plane. To check the stability of the crystals in air, small amount was

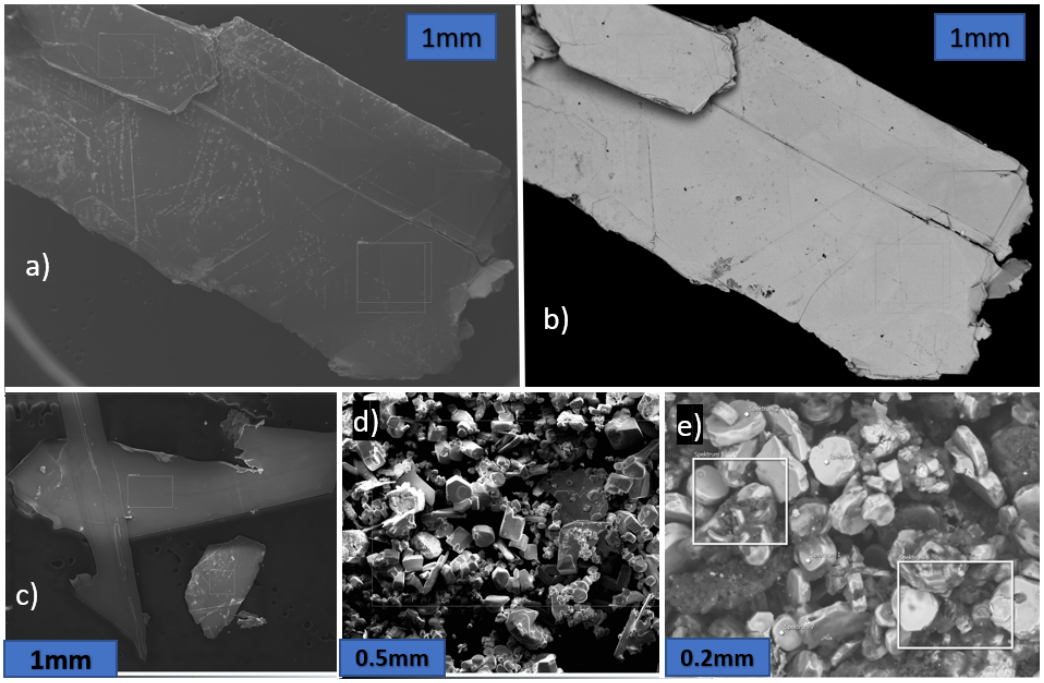

Figure 6.2: SEM images of K_xRhO_2

SEM images: SE (a) and BSE (b) images for a crystal in batch 1. Notice growth steps at 60° angles. Topography image of several flakes from batch 3 (c), showing inferior morphology to batches 1 and 2. The topography images from batches 4 (d) and 5 (e) showing morphology of acquired microcrystals.

left in a Petri dish exposed to ambient air. On the timescale of a week, crystals started to visually deteriorate in shape and formation of white decomposition products was noted. All further handling of the crystals was carried out in dry argon atmosphere. Crystals were studied further by SEM-EDX. Microscopy images (Figure 6.2 a-b) showed even surfaces both in Z and topography contrast. Surfaces show clear growth steps, and with endges at regular 60° angles.

Before moving to the composition analysis, it is worth noting that, because potassium-containing layered oxides can be air- and moisture-sensitive, and because light elements such as oxygen are difficult to quantify by SEM-EDX, this compositions should be treated as approximate. Throughout this chapter oxygen content is assumed to be stoichiometric, i.e. 2 mol O per 1 mol Rh, unless stated otherwise. The results of spectroscopic analysis are presented in Tab. 6.1. The first two batches show reproducible composition, with a potassium content of ≈ 0.65 if rhodium content is normalized to unity.

Batch 3 was synthesized with lower amount of potassium carbonate in a attempt to increase the Rh^{III} content in the final compound. While we achieved slightly lower potassium content, EDX results show $K_{0.57(5)}Rh_{1.0(1)}O_2$ composition, the morphology of the crystals suffered greatly. Crystals were acquired in the form of very fragile, thin, irregular flakes (Figure 6.2 c). The sudden change of morphology can be explained by oversaturation of the Rh_2O_3 solution. Since the growth was carried out from K_2CO_3 self-flux, lowering the potassium to rhodium ratio translates to increasing the rhodium oxide concentration. To attempt the crystallization of more potassium-deficient composition apparently different solvent needs to be identified.

Attempts at substitution at the potassium (batch 4) and rhodium (batch 5) sites were made. Addition of barium chloride to the reaction caused precipitation of the microcrystals, with characteristic

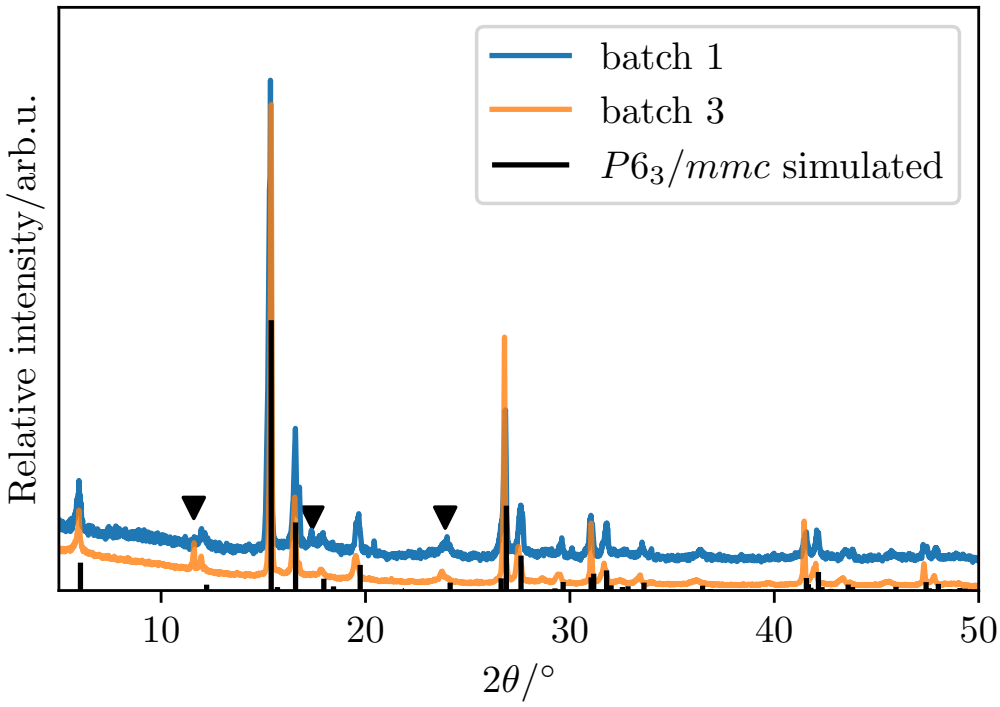

Figure 6.3: Powder diffraction patterns for batch 1 and batch 3. Theoretical pattern for $KRhO_2$ in $NaCoO_2$ structure type is overlaid for clarity.

size of around 100 µm. This suggests that oversaturation happened early in the crystallization process. The relevant microscopy images are presented in Figure 6.2 d. Interestingly, the powder grains show a different morphology to the bulk crystals: in addition to a minority of thin irregular-shaped platelets (similar in morphology to unsubstituted crystals from batch 3), there are bulk hexagonal prisms present. These prisms are noticeably brighter in the SEM SE image. The composition of the resulting precipitate varies greatly depending on the location of the EDX measurement. It is worth noting that potassium didn't precipitate with the crystals, according to these EDX results composition shows Ba:Rh ratio of about 1:1, with only traces of potassium present.

In batch 5, ruthenium oxide was added to the reaction mixture. The resulting microcrystals are presented in Figure 6.2 e. The microcrystals are of irregular chunky shape, with size of around 100 µm. Interestingly, the resulting morphology of the grains is completely different from tabular hexagonal shape of unsubstituted crystals. The EDX spectroscopy results show no presence of ruthenium in the microcrystals.The potassium to rhodium ratio varies throughout the sample. Normalized composition varies in $K_{0.55}RhO_2$–$K_{0.65}RhO_2$ range assuming stoichiometric oxygen content.

At this point, the attempted substitution attempts were considered unsuccessful, and further investigation and method development for this lies beyond the scope of this work. The focus therefore shifted to the unsubstituted K_xRhO_2, which was further characterized by X-ray diffraction and magnetization measurements.

6.4 Crystal Structure

To investigate the structure of the acquired crystals, powder X-ray diffraction was employed. Measured patterns for batches 1 and 3 are presented in Figure 6.3. The patterns were indexed in a $P6_3/mmc$

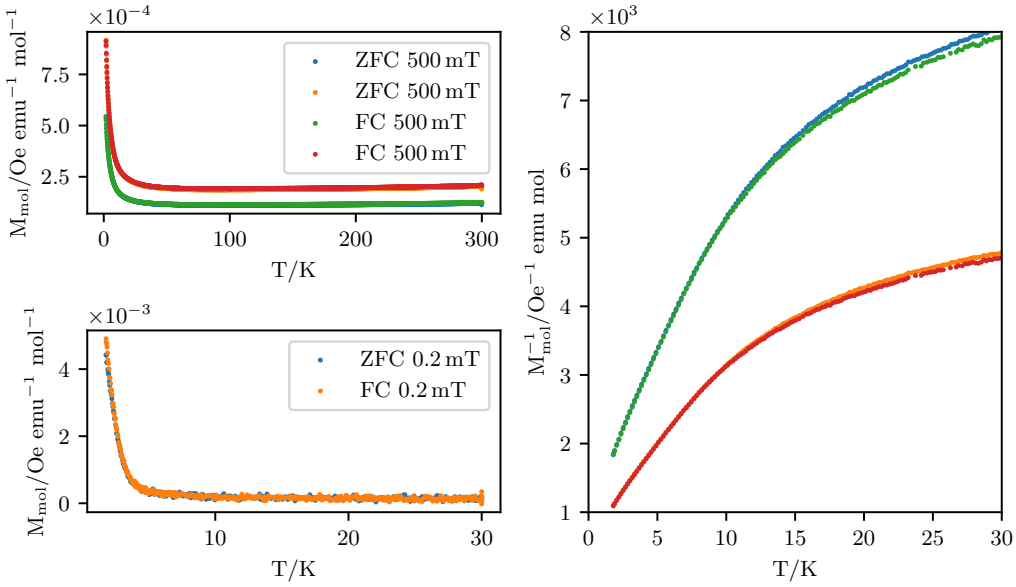

Figure 6.4: SQUID Temperature dependence of molar magnetic moment of $K_{0.65}RhO_2$. Dependence measured with extenal field of 0.5 T in and out of *ab* plane, measured with zero-field and field cooling (top left panel), with temperature dependence of inverse magnetization at low temperatures (right panel), notice non-linear behavior of magnetization. Zero-field and field cooled temperature dependence in external field of 2 mT oriented in *ab* plane (bottom left)

space group, consistent with $NaCoO_2$ structure type. The X-ray diffraction data are in agreement with previously reported structural data for K_xRhO_2.[161] From a simple peak position analysis in a hexagonal crystal family, the lattice parameters were estimated to be $a = 3.0$ Å and $c = 13.2$ Å. While the a parameter agrees with the one reported by Yao et al.[161] nicely, c is off by 0.3 Å. This discrepancy can be attributed to high error of manual lattice parameter determination as well as structural disorder in the material.

The full-profile analysis is complicated due to presence of peaks of different shapes. Peaks of the $hk0$ family are sharp, showing a strong lorenzian contribution. However, the peaks with the l component are significantly broader, showing a complicated peak shape with shoulders or sometimes even split. This is an indication of structural disorder along crystallographic c axis, and challenges the "single crystal" nature of the material. To alleviate such problems, further investigation is needed, both from the material synthesis side (i.e. growth of less defective crystals) and from the characterization side, e.g. probing the material with local methods, such as TEM, and investigation of the atomic pair distribution function, as well as refining the structural model with a disordered structure in mind.

6.5 Magnetization

The magnetic properties of $K_{0.65}RhO_2$ were measured using VSM-SQUID magnetometer. The magnetization of potassium rhodate presented in the Figure 6.4 show paramagnetic behaviour, as expected due to rhodium's mixed formal oxidation state, Rh^{3+}/Rh^{4+}. Rh^{4+} has the electronic configuration $[Kr]5s^04d^5$, so these unpaired $4d$ electrons can provide a paramagnetic response to the external field. The top left panel of the Figure 6.4 measurements in an external field of 0.5 T are presented, illustrating the paramagnetic behavior. Interestingly, these measurements in the *ab* plane

show no signs of the feature around 50 K which was reported by Yao et al..[161] Such behavior could be due to e.g. differences sample preparation, potassium content, hydration state, or stacking disorder. The inverse magnetization doesn't follow the Curie-Weiss law at lower temperatures (Figure 6.4, right panel). These differences to the previously reported data highlight the underlying complexity of the relations between sample preparation and physical properties, and warrants further investigation of the structure of the compound, as well as the magnetic properties, and warrant further investigation of both the crystal structure and magnetic response.

To further check for low-temperature phenomena such as superconductivity, a measurement at an external field of only 2 mT was carried out, both in the field-cooled and zero field cooled regimen, as shown in Figure 6.4, bottom left panel. The measurement shows no signs of any transition down to 1.8 K.

6.6 Summary and Outlook

In conclusion, the synthesis of K_xRhO_2 was successfully carried out via modified K_2CO_3 flux method. The novel synthesis method involved *in situ* sealing of the reaction vessel by a potassium-containing oxide or carbonate derived from the flux, plasiubly related to partial decomposition of potassium carbonate. This self-sealing effect suppresses flux loss during the high-temperature synthesis while avoiding the use of a fully sealed reaction container.

The parent K_xRhO_2 phase was obtained, and attempts at substitution on both the K and Rh sites were carried out. The composition and morphology of the resulting crystals were assessed by SEM and EDX. The EDX-estimated compositions of the unsubstituted crystals are close to $K_{0.65}RhO_2$ for the most reproducible batches, assuming stoichiometric oxygen. Because potassium and oxygen are difficult to quantify reliably by SEM-EDX, these compositions should be treated as approximate. Substitution attempts led to pronounced changes in crystal morphology, but no reliable incorporation of the substituting elements was observed by EDX. These attempts were therefore considered unsuccessful, indicating that further screening of substituting elements, solvents and growth conditions is needed. For the parent compound, an attempt to vary x by reducing the amount of K_2CO_3 led to a slightly lower EDX-estimated potassium content, but this was accompanied by a drastic deterioration of crystal morphology. This behavior is most likely related to oversaturation during crystallization. To access more potassium-deficient crystals with preserved morphology, a different solvent or a more controlled growth protocol will likely be required. PXRD data are consistent with a layered $NaCoO_2$-type average structure for $KRhO_2$. However, the diffraction patterns show strongly anisotropic peak shapes: hk0 reflections are relatively sharp, whereas reflections with a non-zero l component are broadened, asymmetric or split. This indicates substantial stacking disorder along the crystallographic *c* axis. Therefore, the present PXRD data should not be taken as a complete structural confirmation. A robust structural model will require further diffraction or local-structure analysis, ideally including explicit treatment of stacking disorder. Magnetic measurements on EDX-estimated $K_{0.65}RhO_2$ show paramagnetic behavior and no sign of superconductivity down to 1.8 K. The data differ in some respects from previously reported measurements, in particular by the absence of a feature around 50 K. This discrepancy further emphasizes the sensitivity of K_xRhO_2 to synthesis conditions, potassium content, hydration state and structural disorder. Future work should therefore combine improved control over the growth chemistry with more detailed structural characterization and systematic magnetic and transport measurements.

References

(1) De Leon, N. P.; Itoh, K. M.; Kim, D.; Mehta, K. K.; Northup, T. E.; Paik, H.; Palmer, B. S.; Samarth, N.; Sangtawesin, S.; Steuerman, D. W. Materials Challenges and Opportunities for Quantum Computing Hardware. *Science* **2021**, *372*, eabb2823.

(2) Hoffmann, A. et al. Quantum Materials for Energy-Efficient Neuromorphic Computing: Opportunities and Challenges. *APL Materials* **2022**, *10*, 070904.

(3) Shuto, N.; Chiyo, A.; Ken, H.; Tanaka, S. Quantum Materials to the Pioneering Future of Computing and Communication. *Fusion of Multidisciplinary Research, An International Journal* **2020**, *1*, 50–62.

(4) Cava, R.; de Leon, N.; Xie, W. Introduction: Quantum Materials. *Chemical Reviews* **2021**, *121*, 2777–2779.

(5) Lv, B. Q.; Qian, T.; Ding, H. Experimental Perspective on Three-Dimensional Topological Semimetals. *Reviews of Modern Physics* **2021**, *93*, 025002.

(6) Novoselov, K. S.; Jiang, D.; Schedin, F.; Booth, T. J.; Khotkevich, V. V.; Morozov, S. V.; Geim, A. K. Two-Dimensional Atomic Crystals. *Proceedings of the National Academy of Sciences* **2005**, *102*, 10451–10453.

(7) Novoselov, K. S.; Geim, A. K.; Morozov, S. V.; Jiang, D.; Zhang, Y.; Dubonos, S. V.; Grigorieva, I. V.; Firsov, A. A. Electric Field Effect in Atomically Thin Carbon Films. *Science* **2004**, *306*, 666–669.

(8) Novoselov, K. S.; Geim, A. K.; Morozov, S. V.; Jiang, D.; Katsnelson, M. I.; Grigorieva, I. V.; Dubonos, S. V.; Firsov, A. A. Two-Dimensional Gas of Massless Dirac Fermions in Graphene. *Nature* **2005**, *438*, 197–200.

(9) Castro Neto, A. H.; Guinea, F.; Peres, N. M. R.; Novoselov, K. S.; Geim, A. K. The Electronic Properties of Graphene. *Reviews of Modern Physics* **2009**, *81*, 109–162.

(10) Young, S. M.; Kane, C. L. Dirac Semimetals in Two Dimensions. *Physical Review Letters* **2015**, *115*, 126803.

(11) Novoselov, K. S.; Jiang, Z.; Zhang, Y.; Morozov, S. V.; Stormer, H. L.; Zeitler, U.; Maan, J. C.; Boebinger, G. S.; Kim, P.; Geim, A. K. Room-Temperature Quantum Hall Effect in Graphene. *Science* **2007**, *315*, 1379–1379.

(12) Andrei, E. Y.; MacDonald, A. H. Graphene Bilayers with a Twist. *Nature Materials* **2020**, *19*, 1265–1275.

(13) Cao, Y.; Fatemi, V.; Fang, S.; Watanabe, K.; Taniguchi, T.; Kaxiras, E.; Jarillo-Herrero, P. Unconventional Superconductivity in Magic-Angle Graphene Superlattices. *Nature* **2018**, *556*, 43–50.

(14) Liang, T.; Gibson, Q.; Ali, M. N.; Liu, M.; Cava, R. J.; Ong, N. P. Ultrahigh Mobility and Giant Magnetoresistance in the Dirac Semimetal Cd_3As_2. *Nature Materials* **2015**, *14*, 280–284.

(15) Ali, M. N.; Xiong, J.; Flynn, S.; Tao, J.; Gibson, Q. D.; Schoop, L. M.; Liang, T.; Haldolaarachchige, N.; Hirschberger, M.; Ong, N. P.; Cava, R. J. Large, Non-Saturating Magnetoresistance in WTe_2. *Nature* **2014**, *514*, 205–208.

(16) Fu, C.; Guin, S. N.; Scaffidi, T.; Sun, Y.; Saha, R.; Watzman, S. J.; Srivastava, A. K.; Li, G.; Schnelle, W.; Parkin, S. S. P.; Felser, C.; Gooth, J. Largely Suppressed Magneto-Thermal Conductivity and Enhanced Magneto-Thermoelectric Properties in $PtSn_4$. *Research* **2020**, *2020*, DOI: 10.34133/2020/4643507.

(17) Huang, X.; Zhao, L.; Long, Y.; Wang, P.; Chen, D.; Yang, Z.; Liang, H.; Xue, M.; Weng, H.; Fang, Z.; Dai, X.; Chen, G. Observation of the Chiral-Anomaly-Induced Negative Magnetoresistance in 3D Weyl Semimetal TaAs. *Physical Review X* **2015**, *5*, 031023.

(18) Wang, W.; Zhang, X.; Xu, H.; Zhao, Y.; Zou, W.; He, L.; Xu, Y. Evidence for Layered Quantized Transport in Dirac Semimetal $ZrTe_5$. *Scientific Reports* **2018**, *8*, 5125.

(19) Mar, A.; Jobic, S.; Ibers, J. A. Metal-Metal vs Tellurium-Tellurium Bonding in WTe_2 and Its Ternary Variants $TaIrTe_4$ and $NbIrTe_4$. *Journal of the American Chemical Society* **1992**, *114*, 8963–8971.

(20) West, A. R. *Solid State Chemistry and Its Applications*, Second edition, student edition; Wiley: Chichester, West Sussex, UK, 2014; 584 pp.

(21) Hoffmann, R. How Chemistry and Physics Meet in the Solid State. *Angewandte Chemie International Edition in English* **1987**, *26*, 846–878.

(22) Pauling, L. *The Nature of the Chemical Bond and the Structure of Molecules and Crystals: An Introduction to Modern Structural Chemistry*, 3rd ed.; Cornell University Press: Ithaca, New York, USA, 1960; 644 pp.

(23) Atkins, P.; Overton, T.; Rourke, J.; Weller, M.; Armstrong, F.; Hagerman, M. *Shriver & Atkins' Inorganic Chemistry*, 5th ed.; Oxford University Press: 2009; 851 pp.

(24) Singleton, J. *Band Theory and Electronic Properties of Solids*; Oxford Master Series in Condensed Matter Physics; Oxford University Press: Oxford ; New York, 2001; 222 pp.

(25) Vainsthein, B. K. *Fundamentals of Crystals: Symmetry, and Methods of Structural Crystallography*; Springer Berlin Heidelberg: Berlin, Heidelberg, 1994.

(26) Yan, B.; Felser, C. Topological Materials: Weyl Semimetals. *Annual Review of Condensed Matter Physics* **2017**, *8*, 337–354.

(27) Xu, Y.; Elcoro, L.; Song, Z.-D.; Wieder, B. J.; Vergniory, M. G.; Regnault, N.; Chen, Y.; Felser, C.; Bernevig, B. A. High-Throughput Calculations of Magnetic Topological Materials. *Nature* **2020**, *586*, 702–707.

(28) Weyl, H. Gravitation and the Electron. *Proceedings of the National Academy of Sciences* **1929**, *15*, 323–334.

(29) Liu, Z. K. et al. Evolution of the Fermi Surface of Weyl Semimetals in the Transition Metal Pnictide Family. *Nature Materials* **2016**, *15*, 27–31.

(30) Lv, B. Q. et al. Observation of Fermi-Arc Spin Texture in TaAs. *Physical Review Letters* **2015**, *115*, 217601.

(31) Burkov, A. A. Chiral Anomaly and Transport in Weyl Metals. *Journal of Physics: Condensed Matter* **2015**, *27*, 113201.

(32) Soluyanov, A. A.; Gresch, D.; Wang, Z.; Wu, Q.; Troyer, M.; Dai, X.; Bernevig, B. A. Type-II Weyl Semimetals. *Nature* **2015**, *527*, 495–498.

(33) Lv, B. Q.; Weng, H. M.; Fu, B. B.; Wang, X. P.; Miao, H.; Ma, J.; Richard, P.; Huang, X. C.; Zhao, L. X.; Chen, G. F.; Fang, Z.; Dai, X.; Qian, T.; Ding, H. Experimental Discovery of Weyl Semimetal TaAs. *Physical Review X* **2015**, *5*, 031013.

(34) Weng, H.; Fang, C.; Fang, Z.; Bernevig, B. A.; Dai, X. Weyl Semimetal Phase in Noncentrosymmetric Transition-Metal Monophosphides. *Physical Review X* **2015**, *5*, 011029.

(35) Xu, S.-Y. et al. Discovery of a Weyl Fermion Semimetal and Topological Fermi Arcs. *Science* **2015**, *349*, 613–617.

(36) Wang, Z.; Sun, Y.; Chen, X.-Q.; Franchini, C.; Xu, G.; Weng, H.; Dai, X.; Fang, Z. Dirac Semimetal and Topological Phase Transitions in A_3Bi (A = Na, K, Rb). *Physical Review B* **2012**, *85*, 195320.

(37) Huang, S.-M.; Xu, S.-Y.; Belopolski, I.; Lee, C.-C.; Chang, G.; Wang, B.; Alidoust, N.; Bian, G.; Neupane, M.; Zhang, C.; Jia, S.; Bansil, A.; Lin, H.; Hasan, M. Z. A Weyl Fermion Semimetal with Surface Fermi Arcs in the Transition Metal Monopnictide TaAs Class. *Nature Communications* **2015**, *6*, 7373.

(38) Sato, M.; Ando, Y. Topological Superconductors: A Review. *Reports on Progress in Physics* **2017**, *80*, 076501.

(39) Sharma, M. M.; Sharma, P.; Karn, N. K.; Awana, V. P. S. Comprehensive Review on Topological Superconducting Materials and Interfaces. *Superconductor Science and Technology* **2022**, *35*, 083003.

(40) Fei, F.; Bo, X.; Wang, R.; Wu, B.; Jiang, J.; Fu, D.; Gao, M.; Zheng, H.; Chen, Y.; Wang, X.; Bu, H.; Song, F.; Wan, X.; Wang, B.; Wang, G. Nontrivial Berry Phase and Type-II Dirac Transport in the Layered Material $PdTe_2$. *Physical Review B* **2017**, *96*, 041201.

(41) Borisenko, S.; Gibson, Q.; Evtushinsky, D.; Zabolotnyy, V.; Büchner, B.; Cava, R. J. Experimental Realization of a Three-Dimensional Dirac Semimetal. *Physical Review Letters* **2014**, *113*, 027603.

(42) Crassee, I.; Sankar, R.; Lee, W.-L.; Akrap, A.; Orlita, M. 3D Dirac Semimetal Cd_3As_2: A Review of Material Properties. *Physical Review Materials* **2018**, *2*, 120302.

(43) Polymorphism - Online Dictionary of Crystallography `https://dictionary.iucr.org/Polymorphism` (accessed 08/07/2024).

(44) Buerger, M. J.; Bloom, M. C. Crystal Polymorphism. *Zeitschrift für Kristallographie - Crystalline Materials* **1937**, *96*, 182–200.

(45) Okamoto, H. The As-Cd (Arsenic-Cadmium) System. *Journal of Phase Equilibria* **1992**, *13*, 147–154.

(46) Pietraszko, A.; Łukaszewicz, K. A Refinement of the Crystal Structure of α''-Cd_3As_2. *Acta Crystallographica Section B: Structural Crystallography and Crystal Chemistry* **1969**, *25*, 988–990.

(47) Stackelberg, M.; Paulus, R. Investigation on phosphides and arsenides of zinc and cadmium. the Zn3P2 lattice. *Z. phys. Chem* **1935**, *28*, 427–460.

(48) Ali, M. N.; Gibson, Q.; Jeon, S.; Zhou, B. B.; Yazdani, A.; Cava, R. J. The Crystal and Electronic Structures of Cd_3As_2, the Three-Dimensional Electronic Analogue of Graphene. *Inorganic Chemistry* **2014**, *53*, 4062–4067.

(49) Steigmann, G. A.; Goodyear, J. The Crystal Structure of Cd_3As_2. *Acta Crystallographica Section B: Structural Crystallography and Crystal Chemistry* **1968**, *24*, 1062–1067.

(50) Wang, Z.; Weng, H.; Wu, Q.; Dai, X.; Fang, Z. Three-Dimensional Dirac Semimetal and Quantum Transport in Cd_3As_2. *Physical Review B* **2013**, *88*, 125427.

(51) Marsh, R. E.; Kapon, M.; Hu, S.; Herbstein, F. H. Some 60 New Space-Group Corrections. *Acta Crystallographica Section B: Structural Science* **2002**, *58*, 62–77.

(52) Ermer, O.; Dunitz, J. D. Least-Squares Refinement of Centrosymmetric Trial Structures in Non-Centrosymmetric Space Groups. A Warning. *Acta Crystallographica Section A: Crystal Physics, Diffraction, Theoretical and General Crystallography* **1970**, *26*, 163–163.

(53) Fjellvåg, H.; Kjekshus, A. Structural Properties of $ZrTe_5$ and $HfTe_5$ as Seen by Powder Diffraction. *Solid State Communications* **1986**, *60*, 91–93.

(54) Mutch, J.; Chen, W.-C.; Went, P.; Qian, T.; Wilson, I. Z.; Andreev, A.; Chen, C.-C.; Chu, J.-H. Evidence for a Strain-Tuned Topological Phase Transition in $ZrTe_5$. *Science Advances* **2019**, *5*, eaav9771.

(55) Li, X.-B. et al. Experimental Observation of Topological Edge States at the Surface Step Edge of the Topological Insulator $ZrTe_5$. *Physical Review Letters* **2016**, *116*, 176803.

(56) Chen, Z.-G.; Chen, R. Y.; Zhong, R. D.; Schneeloch, J.; Zhang, C.; Huang, Y.; Qu, F.; Yu, R.; Li, Q.; Gu, G. D.; Wang, N. L. Spectroscopic Evidence for Bulk-Band Inversion and Three-Dimensional Massive Dirac Fermions in $ZrTe_5$. *Proceedings of the National Academy of Sciences* **2017**, *114*, 816–821.

(57) Jiang, Y.; Dun, Z. L.; Zhou, H. D.; Lu, Z.; Chen, K.-W.; Moon, S.; Besara, T.; Siegrist, T. M.; Baumbach, R. E.; Smirnov, D.; Jiang, Z. Landau-Level Spectroscopy of Massive Dirac Fermions in Single-Crystalline $ZrTe_5$ Thin Flakes. *Physical Review B* **2017**, *96*, 041101.

(58) Xiong, H.; Sobota, J. A.; Yang, S.-L.; Soifer, H.; Gauthier, A.; Lu, M.-H.; Lv, Y.-Y.; Yao, S.-H.; Lu, D.; Hashimoto, M.; Kirchmann, P. S.; Chen, Y.-F.; Shen, Z.-X. Three-Dimensional Nature of the Band Structure of $ZrTe_5$ Measured by High-Momentum-Resolution Photoemission Spectroscopy. *Physical Review B* **2017**, *95*, 195119.

(59) Xu, B.; Zhao, L. X.; Marsik, P.; Sheveleva, E.; Lyzwa, F.; Dai, Y. M.; Chen, G. F.; Qiu, X. G.; Bernhard, C. Temperature-Driven Topological Phase Transition and Intermediate Dirac Semimetal Phase in $ZrTe_5$. *Physical Review Letters* **2018**, *121*, 187401.

(60) Kobayashi, K. Hard X-ray Photoemission Spectroscopy. *Nuclear Instruments and Methods in Physics Research Section A: Accelerators, Spectrometers, Detectors and Associated Equipment* **2009**, *601*, 32–47.

(61) *Surface Science: An Introduction*; Oura, K., Ed.; Advanced Texts in Physics; Springer: Berlin ; New York, 2003; 440 pp.

(62) Guinier (Chairman), A.; Bokij, G. B.; Boll-Dornberger, K.; Cowley, J. M.; Ďurovič, S.; Jagodzinski, H.; Krishna, P.; De Wolff, P. M.; Zvyagin, B. B.; Cox, D. E.; Goodman, P.; Hahn, Th.; Kuchitsu, K.; Abrahams, S. C. Nomenclature of Polytype Structures. Report of the International Union of Crystallography *Ad Hoc* Committee on the Nomenclature of Disordered, Modulated and Polytype Structures. *Acta Crystallographica Section A Foundations of Crystallography* **1984**, *40*, 399–404.

(63) *Powder Diffraction: Theory and Practice*; Dinnebier, R. E., Billinge, S. J. L., Eds.; Royal Society of Chemistry: Cambridge, 2008; 582 pp.

(64) Egami, T.; Billinge, S. J. L. *Underneath the Bragg Peaks: Structural Analysis of Complex Materials*; Pergamon Materials Series v. 7; Pergamon: Kiddington, Oxford, UK ; Boston, 2003; 404 pp.

(65) Kelly, A.; Knowles, K. M. *Crystallography and Crystal Defects*, 1st ed.; Wiley: 2012.

(66) Tilley, R. J. D. *Defects in Solids*; Wiley Series in Special Topics in Inorganic Chemistry; Wiley: Hoboken, NJ, 2008; 529 pp.

(67) Chadha, G. K. Atomic Positions of Three New Polytypes of CdI_2. *Acta Crystallographica Section B: Structural Crystallography and Crystal Chemistry* **1982**, *38*, 3009–3011.

(68) Pałosz, B. Identification of Polytypes of MX_2-type Compounds – Structures of 19 New Polytypes of Cadmium Iodide. *Acta Crystallographica Section B: Structural Crystallography and Crystal Chemistry* **1982**, *38*, 3001–3009.

(69) Zhang, C.; KC, S.; Nie, Y.; Liang, C.; Vandenberghe, W. G.; Longo, R. C.; Zheng, Y.; Kong, F.; Hong, S.; Wallace, R. M.; Cho, K. Charge Mediated Reversible Metal–Insulator Transition in Monolayer $MoTe_2$ and $W_xMo_{1-x}Te_2$ Alloy. *ACS Nano* **2016**, *10*, 7370–7375.

(70) Naidyuk, Y. G.; Bashlakov, D. L.; Kvitnitskaya, O. E.; Piening, B. R.; Shipunov, G.; Efremov, D. V.; Aswartham, S.; Büchner, B. Switchable Topological Domains in Point Contacts Based on Transition Metal Tellurides, 2020.

(71) Qian, X.; Liu, J.; Fu, L.; Li, J. Quantum Spin Hall Effect in Two-Dimensional Transition Metal Dichalcogenides. *Science* **2014**, *346*, 1344–1347.

(72) Fei, Z.; Palomaki, T.; Wu, S.; Zhao, W.; Cai, X.; Sun, B.; Nguyen, P.; Finney, J.; Xu, X.; Cobden, D. H. Edge Conduction in Monolayer WTe_2. *Nature Physics* **2017**, *13*, 677–682.

(73) Wu, S.; Fatemi, V.; Gibson, Q. D.; Watanabe, K.; Taniguchi, T.; Cava, R. J.; Jarillo-Herrero, P. Observation of the Quantum Spin Hall Effect up to 100 Kelvin in a Monolayer Crystal. *Science* **2018**, *359*, 76–79.

(74) Tang, S. et al. Quantum Spin Hall State in Monolayer 1T'-WTe_2. *Nature Physics* **2017**, *13*, 683–687.

(75) Thoutam, L. R.; Wang, Y. L.; Xiao, Z. L.; Das, S.; Luican-Mayer, A.; Divan, R.; Crabtree, G. W.; Kwok, W. K. Temperature-Dependent Three-Dimensional Anisotropy of the Magnetoresistance in WTe_2. *Physical Review Letters* **2015**, *115*, 046602.

(76) Deng, K. et al. Experimental Observation of Topological Fermi Arcs in Type-II Weyl Semimetal $MoTe_2$. *Nature Physics* **2016**, *12*, 1105–1110.

(77) Liang, A. et al. Electronic Evidence for Type II Weyl Semimetal State in $MoTe_2$, 2016.

(78) Belopolski, I. et al. Fermi Arc Electronic Structure and Chern Numbers in the Type-II Weyl Semimetal Candidate $Mo_xW_{1-x}Te_2$. *Physical Review B* **2016**, *94*, 085127.

(79) Huang, L.; McCormick, T. M.; Ochi, M.; Zhao, Z.; Suzuki, M.-T.; Arita, R.; Wu, Y.; Mou, D.; Cao, H.; Yan, J.; Trivedi, N.; Kaminski, A. Spectroscopic Evidence for a Type II Weyl Semimetallic State in $MoTe_2$. *Nature Materials* **2016**, *15*, 1155–1160.

(80) Wu, Y.; Mou, D.; Jo, N. H.; Sun, K.; Huang, L.; Bud'ko, S. L.; Canfield, P. C.; Kaminski, A. Observation of Fermi Arcs in the Type-II Weyl Semimetal Candidate WTe_2. *Physical Review B* **2016**, *94*, 121113.

(81) Wang, W.; Kim, S.; Liu, M.; Cevallos, F. A.; Cava, R. J.; Ong, N. P. Evidence for an Edge Supercurrent in the Weyl Superconductor $MoTe_2$. *Science* **2020**, *368*, 534–537.

(82) Sharma, P.; Xiang, F.-X.; Shao, D.-F.; Zhang, D.; Tsymbal, E. Y.; Hamilton, A. R.; Seidel, J. A Room-Temperature Ferroelectric Semimetal. *Science Advances* **2019**, *5*, eaax5080.

(83) Huang, F.-T.; Joon Lim, S.; Singh, S.; Kim, J.; Zhang, L.; Kim, J.-W.; Chu, M.-W.; Rabe, K. M.; Vanderbilt, D.; Cheong, S.-W. Polar and Phase Domain Walls with Conducting Interfacial States in a Weyl Semimetal $MoTe_2$. *Nature Communications* **2019**, *10*, 4211.

(84) Tao, Y.; Schneeloch, J. A.; Aczel, A. A.; Louca, D. T_d to 1T' Structural Phase Transition in the WTe_2 Weyl Semimetal. *Physical Review B* **2020**, *102*, 060103.

(85) Tao, Y.; Schneeloch, J. A.; Duan, C.; Matsuda, M.; Dissanayake, S. E.; Aczel, A. A.; Fernandez-Baca, J. A.; Ye, F.; Louca, D. Appearance of a T_d^* Phase across the T_d − 1T' Phase Boundary in the Weyl Semimetal $MoTe_2$. *Physical Review B* **2019**, *100*, 100101.

(86) Ren, Z.; Taskin, A. A.; Sasaki, S.; Segawa, K.; Ando, Y. Optimizing $Bi_{1-x}Sb_xTe_{3-y}Se_y$ Solid Solutions to Approach the Intrinsic Topological Insulator Regime. *Physical Review B* **2011**, *84*, 165311.

(87) Niu, C.; Dai, Y.; Zhu, Y.; Ma, Y.; Yu, L.; Han, S.; Huang, B. Realization of Tunable Dirac Cone and Insulating Bulk States in Topological Insulators $(Bi_{1-x}Sb_x)_2Te_3$. *Scientific Reports* **2012**, *2*, 976.

(88) Rogacheva, E. I.; Nikolaenko, G. O.; Nashchekina, O. N. Transport and Thermoelectric Properties of the $Pb_{1-x}Sn_xTe$ Topological Crystalline Insulator in the Vicinity of the Band Inversion. *Journal of Physics and Chemistry of Solids* **2023**, *183*, 111635.

(89) Dahal, R.; Deng, L. Z.; Poudel, N.; Gooch, M.; Wu, Z.; Wu, H. C.; Yang, H. D.; Chang, C. K.; Chu, C. W. Tunable Structural Phase Transition and Superconductivity in the Weyl Semimetal $Mo_{1-x}W_xTe_2$. *Physical Review B* **2020**, *101*, 140505.

(90) Qi, Y. et al. Superconductivity in Weyl Semimetal Candidate $MoTe_2$. *Nature Communications* **2016**, *7*, 11038.

(91) Yan, Z.; Wu, Z.; Huang, W. Vortex End Majorana Zero Modes in Superconducting Dirac and Weyl Semimetals. *Physical Review Letters* **2020**, *124*, 257001.

(92) Zunger, A. Beware of Plausible Predictions of Fantasy Materials. *Nature* **2019**, *566*, 447–449.

(93) Witte, P.; Koten, A. M. van; Kamminga, M. E. Tuning the Magnetic Properties of van Der Waals Materials by Intercalation. *Materials Advances* **2024**, *5*, 6702–6718.

(94) Augustyn, V. Tuning the Interlayer of Transition Metal Oxides for Electrochemical Energy Storage. *Journal of Materials Research* **2017**, *32*, 2–15.

(95) Foo, M. L.; Wang, Y.; Watauchi, S.; Zandbergen, H. W.; He, T.; Cava, R. J.; Ong, N. P. Charge Ordering, Commensurability, and Metallicity in the Phase Diagram of the Layered Na_xCoO_2. *Physical Review Letters* **2004**, *92*, 247001.

(96) Takada, K.; Sakurai, H.; Takayama-Muromachi, E.; Izumi, F.; Dilanian, R.; Sasaki, T. Superconductivity in Two-Dimensional CoO_2 Layers. *Nature* **2003**, *422*, 53–5.

(97) Fujita, K.; Mochida, T.; Nakamura, K. High-Temperature Thermoelectric Properties of $NaxCoO_{2-\delta}$ Single Crystals. *Japanese Journal of Applied Physics* **2001**, *40*, 4644.

(98) Wang, Y.; Rogado, N. S.; Cava, R. J.; Ong, N. P. Spin Entropy as the Likely Source of Enhanced Thermopower in $Na_xCo_2O_4$. *Nature* **2003**, *423*, 425–428.

(99) Zhang, B.-B.; Wang, C.; Dong, S.-T.; Lv, Y.-Y.; Zhang, L.; Xu, Y.; Chen, Y. B.; Zhou, J.; Yao, S.-H.; Chen, Y.-F. Preparation, Structure Evolution, and Metal–Insulator Transition of Na_xRhO_2 Crystals ($0.25 \leq x \leq 1$). *Inorganic Chemistry* **2018**, *57*, 2730–2735.

(100) Schaak, R. E.; Klimczuk, T.; Foo, M. L.; Cava, R. J. Superconductivity Phase Diagram of $Na_xCoO_{>2}\times 1.3H_2O$. *Nature* **2003**, *424*, 527–529.

(101) Kawasaki, S.; Motohashi, T.; Shimada, K.; Ono, T.; Kanno, R.; Karppinen, M.; Yamauchi, H.; Zheng, G.-q. Measurement of Electron Correlations in Li_xCoO_2 ($x = 0.0$–0.35) Using ^{59}Co Nuclear Magnetic Resonance and Nuclear Quadrupole Resonance Techniques. *Physical Review B* **2009**, *79*, 220514.

(102) Zandbergen, H. W.; Foo, M.; Xu, Q.; Kumar, V.; Cava, R. J. Sodium Ion Ordering in Na_xCoO_2: Electron Diffraction Study. *Physical Review B* **2004**, *70*, 024101.

(103) intensive quantity. **2025**, DOI: doi:10.1351/goldbook.I03074.

(104) Atkins, P. W.; De Paula, J. *Physical Chemistry*; Oxford University Press: Oxford, 2006.

(105) Grest, G.; Anderson, M.; Srolovitz, D.; Rollett, A. Abnormal Grain Growth in Three Dimensions. *Scripta Metallurgica et Materialia* **1990**, *24*, 661–665.

(106) Lee, B.-K.; Chung, S.-Y.; Kang, S.-J. L. Grain Boundary Faceting and Abnormal Grain Growth in $BaTiO_3$. *Acta Materialia* **2000**, *48*, 1575–1580.

(107) Rios, P. R. Abnormal Grain Growth Development from Uniform Grain Size Distributions. *Acta Materialia* **1997**, *45*, 1785–1789.

(108) Omori, T.; Kusama, T.; Kawata, S.; Ohnuma, I.; Sutou, Y.; Araki, Y.; Ishida, K.; Kainuma, R. Abnormal Grain Growth Induced by Cyclic Heat Treatment. *Science* **2013**, *341*, 1500–1502.

(109) Bae, I.-J.; Baik, S. Abnormal Grain Growth of Alumina. *Journal of the American Ceramic Society* **1997**, *80*, 1149–1156.

(110) Canfield, P. C.; Kong, T.; Kaluarachchi, U. S.; Jo, N. H. Use of Frit-Disc Crucibles for Routine and Exploratory Solution Growth of Single Crystalline Samples. *Philosophical Magazine* **2016**, *96*, 84–92.

(111) Goldstein, J. I.; Newbury, D. E.; Michael, J. R.; Ritchie, N. W.; Scott, J. H. J.; Joy, D. C. *Scanning Electron Microscopy and X-Ray Microanalysis*; Springer New York: New York, NY, 2018.

(112) Ponor Teardrop-shaped Electron–Matter Interaction Volume and Limits to the Depths from Which Each Signal Type Can Be Emitted or Detected. 2020.

(113) Koshikawa, T.; Shimizu, R. A Monte Carlo Calculation of Low-Energy Secondary Electron Emission from Metals. *Journal of Physics D: Applied Physics* **1974**, *7*, 1303–1315.

(114) Muso Principle of EDX, 2007.

(115) MBirkholz Hemisphere of Diffraction Showing the Incoming and Diffracted Beams K0 and K That Are Inclined by an Angle Theta with Respect to the Sample Surface. 2021.

(116) Rietveld, H. M. A Profile Refinement Method for Nuclear and Magnetic Structures. *Journal of Applied Crystallography* **1969**, *2*, 65–71.

(117) *Transmission Electron Microscopy*; Carter, C. B., Williams, D. B., Eds.; Springer International Publishing: Cham, 2016.

(118) Shipunov, G. et al. Polymorphic $PtBi_2$ Growth, Structure, and Superconducting Properties. *Physical Review Materials* **2020**, *4*, 124202.

(119) Yang, X.; Bai, H.; Wang, Z.; Li, Y.; Chen, Q.; Chen, J.; Li, Y.; Feng, C.; Zheng, Y.; Xu, Z.-a. Giant Linear Magneto-Resistance in Nonmagnetic $PtBi_2$. *Applied Physics Letters* **2016**, *108*, 252401.

(120) Wu, B.; Barrena, V.; Suderow, H.; Guillamón, I. Huge Linear Magnetoresistance Due to Open Orbits in $PtBi_2$. *Physical Review Research* **2020**, *2*, 022042.

(121) Feng, Y. et al. Rashba-like Spin Splitting along Three Momentum Directions in Trigonal Layered $PtBi_2$. *Nature Communications* **2019**, *10*, 4765.

(122) Ishizaka, K. et al. Giant Rashba-type Spin Splitting in Bulk BiTeI. *Nature Materials* **2011**, *10*, 521–526.

(123) Nie, X.-A. et al. Robust Hot Electron and Multiple Topological Insulator States in PtBi $_2$. *ACS Nano* **2020**, *14*, 2366–2372.

(124) Mandal, M.; Drucker, N. C.; Siriviboon, P.; Nguyen, T.; Boonkird, A.; Lamichhane, T. N.; Okabe, R.; Chotrattanapituk, A.; Li, M. Topological Superconductors from a Materials Perspective. *Chemistry of Materials* **2023**, *35*, 6184–6200.

(125) Veyrat, A.; Labracherie, V.; Bashlakov, D. L.; Caglieris, F.; Facio, J. I.; Shipunov, G.; Charvin, T.; Acharya, R.; Naidyuk, Y.; Giraud, R.; Van Den Brink, J.; Büchner, B.; Hess, C.; Aswartham, S.; Dufouleur, J. Berezinskii–Kosterlitz–Thouless Transition in the Type-I Weyl Semimetal $PtBi_2$. *Nano Letters* **2023**, *23*, 1229–1235.

(126) Wang, J.; Chen, X.; Zhou, Y.; An, C.; Zhou, Y.; Gu, C.; Tian, M.; Yang, Z. Pressure-Induced Superconductivity in Trigonal Layered $PtBi_2$ with Triply Degenerate Point Fermions. *Physical Review B* **2021**, *103*, 014507.

(127) Kuibarov, A.; Suvorov, O.; Vocaturo, R.; Fedorov, A.; Lou, R.; Merkwitz, L.; Voroshnin, V.; Facio, J. I.; Koepernik, K.; Yaresko, A.; Shipunov, G.; Aswartham, S.; Brink, J. van den; Büchner, B.; Borisenko, S. Evidence of Superconducting Fermi Arcs. *Nature* **2024**, *626*, 294–299.

(128) Majchrzak, P.; Sanders, C.; Zhang, Y.; Kuibarov, A.; Suvorov, O.; Springate, E.; Kovalchuk, I.; Aswartham, S.; Shipunov, G.; Büchner, B.; Yaresko, A.; Borisenko, S.; Hofmann, P. Electron Dynamics in a Three-Dimensional Brillouin Zone Analysed by Machine Learning `http://arxiv.org/abs/2406.10551` (accessed 07/22/2024), pre-published.

(129) Majchrzak, P.; Sanders, C.; Zhang, Y.; Kuibarov, A.; Suvorov, O.; Springate, E.; Kovalchuk, I.; Aswartham, S.; Shipunov, G.; Büchner, B.; Yaresko, A.; Borisenko, S.; Hofmann, P. Ultrafast Carrier Dynamics throughout the Three-Dimensional Brillouin Zone of the Weyl Semimetal $PtBi_2$ `http://arxiv.org/abs/2406.10550` (accessed 07/22/2024), pre-published.

(130) Schimmel, S.; Fasano, Y.; Hoffmann, S.; Puig, J.; Shipunov, G.; Baumann, D.; Aswartham, S.; Büchner, B.; Hess, C. High-T_c Surface Superconductivity in Topological Weyl Semimetal t-$PtBi_2$ `http://arxiv.org/abs/2302.08968` (accessed 07/22/2024), pre-published.

(131) Roessler, F. Synthese Einiger Erzmineralien Und Analoger Metallverbindungen Durch Auflösen Und Krystallisierenlassen Derselben in Geschmolzenen Metallen. *Zeitschrift für anorganische Chemie* **1895**, *9*, 31–77.

(132) Алексеевский, Н.; Гайдуков, Ю. Исследование сплавов висмута в области сверхнизких температур. *Журнал экспериментальной и теоретической физики* **1953**, *25*, 383—384.

(133) Okamoto, H. The Bi-Pt (Bismuth-Platinum) System. *Journal of Phase Equilibria* **1991**, *12*, 207–210.

(134) Biswas, T.; Schubert, K. Strukturuntersuchungen in den mischungen Pt-Tl-Pb und Pt-Pb-Bi. *Journal of the Less Common Metals* **1969**, *19*, 223–243.

(135) Gibson, Q. D.; Schoop, L. M.; Muechler, L.; Xie, L. S.; Hirschberger, M.; Ong, N. P.; Car, R.; Cava, R. J. Three-Dimensional Dirac Semimetals: Design Principles and Predictions of New Materials. *Physical Review B* **2015**, *91*, 205128.

(136) Gao, W. et al. Extremely Large Magnetoresistance in a Topological Semimetal Candidate Pyrite $PtBi_2$. *Physical Review Letters* **2017**, *118*, 256601.

(137) Zhao, L. Fermi Surface and Carrier Compensation of Pyrite-Type $PtBi_2$ Revealed by Quantum Oscillations. *Physical Review B* **2018**, *98*, DOI: `10.1103/PhysRevB.98.085137`.

(138) Yao, Q. et al. Bulk and Surface Electronic Structure of Hexagonal Structured $PtBi2_2$ Studied by Angle-Resolved Photoemission Spectroscopy. *Physical Review B* **2016**, *94*, 235140.

(139) Xu, C. Q.; Xing, X. Z.; Xu, X.; Li, B.; Chen, B.; Che, L. Q.; Lu, X.; Dai, J.; Shi, Z. X. Synthesis, Physical Properties, and Band Structure of the Layered Bismuthide $PtBi_2$. *Physical Review B* **2016**, *94*, 165119.

(140) Thirupathaiah, S.; Kushnirenko, Y.; Haubold, E.; Fedorov, A. V.; Rienks, E. D. L.; Kim, T. K.; Yaresko, A. N.; Blum, C. G. F.; Aswartham, S.; Büchner, B.; Borisenko, S. V. Possible Origin of Linear Magnetoresistance: Observation of Dirac Surface States in Layered $PtBi_2$. *Physical Review B* **2018**, *97*, 035133.

(141) Gao, W.; Zhu, X.; Zheng, F.; Wu, M.; Zhang, J.; Xi, C.; Zhang, P.; Zhang, Y.; Hao, N.; Ning, W.; Tian, M. A Possible Candidate for Triply Degenerate Point Fermions in Trigonal Layered PtBi 2. *Nature Communications* **2018**, *9*, 3249.

(142) Kaiser, M.; Baranov, A. I.; Ruck, M. Bi_2Pt(hP9) by Low-Temperature Reduction of $Bi_{13}Pt_3I_7$: Reinvestigation of the Crystal Structure and Chemical Bonding Analysis. *Zeitschrift für anorganische und allgemeine Chemie* **2014**, *640*, 2742–2746.

(143) Figlarz, M. In *Materials Science Forum*, Trans Tech Publ: 1994; Vol. 152, pp 55–68.

(144) Hayward, M., 2.15 - Soft Chemistry Synthesis of Oxides In *Comprehensive Inorganic Chemistry II (Second Edition)*, Reedijk, J., Poeppelmeier, K., Eds., Second Edition; Elsevier: Amsterdam, 2013, pp 417–453.

(145) Okamoto, H. Supplemental Literature Review of Binary Phase Diagrams: Ag-Ni, Ag-Zr, Au-Bi, B-Ni, Co-Sb, Cu-Mn, Cu-Si, Cu-Zn, Fe-Zr, Li-Sb, Mg-Pu, and Si-Zr. *Journal of Phase Equilibria and Diffusion* **2018**, *39*, 87–100.

(146) Tooth, B.; Brugger, J.; Ciobanu, C.; Liu, W. Modeling of Gold Scavenging by Bismuth Melts Coexisting with Hydrothermal Fluids. *Geology* **2008**, *36*, 815.

(147) Shipunov, G.; Piening, B. R.; Wuttke, C.; Romanova, T. A.; Sadakov, A. V.; Sobolevskiy, O. A.; Guzovsky, E. Yu.; Usoltsev, A. S.; Pudalov, V. M.; Efremov, D. V.; Subakti, S.; Wolf, D.; Lubk, A.; Büchner, B.; Aswartham, S. Layered van Der Waals Topological Metals of $TaTMTe_4$ (TM = Ir, Rh, Ru) Family. *The Journal of Physical Chemistry Letters* **2021**, *12*, 6730–6735.

(148) Mar, A.; Ibers, J. A. Synthesis and Physical Properties of the New Layered Ternary Tellurides $MIrTe_4$ (M = Nb, Ta), and the Structure of NbIrTe4. *Journal of Solid State Chemistry* **1992**, *97*, 366–376.

(149) Sajadi, E.; Palomaki, T.; Fei, Z.; Zhao, W.; Bement, P.; Olsen, C.; Luescher, S.; Xu, X.; Folk, J. A.; Cobden, D. H. Gate-Induced Superconductivity in a Monolayer Topological Insulator. *Science* **2018**, *362*, 922–925.

(150) Koepernik, K.; Kasinathan, D.; Efremov, D. V.; Khim, S.; Borisenko, S.; Büchner, B.; van den Brink, J. $TaIrTe_4$: A Ternary Type-II Weyl Semimetal. *Physical Review B* **2016**, *93*, 201101.

(151) Khim, S.; Koepernik, K.; Efremov, D. V.; Klotz, J.; Förster, T.; Wosnitza, J.; Sturza, M. I.; Wurmehl, S.; Hess, C.; van den Brink, J.; Büchner, B. Magnetotransport and de Haas–van Alphen Measurements in the Type-II Weyl Semimetal $TaIrTe_4$. *Physical Review B* **2016**, *94*, 165145.

(152) Haubold, E. et al. Experimental Realization of Type-II Weyl State in Noncentrosymmetric $TaIrTe_4$. *Physical Review B* **2017**, *95*, 241108.

(153) Kumar, D.; Hsu, C.-H.; Sharma, R.; Chang, T.-R.; Yu, P.; Wang, J.; Eda, G.; Liang, G.; Yang, H. Room-Temperature Nonlinear Hall Effect and Wireless Radiofrequency Rectification in Weyl Semimetal $TaIrTe_4$. *Nature Nanotechnology* **2021**, *16*, 421–425.

(154) Guo, P.-J.; Lu, X.-Q.; Ji, W.; Liu, K.; Lu, Z.-Y. Quantum Spin Hall Effect in Monolayer and Bilayer $TaIrTe_4$. *Physical Review B* **2020**, *102*, 041109.

(155) Liu, J.; Wang, H.; Fang, C.; Fu, L.; Qian, X. Van Der Waals Stacking-Induced Topological Phase Transition in Layered Ternary Transition Metal Chalcogenides. *Nano Letters* **2017**, *17*, 467–475.

(156) Xing, Y.; Shao, Z.; Ge, J.; Luo, J.; Wang, J.; Zhu, Z.; Liu, J.; Wang, Y.; Zhao, Z.; Yan, J.; Mandrus, D.; Yan, B.; Liu, X.-J.; Pan, M.; Wang, J. Surface Superconductivity in the Type II Weyl Semimetal $TaIrTe_4$. *National Science Review* **2020**, *7*, 579–587.

(157) Schönemann, R.; Chiu, Y.-C.; Zheng, W.; Quito, V. L.; Sur, S.; McCandless, G. T.; Chan, J. Y.; Balicas, L. Bulk Fermi Surface of the Weyl Type-II Semimetallic Candidate $NbIrTe_4$. *Physical Review B* **2019**, *99*, 195128.

(158) Zhou, W.; Li, B.; Xu, C. Q.; Delft, M. R. van; Chen, Y. G.; Fan, X. C.; Qian, B.; Hussey, N. E.; Xu, X. Nonsaturating Magnetoresistance and Nontrivial Band Topology of Type-II Weyl Semimetal $NbIrTe_4$. *Advanced Electronic Materials* **2019**, *5*, 1900250.

(159) Appendix 7: Crystal Structure Data In *Crystallography and Crystal Defects*; John Wiley & Sons, Ltd: 2012, pp 491–498.

(160) Saeed, Y.; Singh, N.; Schwingenschlögl, U. Colossal Thermoelectric Power Factor in $K_{7/8}RhO_2$. *Advanced Functional Materials* **2012**, *22*, 2792–2796.

(161) Yao, S. H.; Zhang, B. B.; Zhou, J.; Chen, Y. B.; Zhang, S. T.; Gu, Z. B.; Dong, S. T.; Chen, Y. F. Structure and Physical Properties of $K_{0.63}RhO_2$ Single Crystals. *AIP Advances* **2012**, *2*, 042140.

(162) Shibasaki, S.; Nakano, T.; Terasaki, I.; Yubuta, K.; Kajitani, T. Transport Properties of the Layered Rh Oxide $K_{0.49}RhO_2$. *Journal of Physics: Condensed Matter* **2010**, *22*, 115603.

(163) Mendiboure, A.; Eickenbusch, H.; Schöllhorn, R.; Rao, G. V. S. Layered Alkali Rhodium Oxides A_xRhO_2: Topotactic Solvation, Exchange, and Redox Reactions. *Journal of Solid State Chemistry* **1987**, *71*, 19–28.

(164) Yubuta, K.; Shibasaki, S.; Terasaki, I.; Kajitani, T. High-Resolution Electron Microscopy for Incommensurate Structure of K_xRhO_2 Crystal. *Philosophical Magazine* **2009**, *89*, 2813–2822.

(165) Changdar, S.; Shipunov, G.; Joseph, N. B.; Plumb, N. C.; Shi, M.; Büchner, B.; Narayan, A.; Aswartham, S.; Thirupathaiah, S. Anomalous Band Renormalization Due to a High-Energy Kink in K 0.65 RhO 2 with Colossal Thermoelectric Power Factor. *Physical Review Materials* **2021**, *5*, 055402.

Appendix A

Results of Scanning Electron Microscopy

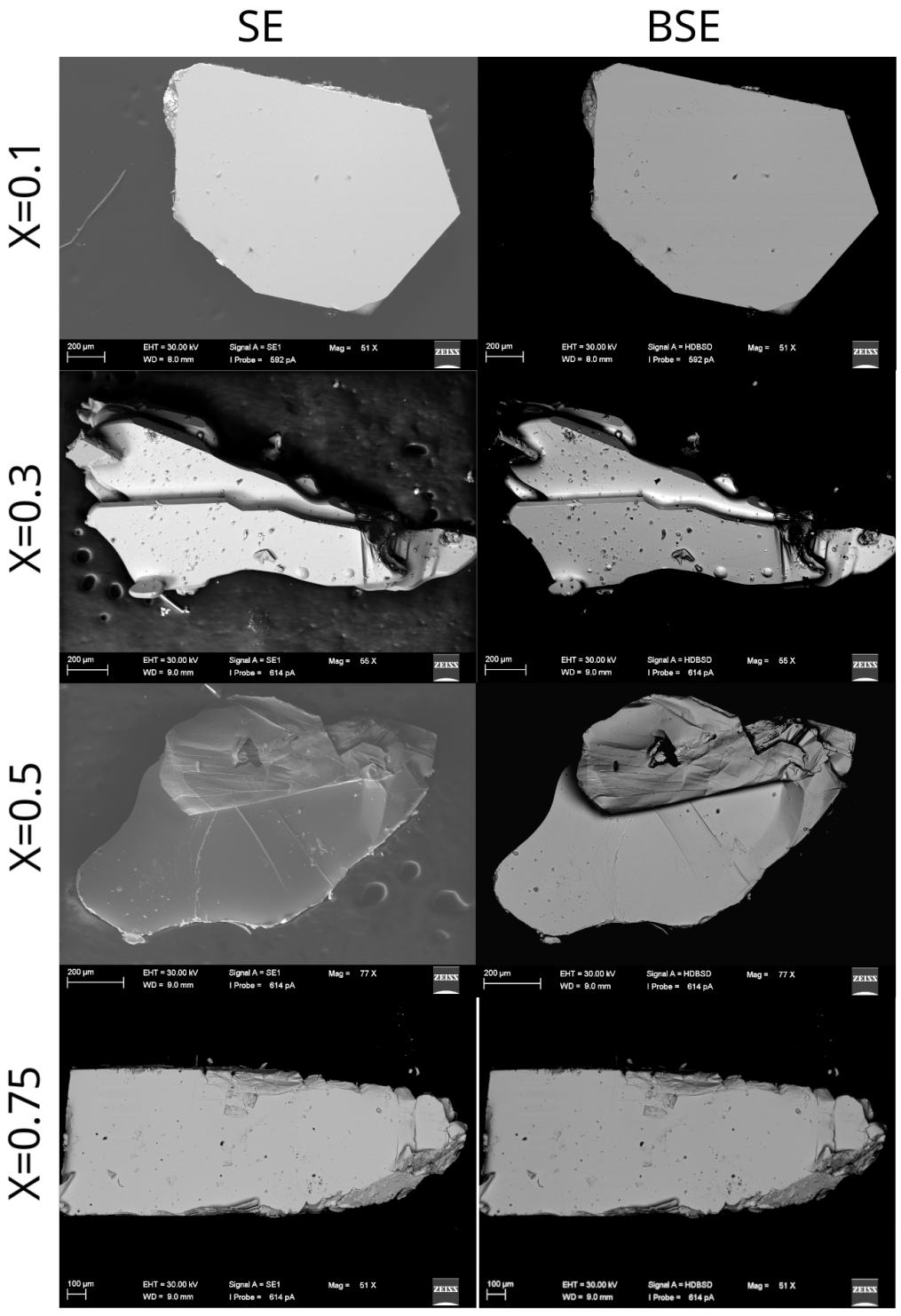

Figure A.1: Overview of SE and BSE SEM images for obtained $Pt_{1-x}Rh_xBi_2$ crystals.

Table A.1: Overview of $Pt_{1-x}Ni_xBi_2$ EDX results

Crystal	Ni	Pt	Bi
		mol%	
	Nominal $x = 0.1$		
A	1.67	31.6	66.73
A	22.39	6.82	70.8
A	21.16	6.62	72.22
B	2.85	31.96	65.19
B	3.39	30.23	66.39
B	4.55	31.97	63.48
B	3.73	31.91	64.36
B	5.31	32.16	62.53
B	6.5	31.91	61.59
C	5.62	31.5	62.89
C	5.5	31.49	63.01
C	6.27	30.16	63.57
C	5.39	31.27	63.33
	Nominal $x = 0.3$		
A	10.23	18.92	73.17
A	10.2	19.11	72.96
A	10.41	19.12	72.66
A	10.31	18.94	73.2
A	10.23	18.9	73.04
B	10.23	18.85	72.8
B	10.26	18.86	72.76
B	10.23	18.99	73.01
B	10.24	18.83	73.09
B	10.24	18.83	73
C	5.25	19.26	76.91
C	6.59	7.66	87.43
C	6.29	15.81	78.69
C	6.27	15.17	77.64
C	10.04	25.82	59.25
C	11.24	21.72	64.14
D	10.6	19.37	73.82
D	10.64	19.43	73.96
D	10.73	19.7	74.91

Crystal	Ni	Pt	Bi
		mol%	
	Nominal $x = 0.3$		
E	10.68	19.4	74.3
E	10.66	19.45	74.06
E	10.69	24.78	60.49
E	10.39	24.17	62.12
E	10.37	24.76	60.92
E	9.54	22.13	66.29
E	10.61	25.33	59.8
	Nominal $x = 0.5$		
A	1.43	29.74	71.07
A	1.45	29.49	71.33
A	1.38	28.9	69.5
A	1.39	28.47	68.42
A	1.32	28.09	67.22
B	1.24	28.02	65.93
B	1.25	27.79	65.38
B	1.42	31.92	66.66
B	1.23	27.57	65.73
B	1.23	27.28	64.87
C	1.02	25.72	61.61
C	0.99	25.49	61
C	0.98	25.52	60.96
C	1.03	25.5	61.13
C	1.09	25.21	61.34
D	0.74	1.09	97.35
D	0.82	1.54	97.78
D	1.43	27.45	66.34
D	1.49	27.64	66.12
D	1.46	27.36	65.32
D	1.32	27.69	69

Appendix B

Results of X-Ray Diffraction Studies

Table B.1: $Pt_{1-x}Rh_xBi_2$ structural parameters and residual factors of Rietveld analysis

Parameter	Composition, $Pt_{1-x}Rh_xBi_2$, x		
	0	0	0.03
Wavelength (Å)	1.78996	1.78996	1.78996
2θ range (°)	10–111.955	10–111.955	10–111.995
Step Size (°)	0.015	0.015	0.015
Temperature (K)	293	293	293
Space Group	$P\bar{3}$ (№147)	$P31m$ (№157)	$P31m$ (№157)
a (Å)	6.57651(4)	6.57703(2)	6.57696(2)
c (Å)	6.14724(8)	6.14795(4)	6.14796(4)
$U_{isotropic}$:			
U_{Pt1}	-0.0144(11)	0.0066(5)	0.0077(5)
U_{Pt2}	0.117(2)	n/a	n/a
U_{Bi1}	0.0799(8)	0.0159(9)	0.0164(9)
U_{Bi2}	n/a	0.0053(5)	0.0087(5)
U_{Bi3}	n/a	0.0157(4)	0.0142(5)
R	0.1569(all)	0.0273(prof)	0.0226
wR	0.1972(all)	0.0481(prof)	0.0324
Goodness-of-Fit	3.78 1.88	1.92	

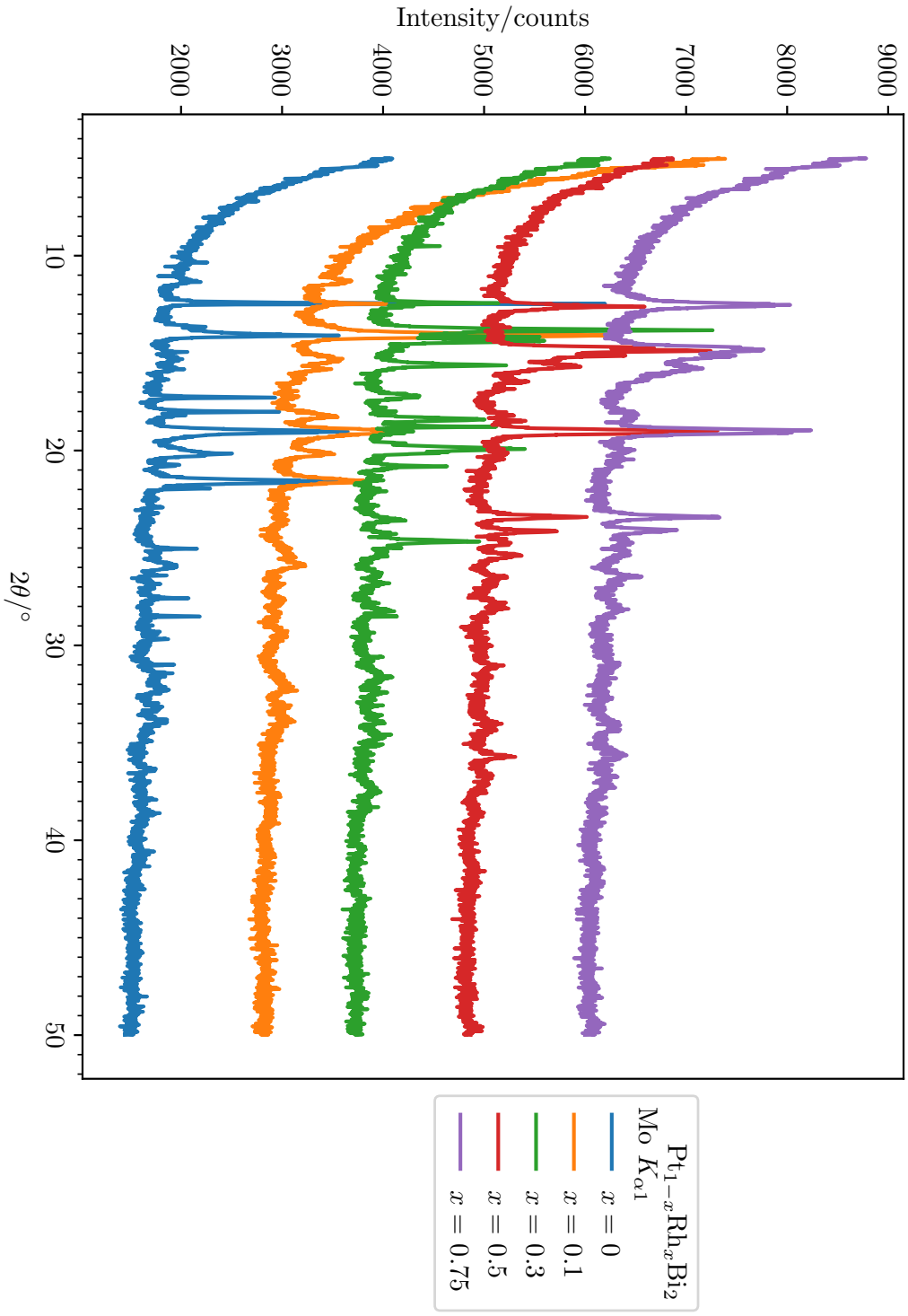

Figure B.1: Powder diffraction patterns of $Pt_{1-x}Rh_xBi_2$ samples. Every next curve is offset by 1000 counts along ordinate axis.

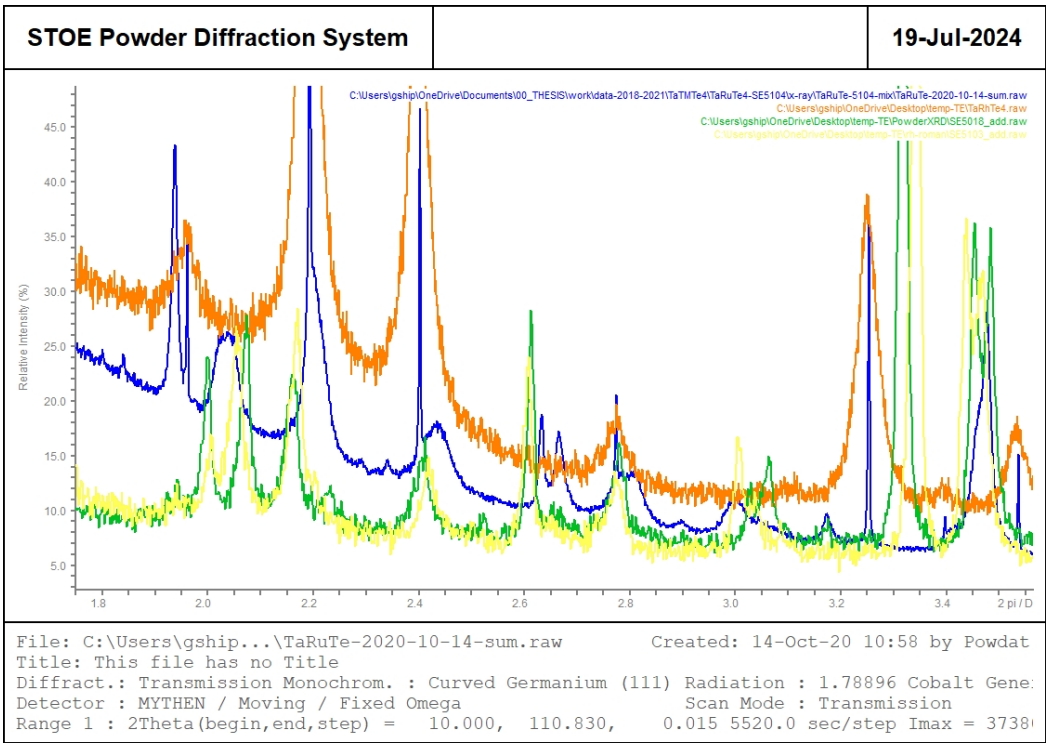

Figure B.2: Examples of $TaTMTe_4$ powder diffraction profiles

Table B.2: Refined atomic coordinates for $Pt_{1-x}Rh_xBi_2$

Sample	Atom	site	x	y	z
$PtBi_2$	Pt (Pt1)	3*c*	0.2587(2)	0	-0.0044(3)
	Bi (Bi1)	1*a*	0	0	-0.3437(4)
	Bi (Bi2)	2*b*	2/3	1/3	-0.2247(3)
	Bi (Bi3)	3*c*	0.6090(2)	0	0.2844(3)
$Pt_{0.97}Rh_{0.03}Bi_2$	Pt/Rh (Pt1)	3*c*	0.2617(2)	0	0.3578(6)
	Bi (Bi1)	1*a*	0	0	0.0139(6)
	Bi (Bi2)	2*b*	2/3	1/3	0.1413(6)
	Bi (Bi3)	3*c*	0.6093(2)	0	0.6345(5)

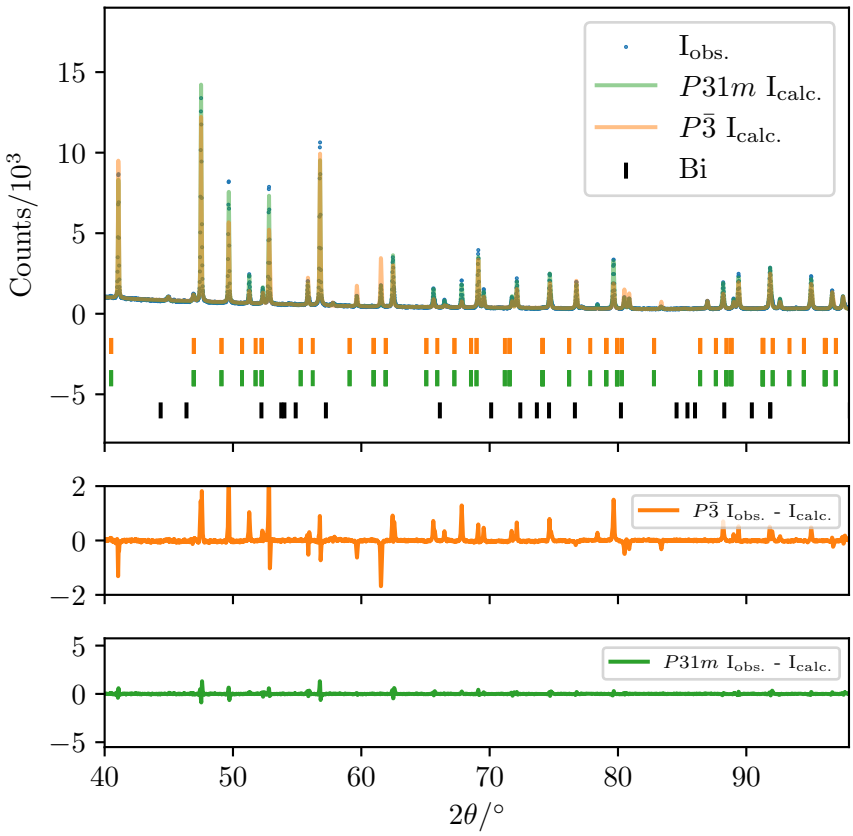

Figure B.3: Zoom-in of the Fig. 4.6

Table B.3: $TaTMTe_4$: Structural parameters and residual factors of Rietveld analysis

Parameter	$TaRhTe_4$	$TaIrTe_4$
Wavelength (Å)	0.70926	0.70926
2θ range (°)	5–50	5–50
Step Size (°)	0.01	0.01
Temperature (K)	293	293
Space Group	$Pmn2_1$ (№31)	$Pmn2_1$ (№31)
a (Å)	3.7576(1)	3.7850(1)
b (Å)	12.5476(4)	12.4444(4)
c (Å)	13.166(3)	13.193(3)
Rp	8.24	6.64
Rwp	10.5	8.48
χ^2	1.33	1.30

Table B.4: Refined atomic coordinates for $TaRhTe_4$

Atom (label)	site	x	y	z
Ta (Ta1)	2a	0.00000	0.05580	-0.19200
Ta (Ta2)	2a	0.00000	0.26530	0.29100
Rh (Rh1)	2a	0.00000	0.52760	-0.19800
Rh (Rh2)	2a	0.00000	0.75430	0.33100
Te (Te1)	2a	0.00000	0.05945	0.19049
Te (Te2)	2a	0.00000	0.19454	0.62601
Te (Te3)	2a	0.00000	0.34483	-0.09190
Te (Te4)	2a	0.00000	0.40783	0.44478
Te (Te5)	2a	0.00000	0.57274	0.19981
Te (Te6)	2a	0.00000	0.67725	0.65759
Te (Te7)	2a	0.00000	0.85038	-0.07740
Te (Te8)	2a	0.00000	0.90438	0.46746

Table B.5: Refined atomic coordinates for $TaIrTe_4$

Atom (label)	site	x	y	z
Ta (Ta1)	2a	0.00000	0.05500	-0.20000
Ta (Ta2)	2a	0.00000	0.26790	0.20000
Ir (Ir1)	2a	0.00000	0.53240	-0.20000
Ir (Ir2)	2a	0.00000	0.75420	0.30000
Te (Te1)	2a	0.00000	0.05920	0.10000
Te (Te2)	2a	0.00000	0.19500	0.60000
Te (Te3)	2a	0.00000	0.34410	-0.10000
Te (Te4)	2a	0.00000	0.40740	0.40000
Te (Te5)	2a	0.00000	0.57320	0.20000
Te (Te6)	2a	0.00000	0.67670	0.60000
Te (Te7)	2a	0.00000	0.85090	-0.10000
Te (Te8)	2a	0.00000	0.90430	0.40000

All Publications Involving the Author

(1) Changdar, S.; Shipunov, G.; Joseph, N. B.; Plumb, N. C.; Shi, M.; Büchner, B.; Narayan, A.; Aswartham, S.; Thirupathaiah, S. Anomalous band renormalization due to a high-energy kink in $K_{0.65}RhO_2$ with colossal thermoelectric power factor. *Physical Review Materials* **2021**, *5*, 055402.

(2) Changdar, S.; Aswartham, S.; Bose, A.; Kushnirenko, Y.; Shipunov, G.; Plumb, N.; Shi, M.; Narayan, A.; Büchner, B.; Thirupathaiah, S. Electronic structure studies of FeSi: A chiral topological system. *Physical Review B* **2020**, *101*, 235105.

(3) Thirupathaiah, S.; Morozov, I.; Kushnirenko, Y.; Fedorov, A.; Haubold, E.; Kim, T.; Shipunov, G.; Maksutova, A.; Kataeva, O.; Aswartham, S., et al. Spectroscopic evidence of topological phase transition in the three-dimensional Dirac semimetal $Cd_3(As_{1-x}P_x)_2$. *Physical Review B* **2018**, *98*, 085145.

(4) Shipunov, G.; Kovalchuk, I.; Piening, B.; Labracherie, V.; Veyrat, A.; Wolf, D.; Lubk, A.; Subakti, S.; Giraud, R.; Dufouleur, J., et al. Polymorphic $PtBi_2$: Growth, structure, and superconducting properties. *Physical Review Materials* **2020**, *4*, 124202.

(5) Sykora, S.; Schoop, J.; Graf, L.; Shipunov, G.; Morozov, I. V.; Aswartham, S.; Büchner, B.; Hess, C.; Giraud, R.; Dufouleur, J. Disorder-induced coupling of Weyl nodes in WTe_2. *Physical Review Research* **2020**, *2*, 033041.

(6) Veyrat, A.; Labracherie, V.; Bashlakov, D. L.; Caglieris, F.; Facio, J. I.; Shipunov, G.; Charvin, T.; Acharya, R.; Naidyuk, Y.; Giraud, R., et al. Berezinskii–Kosterlitz–Thouless transition in the type-I Weyl semimetal $PtBi_2$. *Nano Letters* **2023**, *23*, 1229–1235.

(7) Naidyuk, Y. G.; Bashlakov, D. L.; Kvitnitskaya, O. E.; Piening, B. R.; Shipunov, G.; Efremov, D. V.; Aswartham, S.; Büchner, B. Switchable domains in point contacts based on transition metal tellurides. *Physical Review Materials* **2021**, *5*, 084004.

(8) Naidyuk, Y. G.; Bashlakov, D.; Kvitnitskaya, O.; Aswartham, S.; Morozov, I.; Chernyavskii, I.; Shipunov, G.; Fuchs, G.; Drechsler, S.; Hühne, R., et al. Yanson point-contact spectroscopy of Weyl semimetal WTe_2. *2D Materials* **2019**, *6*, 045012.

(9) Shipunov, G.; Piening, B.; Wuttke, C.; Romanova, T.; Sadakov, A.; Sobolevskiy, O.; Guzovsky, E. Y.; Usoltsev, A.; Pudalov, V.; Efremov, D., et al. Layered van der Waals topological metals of $TaTMTe_4$ (TM= Ir, Rh, Ru) family. *The Journal of Physical Chemistry Letters* **2021**, *12*, 6730–6735.

(10) Kar, I.; Dolui, K.; Harnagea, L.; Kushnirenko, Y.; Shipunov, G.; Plumb, N. C.; Shi, M.; Büchner, B.; Thirupathaiah, S. Experimental Evidence of a Stable 2*H* Phase on the Surface of Layered 1 T⊠-$TaTe_2$. *The Journal of Physical Chemistry C* **2021**, *125*, 1150–1156.

(11) Bashlakov, D.; Kvitnitskaya, O.; Shipunov, G.; Aswartham, S.; Feya, O.; Efremov, D.; Büchner, B.; Naidyuk, Y. G. Electron-phonon interaction and point contact enhanced superconductivity in trigonal $PtBi_2$. *Low Temperature Physics* **2022**, *48*, 747–754.

(12) Schimmel, S.; Fasano, Y.; Hoffmann, S.; Besproswanny, J.; Corredor Bohorquez, L. T.; Puig, J.; Elshalem, B.-C.; Kalisky, B.; Shipunov, G.; Baumann, D., et al. Surface superconductivity in the topological Weyl semimetal t-$PtBi_2$. *Nature Communications* **2024**, *15*, 9895.

(13) Kuibarov, A.; Suvorov, O.; Vocaturo, R.; Fedorov, A.; Lou, R.; Merkwitz, L.; Voroshnin, V.; Facio, J. I.; Koepernik, K.; Yaresko, A., et al. Evidence of superconducting Fermi arcs. *Nature* **2024**, *626*, 294–299.

(14) Bashlakov, D.; Kvitnitskaya, O.; Aswartham, S.; Shipunov, G.; Harnagea, L.; Efremov, D.; Büchner, B.; Naidyuk, Y. G. Electron-phonon interaction, magnetic phase transition, charge density waves, and resistive switching in VS_2 and VSe_2 revealed by Yanson point-contact spectroscopy. *Low Temperature Physics* **2024**, *50*, 676–682.

(15) Hoffmann, S.; Schimmel, S.; Vocaturo, R.; Puig, J.; Shipunov, G.; Janson, O.; Aswartham, S.; Baumann, D.; Büchner, B.; Brink, J. v. d., et al. Fermi arcs dominating the electronic surface properties of trigonal $PtBi_2$. *Advanced Physics Research* **2025**, *4*, 2400150.

(16) Büchner, B.; Naidyuk, Y. G.; Kvitnitskaya, O.; Bashlakov, D.; HARNAGEA, L.; Aswartham, S.; Shipunov, G.; Efremov, D. Electron-phonon interaction, magnetic phase transition, charge density waves, and resistive switching in VS_2 and VSe_2 revealed by Yanson point-contact spectroscopy. **2024**.

(17) Veyrat, A.; Koepernik, K.; Veyrat, L.; Shipunov, G.; Kovalchuk, I.; Aswartham, S.; Qu, J.; Kumar, A.; Ceccardi, M.; Caglieris, F., et al. Dissipationless transport signature of topological nodal lines. *Nature Communications* **2025**, *16*, 6711.

(18) Behnami, M.; Gillig, M.; Moghaddam, A.; Efremov, D.; Shipunov, G.; Piening, B.; Morozov, I.; Aswartham, S.; Dufouleur, J.; Ochkan, K., et al. Large Nernst effect in Te-based van der Waals materials. *Physical Review Research* **2025**, *7*, 023009.

(19) Majchrzak, P.; Sanders, C.; Zhang, Y.; Kuibarov, A.; Suvorov, O.; Springate, E.; Kovalchuk, I.; Aswartham, S.; Shipunov, G.; Büchner, B., et al. Machine-learning approach to understanding ultrafast carrier dynamics in the three-dimensional Brillouin zone of $PtBi_2$. *Physical Review Research* **2025**, *7*, 013025.

(20) Caglieris, F.; Ceccardi, M.; Efremov, D.; Shipunov, G.; Kovalchuk, I.; Aswartham, S.; Veyrat, A.; Dufouleur, J.; Marré, D.; Büchner, B., et al. Fermi surface evolution in Weyl semimetal t-$PtBi_2$ probed by transverse transport properties. *Physical Review Materials* **2025**, *9*, 084202.

(21) Behnami, M.; Efremov, D.; Aswartham, S.; Shipunov, G.; Piening, B.; Blum, C.; Kocsis, V.; Dufouleur, J.; Pallecchi, I.; Putti, M., et al. Signature of chiral anomaly in the Weyl semimetal $TaRhTe_4$. *Physical Review B* **2025**, *112*, 045101.

(22) Kvitnitskaya, O.; Harnagea, L.; Shipunov, G.; Aswartham, S.; Kovalchuk, I.; Fisun, V.; Efremov, D.; Büchner, B.; Naidyuk, Y. G. Point-contact enhanced superconductivity in trigonal PtBi2: quest for the origin of "high-Tc". *Superconductor Science and Technology* **2025**.

(23) Changdar, S.; Suvorov, O.; Kuibarov, A.; Thirupathaiah, S.; Shipunov, G.; Aswartham, S.; Wurmehl, S.; Kovalchuk, I.; Koepernik, K.; Timm, C., et al. Topological nodal i-wave superconductivity in $PtBi_2$. *Nature* **2025**, *647*, 613–618.

Summary

Novel quantum materials demonstrate an array of peculiar electronic properties, which excite theoretical and experimental physicists alike, and spark interest of engineers regarding possible applications for low-power, high efficiency computation devices. But before physicists can lay their hands on single crystals, or CIF file describing the structure of thereof those materials are synthesized and studied by chemists and crystallographers, who quite often sit at a different department. When a person downloads a CIF file, or sees final result of composition assesment of the material at hand it is easy to assume for them that the model they are looking at is true without any caveats. Anyone who did any kind of research will assure you that it is way more complicated then that.

To start, one needs to understand how to make a material with targeted properties, and assess the reliability of compositional and structural analysis. That's why chemists keep chanting something along the line of "composition–structure–properties". When a physicist comes to a chemist asking, for example, to "just move the Fermi level by 10 meV"*, one cannot do that by moving said level with a fine tweezer. To modify that *property*, one need to accordingly change the *structure*, atomic and/or electronic. If we talking about bulk crystals, the fine tweezer method is, once again, determined to fail. So the knobs we have during the synthesis are composition and synthetic conditions, which, in turn, have an effect on the electronic and crystal structure, which finally manifests in a desired (or undesired) property. This relationship is illustrated on many published examples in Chapter 1.

Also, pretty much everyone in the field seems to be after "high quality single crystals". In published literature this "high quality" is usually a placeholder for large size, absence of internal stress, low mosaicity, low defect concentration, high compositional uniformity, etc. This qualities are controlled by synthetic approach. Knowing how the crystal was grown can tell one what to expect in the result. Another point, even While countless textbooks are written on both the problem of solid state material synthesis and solid state material characterization, Chapters 2 and 3 try to give a taste of modern characterization methods and synthetic approaches as applied to layered quantum materials.

To interpret results of physical property measurements theoretical assesment of electronic structure must be performed. For this, theory colleagues need a reliable description of crystal structure. Methods in the field of crystallography evolve, and as a result the standards of "proven beyond resonable doubt" rise both on side of physicists and chemists. Weissenberg camera and a room full of computers† behind electromechanical calculators was considered state of the art in the structure determination not so long ago. Nowadays the same results are acquired on a modern diffractometer, in a matter of minutes, and with computers out of silicon. And these results are considered "preliminary screening". This text tries to expose the complexity of the structure determination, provides a small taste of structural methods employed in a field of solid state in Chapter 3 and applies the whole composition, structure, property chain to several families of quantum materials in later chapters.

Chapter 4 introduces TSM and superconductor $PtBi_2$, and navigates through its rich polymoprphism. The goal is to optimize the synthesis of the trigonal γ-$PtBi_2$ polymorph that is the most interesting topological phase. Following the crystal growth of the target polymorph, its crystal structure is re-investigated, solving the long-standing controversy about its lattice symmetry. Consequently, this result clarifies which band structure model and topological electronic states are inherent to γ-$PtBi_2$. Moreover, several possible substitutional series are investigated and the effects of the substitution on structure and properties are preliminary assessed.

*A real question author was asked

†That's a job, not a device

Chapter 5 deals with a family of candidate type-II Weyl semimetals, ternary $TaTMTe_4$ (TM = Ir, Rh, Ru) compounds. Several members were published long ago, but no single crystals were available. Unlike for $PtBi_2$, there are no ternary phase diagrams, which complicates synthesis optimization. Crystal growth of $TaIrTe_4$, $TaRhTe_4$ and $Ta_{1.25}Ru_{0.75}Te_4$ has been successfully performed, and some transition-metal substitutions have been attempted. This chapter also revisits crystal structures of the family members, and finds out non-stoichiometry, atomic disorder and lattice changes in the $Ta_{1.25}Ru_{0.75}Te_4$ compound*. These findings categorize $TaRuTe_4$ as an isostructural and, likely, isovalent analogue of the type-II Weyl TSM WTe_2, which makes the former attractive for future in-depth studies.

Chapter 6 addresses K_xRhO_2, a compositionally versatile material with a rich phase diagram of physical properties as a function of x. We present a new synthetic approach to this material, which may potentially give access to new compositions and properties. We show the preliminary results of how the synthetic route impacts magnetic properties.

*This was previously reported as the stoichiometric, isostructural $TaRuTe_4$ compound[19]

Samenvatting

Nieuwe kwantummaterialen vertonen een hele reeks eigenaardige elektronische eigenschappen, die zowel theoretische als experimentele fysici enthousiast maken, en die bij ingenieurs interesse wekken vanwege mogelijke toepassingen in rekenapparaten met laag vermogen en hoge efficiëntie. Maar voordat fysici hun handen kunnen leggen op eenkristallen, of op een CIF-bestand dat de structuur van zulke materialen beschrijft, worden deze materialen gesynthetiseerd en bestudeerd door chemici en kristallografen, die vaak op een andere afdeling zitten. Wanneer iemand een CIF-bestand downloadt, of het eindresultaat ziet van de compositieanalyse van het materiaal in kwestie, is het makkelijk om aan te nemen dat het model waarnaar men kijkt zonder voorbehoud waar is. Iedereen die ook maar enig onderzoek heeft gedaan, zal je verzekeren dat het veel ingewikkelder ligt dan dat.

Om te beginnen moet men begrijpen hoe een materiaal met gerichte eigenschappen gemaakt kan worden, en hoe de betrouwbaarheid van compositionele en structurele analyse beoordeeld kan worden. Daarom blijven chemici iets in de trant van "samenstelling–structuur–eigenschappen" scanderen. Wanneer een fysicus naar een chemicus komt met de vraag om bijvoorbeeld 'even het Fermi-niveau met 10 meV te verschuiven [*], kan men dat niveau niet simpelweg met een fijn pincetje verplaatsen. Om die *eigenschap* te veranderen, moet men de *structuur* overeenkomstig aanpassen, atomair en/of elektronisch. Als we het over bulkkristallen hebben, is de methode met het fijne pincet wederom gedoemd te mislukken. De knoppen waaraan we tijdens de synthese kunnen draaien zijn dus samenstelling en syntheseomstandigheden; die beïnvloeden op hun beurt de elektronische en kristalstructuur, wat zich uiteindelijk uit in een gewenste, of ongewenste, eigenschap. Deze relatie wordt aan de hand van veel gepubliceerde voorbeelden geïllustreerd in Chapter 1.

Daarnaast lijkt vrijwel iedereen in het veld op zoek te zijn naar "high quality single crystals". In de gepubliceerde literatuur is die "high quality" meestal een verzamelterm voor grote afmetingen, afwezigheid van interne spanning, lage mozaïciteit, lage defectconcentratie, hoge compositionele uniformiteit, enzovoort. Deze eigenschappen worden bepaald door de syntheseaanpak. Weten hoe het kristal gegroeid is, vertelt vaak al wat men in het resultaat kan verwachten. Hoewel er talloze leerboeken zijn geschreven over zowel de synthese van vaste-stofmaterialen als de karakterisering ervan, proberen Chapters 2 and 3 een indruk te geven van moderne karakteriseringsmethoden en syntheseaanpakken zoals toegepast op gelaagde kwantummaterialen.

Om de resultaten van metingen aan fysische eigenschappen te interpreteren, moet een theoretische beoordeling van de elektronische structuur worden uitgevoerd. Daarvoor hebben theoriekollega's een betrouwbare beschrijving van de kristalstructuur nodig. Methoden binnen de kristallografie ontwikkelen zich voortdurend, en als gevolg daarvan stijgen de standaarden voor wat 'buiten redelijke twijfel bewezen" is, zowel aan de kant van fysici als aan die van chemici. Een Weissenberg-camera en een zaal vol computers[†] achter elektromechanische rekenmachines golden nog niet zo lang geleden als de stand van de techniek in structuurbepaling. Tegenwoordig worden dezelfde resultaten verkregen op een moderne diffractometer, in een kwestie van minuten, en met computers van silicium. En die resultaten worden beschouwd als 'preliminary screening". Deze tekst probeert de complexiteit van structuurbepaling zichtbaar te maken, geeft in Chapter 3 een kleine indruk van structurele methoden die in het veld van de vaste-stofchemie worden gebruikt, en past in de latere hoofdstukken de volledige keten samenstelling, structuur en eigenschap toe op verschillende families van kwantummaterialen.

[*] Een echte vraag die aan de auteur werd gesteld

[†] Dat is een baan, geen apparaat

Chapter 4 introduceert de TSM en supergeleider $PtBi_2$, en navigeert door het rijke polymorfisme ervan. Het doel is om de synthese te optimaliseren van de trigonale γ-$PtBi_2$-polymorf, de topologische fase die het meest interessant is. Na de kristalgroei van de doelpolymorf wordt de kristalstructuur opnieuw onderzocht, waarmee een langlopende controverse over de roostersymmetrie wordt opgelost. Daarmee verduidelijkt dit resultaat welk bandstructuurmodel en welke topologische elektronische toestanden inherent zijn aan γ-$PtBi_2$. Bovendien worden verschillende mogelijke substitutionele reeksen onderzocht en worden de effecten van substitutie op structuur en eigenschappen voorlopig beoordeeld.

Chapter 5 behandelt een familie van kandidaat type-II Weyl-halfmetalen, de ternaire $TaTMTe_4$-verbindingen (TM = Ir, Rh, Ru). Verschillende leden van deze familie zijn lang geleden gepubliceerd, maar er waren geen eenkristallen beschikbaar. Anders dan voor $PtBi_2$ bestaan er geen ternaire fasediagrammen, wat de optimalisatie van de synthese bemoeilijkt. De kristalgroei van $TaIrTe_4$, $TaRhTe_4$ en $Ta_{1.25}Ru_{0.75}Te_4$ is succesvol uitgevoerd, en enkele substituties op de overgangsmetaalpositie zijn geprobeerd. Dit hoofdstuk bekijkt ook de kristalstructuren van de familieleden opnieuw, en toont niet-stoichiometrie, atomaire wanorde en roosterveranderingen aan in de $Ta_{1.25}Ru_{0.75}Te_4$-verbinding*. Deze bevindingen categoriseren $TaRuTe_4$ als een isostructureel en waarschijnlijk isovalent analoog van de type-II Weyl-TSM WTe_2, wat het eerstgenoemde materiaal aantrekkelijk maakt voor toekomstige diepgaande studies.

Chapter 6 richt zich op K_xRhO_2, een compositioneel veelzijdig materiaal met een rijk fasediagram van fysische eigenschappen als functie van x. We presenteren een nieuwe syntheseaanpak voor dit materiaal, die mogelijk toegang kan geven tot nieuwe samenstellingen en eigenschappen. We laten voorlopige resultaten zien van de invloed van de syntheseroute op de magnetische eigenschappen.

*Dit werd eerder gerapporteerd als de stoichiometrische, isostructurele $TaRuTe_4$-verbinding[19]

Acknowledgments

While this thesis has only one name on the cover, it wouldn't happen without external factors, human or otherwise. First of all, those who taught me, corrected me, argued with me, fed me, distracted me, encouraged me, kept me sane, and especially those who occasionally asked me whether I had simply considered just finishing it—thank you. You know who you are. I also want to express my gratitude to the mindless machines that worked, the mindless machines that eventually worked, an the mindless machines that at least taught me something.

Tja, léék me dus destijds wel slim.